AD_____

Award Number:
W81XWH-09-1-0060

TITLE:
Ultrasound-Based Guidance for Partial Breast Irradiation Therapy

PRINCIPAL INVESTIGATOR:
Hassan Rivaz, Ph.D.

CONTRACTING ORGANIZATION:

Johns Hopkins University
Baltimore, MD   21218

REPORT DATE:
January 2012

TYPE OF REPORT: Annual Summary

PREPARED FOR: U.S. Army Medical Research and Materiel Command
               Fort Detrick, Maryland 21702-5012

DISTRIBUTION STATEMENT:

     Approved for public release; distribution unlimited

REPORT DOCUMENTATION PAGE

Form Approved
OMB No. 0704-0188

1. REPORT DATE	2. REPORT TYPE	3. DATES COVERED
1 Jan 2012	Annual Summary	

4. TITLE AND SUBTITLE	5a. CONTRACT NUMBER
	1Jan 2009 - 31 Dec 2011
Ultrasound-Based Guidance for Partial Breast Irradiation Therapy	5b. GRANT NUMBER
	W81XWH-09-1-0060
	5c. PROGRAM ELEMENT NUMBER

6. AUTHOR(S)	5d. PROJECT NUMBER
Hassan Rivaz, Ph.D.	5e. TASK NUMBER
	5f. WORK UNIT NUMBER
E-Mail: rivaz@jhu.edu	

7. PERFORMING ORGANIZATION NAME(S) AND ADDRESS(ES)	8. PERFORMING ORGANIZATION REPORT NUMBER
Johns Hopkins University Baltimore, MD 21218	

9. SPONSORING / MONITORING AGENCY NAME(S) AND ADDRESS(ES)	10. SPONSOR/MONITOR'S ACRONYM(S)
U.S. Army Medical Research and Materiel Command Fort Detrick, Maryland 21702-5012	
	11. SPONSOR/MONITOR'S REPORT NUMBER(S)

12. DISTRIBUTION / AVAILABILITY STATEMENT
Approved for Public Release; Distribution Unlimited

13. SUPPLEMENTARY NOTES

14. ABSTRACT
Tracked ultrasound elastography can be used for guidance in partial breast radiotherapy by visualizing the hard scar tissue around the lumpectomy cavity. For clinical success, the elastography method needs to be robust to the sources of decorrelation between ultrasound images, specifically fluid motions inside the cavity, change of the appearance of speckles caused by compression or physiologic motions, and out-of-plane motion of the probe. In this report, we extend our previous work where we proposed 1D Analytic Minimization (1D AM) of a cost function to calculate robust elasticity images to 2D AM. We show that 2D AM is much faster than 1D AM, which is critically important in creating real-time elastography. In elasticity reconstruction using an inverse problem framework. We also propose a novel strain addition, 2D AM produces high quality strain images in 2D which can be used for calculation technique using Kalman filters, which generates smooth strain images without blurring the images and removing sharp boundaries. We show using simulation, phantom and clinical trials that the 2D AM generates high quality strain images in real-time. This work is in published in 2 IEEE TMI articles (23 pages total), and in 5 conference proceeding papers (each paper 8 to 9 pages, 42 pages total). The papers are well received, resulting in more than 55 citations to date according to Google Scholar.

15. SUBJECT TERMS
Partial Breast Radiation Therapy, Ultrasound Elastography, Regularization, Iterative Reweighted Least Squares, Tracked Ultrasound, Kalman filtering

16. SECURITY CLASSIFICATION OF:			17. LIMITATION OF ABSTRACT	18. NUMBER OF PAGES	19a. NAME OF RESPONSIBLE PERSON USAMRMC
a. REPORT	b. ABSTRACT	c. THIS PAGE			19b. TELEPHONE NUMBER *(include area code)*
U	U	U	UU		

Table of Contents

INTRODUCTION:

A tracked free-hand ultrasound system is ideal for guiding many radiotherapy procedures, as it can be performed in the treatment room. In partial breast irradiation, the lumpectomy cavity should be localized during the treatment course. While many structures in the breast look similar to the lumpectomy cavity in ultrasonography, the scar tissue around the cavity is hard and can be visualized by ultrasound elastography. To be clinically successful, the elastography method needs to be robust to the sources of decorrelation between ultrasound images, specifically fluid motions inside the cavity, change of the appearance of speckles caused by compression and physiologic motions, and out-of-plane motion of the probe. We presented a novel elastography technique that was based on Dynamic Programming (DP) and analytic minimization of a regularized cost function. The cost function incorporates similarity of RF data intensity and displacement continuity, making the method robust to decorrelation noise present throughout the image. We exploited techniques from robust statistics to make the method resistant to large decorrelations caused by sources such as fluid motion. The analytic displacement estimation worked in real-time. We further used the tracked data, used for targeting the irradiation, for discarding frames with excessive out-of-plane motion. In this method, we introduced an "optimal frame selection function" which selected the best frames –using the tracking data- to generate high quality elasticity images. In addition, we have extended the 1D method to 2D, meaning that we can calculate tissue displacements more completely. The 2D method follows the path of the 1D method in optimizing regularized cost functions and is also real-time. And finally, we have developed a 3D elasticity imaging technique based on DP and analytic minimization of a cost function for volumetric imaging of the elasticity.

We also introduced Kalman filtering for calculating strain images. The Kalman filter allows estimating low variance strain images, while it doesn't eliminate boundaries by over-smoothing the strain images. A major contribution has also been made in utilizing multiple ultrasound images to calculate the elasticity image. Displacement estimation is an essential step for ultrasound elastography and numerous techniques have been proposed to improve its quality using *two* frames of ultrasound RF data. We introduced a technique for calculating a displacement field from *three (or multiple)* frames of ultrasound RF data. To calculate a displacement field using three images, we first derive constraints on variations of the displacement field with time using mechanics of materials. These constraints are then used to generate a regularized cost function that incorporates amplitude similarity of three ultrasound images and displacement continuity. We optimize the cost function in an expectation maximization (EM) framework. Iteratively reweighted least squares (IRLS) is used to minimize the effect of outliers. We show that, compared to using two images, the new algorithm reduces the noise and eliminates ambiguities in displacement estimation. The displacement field is used to generate strain images for quasi-static elastography.

BODY:

We are very excited to report the novel achievements of this research effort. The detailed Statement of Work tasks and a description below each task is provided next. The SOW tasks are in blue. A description of the research effort follows each SOW item in **black**.

1.   **Obtain ultrasound (US), US elastography (USE) and CT scans before the start of the radiotherapy.**
a.   **Develop a tracked US system for data collection (month 1).** We will use Polaris optical tracker, already available in the ERC-CISST for tracking. Polaris markers will be attached to the US probe and the US probe will be calibrated with respect to the trackers.

Polaris optical tracker gives very accurate displacement measurements. However, they require line of sight (as they are optical) and also they take longer time to set up in a CT imaging room. Because of the time constraints (we had a short amount of time to set up the tracking device in the CT room before the patient shows up), we instead used magnetic trackers. Magnetic trackers are not as accurate as Polaris and suffer from distortion of magnetic field due to presence of metals. However, they do not require line of sight and also easier to set up and also are inexpensive. We started by using a Polaris camera to collect position data. However, setting up the camera was cumbersome and the limited time that we had in the CT room did not allow the required preparations. Therefore, we opted for a magnetic tracker and continued data collection using a magnetic tracker.

b.   **Collect US data from patient before the PBI treatment at the same time that CT is collected (months 2-14).**

We have collected data from 16 patients so far. All data was acquired in the CT room while the patient was lying down on the CT bed. The patient did not move after ultrasound data was acquired until her CT scan was finished. We have acquired both 3D ultrasound data (freehand data, no 3D probe is used) and palpation data (for elastography). More details of the system are in the attached paper (MICCAI conference, 34% acceptance rate, MedLine and ISI indexed and listed). I received travel award from MICCAI (only 7 students received this award) to present this work.

Our approach introduces minimal divergence from the original workflow of PBI treatment. We have an approved institutional review board (IRB) protocol to obtain B-mode and strain images from patients who undergo lumpectomy. We acquire the ultrasound data when the patients return for the CT scan four weeks after the surgery. The data includes tracked B-mode images scanned over the lumpectomy bed, tracked real-time strain images, and RF dara synchronized with the tracking

information for off-line processing. We have devised a data collection system for this purpose shown in Figure 1.

Before acquiring the CT scan, four CT-compatible fiducials are placed around the scar of the surgery on patient's breast. These fiducials are additional to the ones that are commonly placed on patient's chest and the resting foam bed. The foam bed, shown in Figure 1 maintains the configuration of patient's body during the treatment. The extra fiducials are used to locally align the CT and ultrasound data, and the regular ones are used for targeting at the time of irradiation.
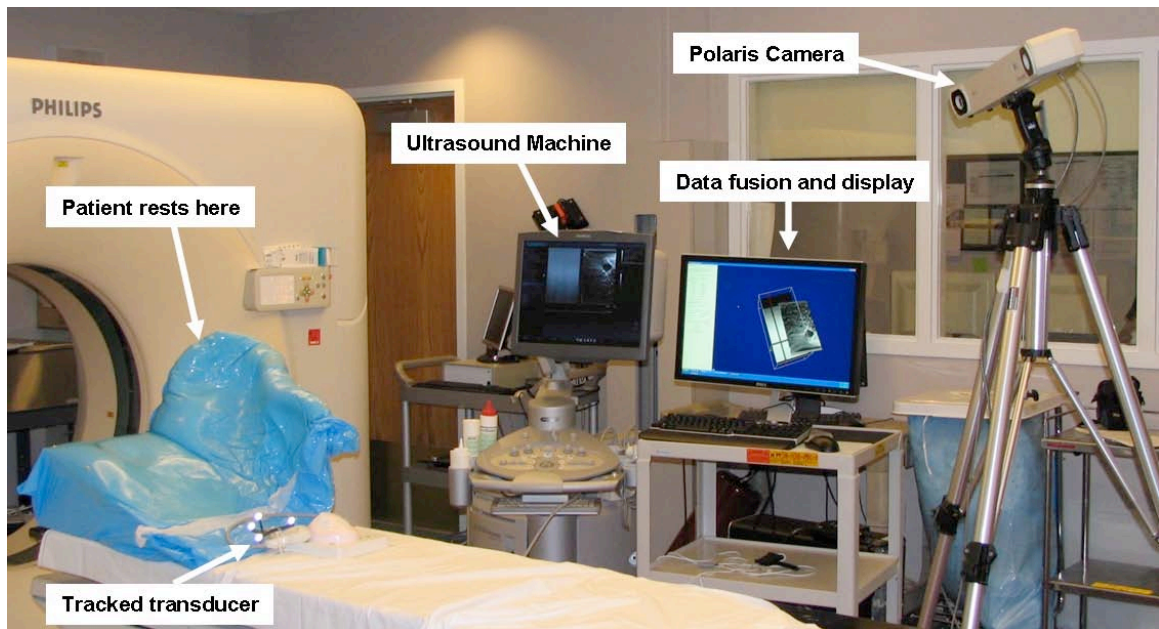

Figure 1. The Polaris camera (NDI, Waterloo, Canada) tracks the 3D orientation of the ultrasound probe by detecting the 4 bright spheres attached to the ultrasound transducer.

The patient remains in the same resting position after the CT scan. As the first step, the sonographer digitizes the location of the fiducials with a calibrated stylus by simply touching each of the four fiducials with the stylus in a certain order prescribed in our protocol. Afterwards, the sonographer sweeps the ultrasound transducer over the lumpectomy bed collecting at least 500 B-mode images. Then within a few seconds, the program constructs the ultrasound volume from the collected images. Next, the sonograhper obtains individual tracked strain images from the areas of interest by gently moving the ultrasound transducer up and down. The visualization program demonstrates the flying strain image over the ultrasound volume (Figure 2). Depending on each case, we acquire a minimum of 200 strain images. Lastly, we record sequences of RF signals as the sonographer compresses

and decompresses the tissue. The RF data synchronized with the tracking information facilitates more elaborate strain imaging techniques.
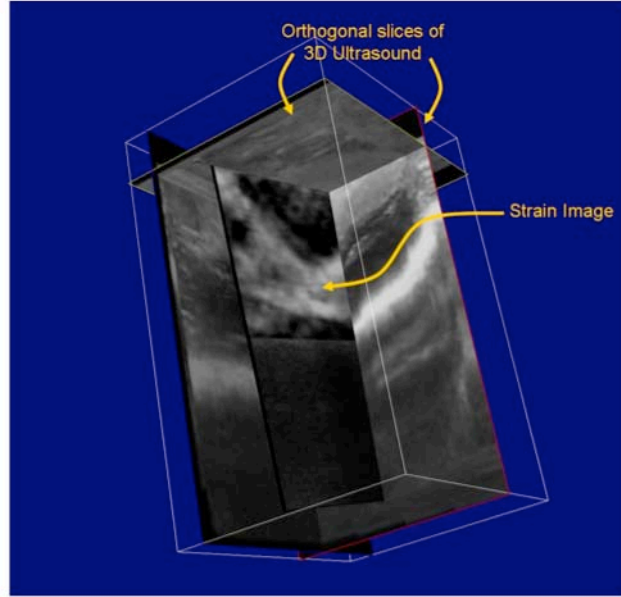

Figure 2. The visualization software shows 3D ultrasound and strain images.

To generate 3D ultrasound, we have developed a novel method that uses the ultrasound scatterers to create a high quality 3D volume. Out-of-plane motion in freehand 3D ultrasound can be estimated using the correlation of corresponding patches, leading to sensorless freehand 3D ultrasound systems. The correlation between two images is related to their distance by calibrating the ultrasound probe: the probe is moved with an accurate stage (or with a robot in this work) and images of a phantom are collected, such that the position of each image is known. Since parts of the calibration curve with higher derivative gives lower displacement estimation error, previous work limits displacement estimation to parts with maximum derivative. In this paper, we first propose a novel method for exploiting the entire calibration curve by using a maximum likelihood estimator (MLE). We then propose for the first time using constrains inside the image to enhance the accuracy of out-of-plane motion estimation. We specifically use continuity constraint of a needle to reduce the variance of the estimated out-of-plane motion. Simulation and real tissue experimental results are presented. The published paper attached at the end of the report titled "Novel Reconstruction and Feature Exploitation Techniques for Sensorless Freehand 3D Ultrasound" thoroughly explains this technique.

c.   Register US to the CT (months 2-14).

We advanced significantly and proposed exciting new avenues for further work in developing novel techniques for elastography, which is the major contribution of this research proposal. Therefore, we have not had enough time to focus on this task. However, we have performed registration of US and CT using the tracking information (obtained from the Polaris camera). The registration is included in the data acquisition software, which enabled fast and smooth data collection and visualization. The application interfaces with the ultrasound machine and the tracker (optical or magnetic), synchronizes, records, and visualizes the data. It is implemented in C++ with a multi-threaded scheme for better performance. We have also developed a simple and intuitive graphical user interface (GUI).

B-mode images and transducer locations are continuously stored in two circular buffers in separate threads with the highest rate possible. A time-stamp with microsecond accuracy is also recorded along with the captured data. A constant delay calculated off-line is applied to synchronize the stream of data. Acquisition of B-mode images is fast, and the region of interest can be scanned within a few seconds. The maximum rate of storing data is bounded with the minimum of frame rate of the B-mode images and the tracker. However, the user can set the rate of data storage to a lower rate through the GUI if needed. Due to the high data rate and large frame sizes captured per second (typically 10 to 30 frames per second), immediate saving to the hard drive may result in unexpected delays or loss of frames. Therefore, the data is first stored in the random access memory (RAM) of the computer and stored in hard disk only when the data collection is stopped.

Once the B-mode scan is acquired, the program constructs a 3D-US volume. The volume is presented as three orthogonal slices that can be freely translated and rotated in space as shown in Figure 2. VTK (Kiteware Inc.) is mainly used for the visualization and reslicing tasks (Figure 3). The real-time strain images are captured in the same manner except that the strain plane is overlaid on 3D-US. In addition, the program can sends commands to ultrasound machine for capturing sequences of RF data. When the ultrasound machine receives the command, captures and saves one sequence of RF frames, while our program records the tracking information.

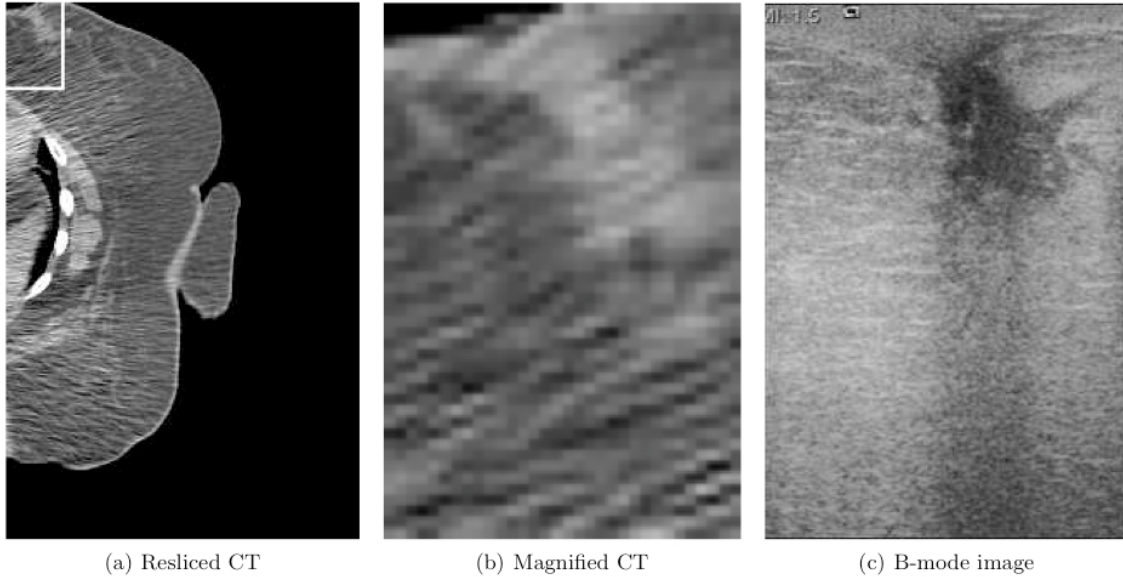(a) Resliced CT   (b) Magnified CT   (c) B-mode image

Figure 3. Registration of CT and ultrasound. (a) Shows a CT image, sliced in 3D (using interpolation) to match the ultrasound image, whose orientation is known from the tracking information. In (b), the square region of (a) is magnified. (c) shows the corresponding ultrasound image.

In addition, we performed some efforts to improve the tracking-based registration results of Figure 3 by generating a pseudo-ultrasound image from the CT volume and registering the CT and ultrasound through the pseudo-ultrasound, but the preliminary results were not satisfactory, and we decided to use the tracking-based registration results of Figure 3.

d.   **Compare different combination of US, USE and CT for delineation (months 3-18).**

We have done preliminary studies on comparing the performance of the operator with different imaging modalities. While it is intuitive that adding ultrasound and elastography enhance the delineation of the lumpectomy bed, we have not achieved a conclusive result yet.

e.   **Optimize USE code for using the human data (months 3-24).** I have developed a novel USE technology and software under a Breast Cancer Research Foundation research. The work thus far has been extremely promising: a manuscript has already been accepted for publication in the IEEE Trans. Med. Imag. I will be further improving my USE implementation to enhance visualization of the lumpectomy bed and ductal tissue.

Extremely promising results have been obtained in this area. We have developed new elastography techniques that generate superb images from the human data. In J1 (cited below and attached to the report), we introduced a 2D strain imaging technique based on minimizing a cost function using dynamic programming (DP). The cost function incorporates similarity of echo amplitudes and displacement continuity. Since tissue deformations are smooth, the incorporation of the smoothness into the cost function results in reduced decorrelation noise. As a result, the method generates high quality strain images of freehand palpation elastography with up to 10% compression, showing that the method is more robust to signal decorrelation (caused by scatterer motion in high axial compression and non-axial motions of the probe) in comparison to the standard correlation techniques. The method operates in less than 1 second and is thus also potentially suitable for real time elastography. In J2 (cited below and attached to the report), we further proposed an analytic minimization technique for strain estimation that generates smooth strain images from the DP USE images. In C1 (cited below and attached to the report), we proposed to exploit tracking information to select the best frames for USE, and showed that optimal frame selection enhances the USE quality. In C2 (cited below and attached to the report), we introduce a technique for calculating a displacement field from three frames of ultrasound RF data. To this end, we first introduced constraints on variations of the displacement field with time using mechanics of materials. These constraints are then used to generate a regularized cost function that incorporates amplitude similarity of three ultrasound images and displacement continuity. We optimize the cost function in an expectation maximization (EM) framework. Iteratively reweighted least squares (IRLS) is used to minimize the effect of outliers. We show that, compared to using two images, the new algorithm reduces the noise of the displacement estimation. The displacement field is used to generate strain images for quasi-static elastography.

C1. **Rivaz, H.**, Foroughi, P., Fleming, I., Zellars, R., Boctor, E., Hager, G., Tracked Regularized Ultrasound Elastography for Targeting Breast Radiotherapy, Medical Image Computing and Computer Assisted Intervention, MICCAI, London, UK, Sept. 2009, pp 507-515 [acceptance rate: 33%] Conference listed in PubMed and papers treated and cited similar to high-impact factor journal papers.

C2. **Rivaz, H.**, Boctor, E., Choti, M., Hager, G., "Ultrasound Elastography Using Multiple Images", IEEE Trans. Medical Imaging [acceptance rate: 30%]. Conference listed in PubMed and papers treated and cited similar to high-impact factor journal papers.

J1. **Rivaz, H.**, Boctor, E., Foroughi, P., Zellars, R., Fichtinger, G., Hager, G., Ultrasound Elastography: a Dynamic Programming Approach, IEEE Trans. Medical Imaging, Oct. 2008, vol. 27 pp 1373-1377

J2. **Rivaz, H.**, Boctor, E., Choti, M., Hager, G., Real-Time Regularized Ultrasound Elastography, IEEE Trans. Medical Imaging April 2011, vol. 30 pp 928-945.

**f.	Performance optimization and refinements of subsystems (months 18-36).**

The ultrasound elastography subsystem is almost finalized. We have made the code also available to the public[1], so that groups who work in different applications of ultrasound elastography can exploit our novel and high-quality elastography estimation technique. We could confidently say that the method can be implemented commercially with small modifications.

**2.	Obtain tracked US and USE scans of the patients weekly during the radiotherapy (months 2-14).** This data will be acquired from the same patients from whom US and USE data were acquired in step 1.b.

As mentioned in the 1b Section, elastography and ultrasound images are both acquired from patients.

**3.	Develop US to US registration (month 25-27).** This task is partly solved in task 1.c. (US to CT registration). As mentioned, US to US registration is one of the steps required in US to CT registration. I will optimize this step to work with breast images, as opposed to simulation images in task 1.c.

As mentioned before, registration of the pseudo-ultrasound to the ultrasound images are required to perform CT to ultrasound registration. Please refer to the task 1.c for more details.

KEY RESEARCH ACCOMPLISHMENTS:

•	Development of a novel, real-time, robust and high quality elastography techniques
•	Development of a tracked ultrasound system using magnetic trackers
•	Development of a technique for 3D volumetric ultrasound imaging using US image data
•	Study of ultrasound images of lumpectomy cavity
•	Study of elastography images of lumpectomy cavity
•	Data acquisition from more than 15 patients
•	Developed the 2D AM method which calculates high quality 2D strain images in real-time

---

[1] Available online at www.cs.jhu.edu/~rivaz/Ultrasound_Elastography

- Introduced ElastMI (Elastography using Multiple Images), a novel method which generates high quality strain images by utilizing multiple ultrasound images.

REPORTABLE OUTCOMES:

C1. **Rivaz, H.**, Foroughi, P., Fleming, I., Zellars, R., Boctor, E., Hager, G., Tracked Regularized Ultrasound Elastography for Targeting Breast Radiotherapy, Medical Image Computing and Computer Assisted Intervention, MICCAI, London, UK, Sept. 2009, pp 507-515 [acceptance rate: 33%] Conference listed in PubMed and papers treated and cited similar to high-impact factor journal papers.

C2. **Rivaz, H.**, Boctor, E., Choti, M., Hager, G., "Ultrasound Elastography Using Multiple Images", IEEE Trans. Medical Imaging [acceptance rate: 30%]. Conference listed in PubMed and papers treated and cited similar to high-impact factor journal papers.

C3. **Rivaz, H**., Fleming, I., Assumpcao, L., Fichtinger, G., Hamper, U., Choti, M., Hager, G., Boctor, E., Ablation Monitoring with Elastography: 2D In-vivo and 3D Ex-vivo Studies, Medical Image Computing and Computer Assisted Intervention, MICCAI, New York, NY, Sept. 2008, pp 458-466 [acceptance rate: 33%].

C4. Foroughi, P., **Rivaz, H.**, Fleming, I., Hager, G., Boctor, E. "Tracked Ultrasound Elastography (TrUE)", Medical Image Computing and Computer Assisted Intervention, MICCAI, Beijing, China, Sept. 2010, pp 9-16 [Acceptance rate: 32%]

C5. **Rivaz, H.**, Kang, H., Stolka, P., G. Hager, Boctor, E. "Novel reconstruction and feature exploitation techniques for sensorless freehand 3D ultrasound", SPIE Med. Imag., 2010, pp 76291D1-76291D9

J1. **Rivaz, H.**, Boctor, E., Foroughi, P., Zellars, R., Fichtinger, G., Hager, G., Ultrasound Elastography: a Dynamic Programming Approach, IEEE Trans. Medical Imaging, Oct. 2008, vol. 27 pp 1373-1377

J2. **Rivaz, H.**, Boctor, E., Choti, M., Hager, G., Real-Time Regularized Ultrasound Elastography, IEEE Trans. Medical Imaging April 2011, vol. 30 pp 928-945.

Training:

The training obtained during the year of 2010 was mainly in the following forms:
•	Reading papers related to partial breast radiation therapy techniques
•	Helping in preparation of Institutional Review Boards (IRB) for patient trials
•	Meetings with radiation oncologists on the problems of current breast radiotherapy workflow
•	Analyzing and enhancing the CT, ultrasound and strain images obtained from the lumpectomy
•	Setting up the image acquisition setup for imaging lumpectomy patients and helping in CT and ultrasound data collection.

CONCLUSION:

Data acquisition from lumpectomy patients went smoothly. We acquired the ultrasound data few minutes before the CT scan was acquired. This means that we did not alter the current medical work-flow. Ultrasound data acquisition took only few minutes, minimizing the cost and patient discomfort. Magnetic tracking provided ease of use and enough reliability for registration of ultrasound to CT images and for reconstructing 3D volumes from 2D data. The novel ultrasound elastography technique has many advantages compared to the previous methods. We chose the novel application of the lumpectomy cavity localization as the hard scar tissue around the lumpectomy is relatively thin and demands a high resolution elastography method. Also, incoherent fluid motions in the cavity causes large decorrelations, requiring a robust method. Due to the hard and noisy ultrasound images acquired from lumpectomy patients, we developed robust image analysis techniques, namely the Dynamic Programming (DP) elastography method as explained before, the Analytic Minimization (AM), Kalman filtering and Iteratively Reweighted Least Squares (IRLS) USE methods as explained before, the Elastography Using Multiple Images (ElastMI) framework for exploiting multiple images to enhance USE quality, and the Expectation Maximization (EM) method for 3D volumetric ultrasound generation using the ultrasound scatterer information. We also believe that USE is useful also for imaging breast tumors to reduce the number of biopsy referrals, as USE is an extremely more convenient and less expensive option.

References:

1. Rivaz, H., Boctor, E., Choti, M., Hager, G., "Ultrasound Elastography Using Multiple Images", IEEE Trans. Medical Imaging (submitted)

2. Rivaz, H., Boctor, E., Choti, M., Hager, G., "Real-Time Regularized Ultrasound Elastography", IEEE Trans. Medical Imaging (2011, in press)

3. Rivaz, H., Boctor, E., Hager, G., "2D Robust Motion Estimation" 9th Int. elastography Conf., Snowbird, UT, Oct 2010, p 129 (oral presentation)

4. Rivaz, H., Boctor, E., Foroughi, P., Zellars, R., Fichtinger, G., Hager, G., "Ultrasound Elastography: a Dynamic Programming Approach", IEEE Trans. Medical Imaging Oct. 2008, vol. 27 pp 1373-1377

5. Rivaz, H., Rohling, R., "An Active Dynamic vibration Absorber for a Hand-Held Vibro-Elastography Probe," ASME Trans. Vibration & Acoustics, Feb. 2007, vol. 129, pp 101-112 [Top 10 most downloaded articles from this journal in March 2008]

6. Rivaz, H., Kang, H., Stolka, P., Boctor, E. "Novel reconstruction and feature exploitation techniques for sensorless freehand 3D ultrasound", SPIE Med. Imag., 2010 (accepted)

7. Rivaz, H., van Vledder, M., Choti M., Hager, G., Boctor, E. "Liver ablation guidance: discriminating ablation tumor from the cancer tumor with ultrasound elastography", SPIE Med. Imag., 2010 (accepted)

8. Rivaz, H., Foroughi, P., Fleming, I., Zellars, R., Boctor, E., Hager, G., "Tracked Regularized Ultrasound Elastography for Targeting Breast Radiotherapy", Medical Image Computing and Computer Assisted Intervention, MICCAI, London, UK, Sept. 2009, pp 507-515. [Acceptance rate: 34%] [Awarded MICCAI Travel Grant]

9. Rivaz, H., Liang, J., Shinagawa Y., "Electronic Colon Cleansing of the Unprepared Colon", SPIE Med. Imag., Orlando, FL,2009, Vol. 726019, pp 1901-1912

10. Fleming, I., Rivaz, H., Hamper, U., Hager, G., Boctor, E., "Ultrasound elastography: Enabling technology for image guided laparoscopic prostatectomy", SPIE Medical Imaging, Orlando, FL, Feb. 2009, Vol. 72612I

11. Foroughi, P., Csoma, C., Rivaz, H., Fichtinger, G., Zellars, R., Hager, G., Boctor, E., "Multi-modality fusion of CT, 3D ultrasound, and tracked strain images for breast irradiation planning", SPIE Medical Imaging, Orlando, FL, Feb. 2009, Vol. 72651B [Best Poster Award, Second Best Paper Award]

12. Boctor, E., Matinfar, M., Ahmad, O, Rivaz, H., Choti, M. Taylor, R. "Elasticity-based three dimensional ultrasound real-time volume rendering", SPIE Medical Imaging, Orlando, FL, Feb. 2009, Vol. 72612V

13. Rivaz, H., Fleming, I., Matinfar, M., Khamene, A., Choti, M., Hager, G., Boctor, E., "Ablation Monitoring with a Regularized 3D Elastography Technique", IEEE Int. Ultrasonics Symposium, Beijing, China, Oct. 2008 pp 308 – 312

14. Rivaz, H., Fleming, I., Assumpcao, L., Fichtinger, G., Hamper, U., Choti, M., Hager, G., Boctor, E., "Ablation Monitoring with Elastography: 2D In-vivo and 3D Ex-vivo Studies", Medical Image Computing and Computer Assisted Intervention, MICCAI, New York, NY, Sept. 2008, pp 458-466 [Acceptance rate: 34%]

15. Rivaz, H., Zellars, R., Hager, G. Fichtinger, G., Boctor, E., "Beam Steering Approach to Speckle Characterization and Out-of-Plane Motion Estimation in Real Tissue", IEEE Int. Ultrasonics Symposium, New York, NY, Oct. 2007 pp 781-784

16. Rivaz, H., Boctor, E., Fichtinger, G., "A Robust Meshing and Calibration Approach for Sensorless Freehand 3D Ultrasound", SPIE Medical Imaging, San Diego, CA, Feb. 2007, Vol. 6513, pp 181-188

17. Rivaz, H., Boctor, E., Fichtinger, G., "Ultrasound Speckle Detection using Low Order Statistics," IEEE Int. Ultras. Symp., Vancouver, Canada,2006, pp 2092 – 2095

18. Rivaz, H., Rohling, R., "A Hand-Held Device for Vibro-Elastography," Medical Image Computing and Computer Assisted Intervention, MICCAI, Palm Springs, CA, Oct. 2005, pp 613-620 [Acceptance rate: 34%]

19. Deshmukh, N., Rivaz, H., Boctor, E. "GPU-Based Elasticity Imaging Algorithms", MICCAI-Grid Workshop, London, UK (in press)

20. Rivaz, H., Foroughi, P., Boctor, E., Zellars, R., Fichtinger, G., Hager, G., "High Resolution Ultrasound Elastography: a Dynamic Programming Approach", MICCAI Workshop, Brisbane, Australia, Oct. 2007, pp 113-121

21. Rivaz, H., Foroughi, P., Boctor, E., Zellars, R., Fichtinger, G., Hager, G., "Toward Real-Time 2D Ultrasound Elastography Using Global Optimization of a Regularized Displacement Field", 6th Int. elastography Conf., Santa Fe, NM, Nov. 2007, p 137 (oral presentation)

22. Rivaz, H., Hager, G., Zellars, R., Fichtinger, G., Boctor, E., "Speckle Characterization and Out-of-Plane Motion Estimation in Tissue", 6th Int. elastography Conf., Santa Fe, NM, Nov. 2007, p 116 (oral presentation)

23. Rivaz, H., Rohling, R., "Design of a hand-held probe for vibro-elastography," 4th Int. elastography Conf., Austin, TX, Oct. 2005, p 61 (oral presentation)

Ultrasound Elastography: A Dynamic Programming Approach

Hassan Rivaz*, Emad Boctor, Pezhman Foroughi, Richard Zellars, Gabor Fichtinger, and Gregory Hager

Abstract—This paper introduces a 2-D strain imaging technique based on minimizing a cost function using dynamic programming (DP). The cost function incorporates similarity of echo amplitudes and displacement continuity. Since tissue deformations are smooth, the incorporation of the smoothness into the cost function results in reduced decorrelation noise. As a result, the method generates high-quality strain images of freehand palpation elastography with up to 10% compression, showing that the method is more robust to signal decorrelation (caused by scatterer motion in high axial compression and nonaxial motions of the probe) in comparison to the standard correlation techniques. The method operates in less than 1 s and is thus also potentially suitable for real time elastography.

Index Terms—Dynamic programming, freehand ultrasound (US), real time strain imaging, regularization, ultrasound elastography.

I. INTRODUCTION

ELASTOGRAPHY, the computation of the spatial variation of the elastic modulus of tissue, is an emerging medical imaging method with medical applications such as tumor detection [1]. This paper focuses on static elastography, a well-known technique that applies quasi-static compression of tissue and simultaneously images it with ultrasound. Through analysis of the ultrasound images, a tissue displacement map can be obtained [2], [3]. A least squares technique is then typically used to generate a low noise strain estimate from the displacement map [2].

Despite having numerous potential clinical applications, several practical challenges have hindered wide application of static elastography. First, signal decorrelation between the precompression and postcompression images induces significant noise in the obtained displacement map and is one of the major limiting factors in elastography [4]. Major sources of signal decor-

*H. Rivaz is with the Engineering Research Center for Computer Integrated Surgery, Johns Hopkins University, 3400 N. Charles Street, Baltimore, MD 21218 USA.

E. Boctor, P. Foroughi, and G. Hager are with the Engineering Research Center for Computer Integrated Surgery, Johns Hopkins University, Baltimore, MD 21218 USA.

R. Zellars is with the Department of Radiation Oncology, Johns Hopkins University School of Medicine, Baltimore, MD 21231 USA.

G. Fichtinger is with the School of Computing, Queens University, Kingston, ON, K7L 3N6 Canada.

relation are scatterer motion in high axial compression, nonaxial motions of the probe, and physiologic motion. Most elastography techniques estimate local displacements of tissue based on correlation analysis of radio-frequency (RF) echoes [2], [3]. Large windows are required to reduce the variance (i.e., noise) of the estimated displacement and to avoid ambiguity in time delay estimation, especially when tracking a motion that exceeds one wavelength. At the same time, signal decorrelation within large windows limits the tolerable level of compression [2]–[4]. To reduce signal decorrelation, stretching methods have been proposed [5], [6], which are computationally expensive and are not suitable for real-time elastography. Moreover, large errors due to false peaks and smaller errors due to jitter [7] limit the performance of correlation techniques.

Second, in many methods, the compression is applied by a mechanical actuator in order to generate an excitation that minimizes signal decorrelation [1], [8] or because accurate motion is otherwise required by the particular elastography technique [9]. Freehand palpation elastography is a much more attractive alternative, as it requires no extra hardware and provides ease of use. It has attracted increasing interest in recent years [8], [10]–[13], however it introduces additional sources of signal decorrelation caused by operator's hand unwanted motion.

Third, elastography is computationally expensive, making it challenging to display elastograms in real time. Real-time elastography provides the feedback to the operator to best capture the region of interest in the elastogram and is required for image guided surgical operations that can potentially use elastograms. Combined autocorrelation method [14] and phase zero estimation [15] are the first work that generate real-time elastograms. Hall *et al.* [12] have presented a real-time elastography system where tissue compression is performed by freehand palpation based on a 2-D block matching algorithm. Dynamic programming is used for one A-line of the image for guiding the block matching algorithm [16]. While these methods use the displacement of each window to confine the search range for the neighboring windows, the displacement of each window is calculated independently and hence are sensitive to signal decorrelation.

In work closely related to this paper, Pellot-Barakat *et al.* [17] have proposed minimizing an energy function that combines constraints of conservation of echo amplitude and displacement continuity. Since data alone can be insufficient to solve ambiguities due to signal decorrelation, the physical priors of tissue motion continuity increases the robustness of the technique. The RF data is first upsampled by a factor of four in the axial direction. The image is then subdivided into four parts and a coarse displacement map is calculated for each part iteratively. Each part is subsequently divided into four parts and the displace-

ment of each part is calculated by the same iterative technique using the displacement of the parent grid as an initial guess. The method is shown to generate accurate low noise displacement fields. However, the computation time is reported to be more than 1 min for a strain image that is less than half of the number of pixels in the strain images generated in this paper. Hence, the method is not immediately suitable for real time elastography.

The contribution of this paper is the demonstration of the feasibility of an elastography technique based on dynamic programming (DP) for image matching [18]. Compared to other optimization techniques, DP is an efficient noniterative method of global optimization [19], [20]. However, it can only be used to optimize causal cost functions (Section II).

II. ONE-DIMENSIONAL DISPLACEMENT ESTIMATION USING DP

Devising a DP algorithm for optimization involves the following.

1) Breaking the total optimization cost into a sum of individual costs, such that each cost corresponds to a discrete decision. The decisions should follow each other sequentially and the cost corresponding to each decision should only depend on the previous and not the future decisions (causality).
2) Determining what decisions are possible at each stage.
3) Writing a recursion on the optimal cost from the first stage to the final stage.

We first consider the problem of 1-D strain estimation with 1-D smoothness regularization. Consider two echo signals $g(i)$ and $g'(i)$ corresponding to two A-lines acquired before and after compression (Fig. 1, left), each signal sampled at $i = 1, 2 \cdots m$. The difference between the two signals Δ can be quantified using sum of absolute differences (SAD), which is computationally inexpensive to compute and has been shown to have good robustness against outliers [21], [20]

$$\Delta(i, d) = |g(i) - g'(i + d)| \quad (1)$$

where $d_{\min} \leq d \leq d_{\max}$ is the displacement at the sample i (Fig. 1, left) and $d_{\min}$ and $d_{\max}$ specify the allowed displacement. Gains of RF data can be changed in ultrasound machines to improve visualization. To reduce the effect of these changes on Δ, both precompression and postcompression ultrasound images are divided by the maximum value of one of the images. The smoothness of the displacements is S

$$S(d_i, d_{i-1}) = (d_i - d_{i-1})^k \quad (2)$$

where d_i is the displacement at the sample i and d_{i-1} is the displacement at the sample $i - 1$ of the $g(i)$. To avoid large jumps in the displacement, S should be strictly convex

$$\alpha (d_{i1} - d_{i-1})^k + (1 - \alpha) (d_{i2} - d_{i-1})^k > [\alpha d_{i1} + (1 - \alpha) d_{i2} - d_{i-1}]^k, \quad 0 < \alpha < 1 \quad (3)$$

i.e., a small jump and a large jump (left-hand side) are penalized more than two medium jumps (right-hand side). This holds for even k, we choose $k = 2$: for $k > 2$ larger jumps are more heavily penalized which adversely affects contrast to noise ratio.
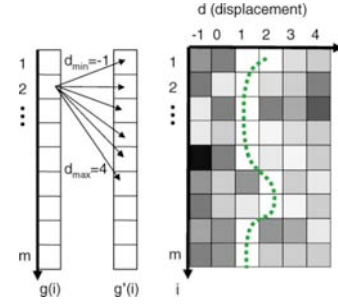

Fig. 1. In the left, values of $g(i)$ and $g'(i+d)$ corresponding to precompression and postcompression RF data are compared. Right shows the cost function C of (4) (white and black represent low and high cost values, respectively).

The cost function C at a point i and associated displacement d_i is defined as a recursive function

$$C(i, d_i) = \min_{d_{i-1}} \{C(i - 1, d_{i-1}) + wS(d_i, d_{i-1})\} + \Delta(i, d_i) \quad (4)$$

where w is a regularization weight which governs smoothness. The study of its effect on the estimated displacement is postponed to the discussion of 2-D displacement estimation in Section III-A. The values of the C function are stored in a $(d_{\max} - d_{\min} + 1) \times m$ matrix (Fig. 1, right).

Generally, the optimum value of d_{i-1} should be sought in the entire $[d_{\min}, d_{\max}]$ range. However, since the strain value is low in elastography, it is expected and desired that at each sample of RF data, the change between the displacement of a sample and its previous sample is not more than 1. Therefore, the search range of optimum value for d_{i-1} is limited to the three values of $d_i - 1$, d_i and $d_i + 1$, which results in a significant gain in speed. This limit on the search range does not affect the results even in a high strain of 10%: Δd is zero for nine samples and one for the tenth sample on average. The value of d_{i-1} that minimizes (4) is also "memoized" [19] in a function M for later use

$$M(i, d_i) = \arg\min_{d_{i-1}} \{C(i - 1, d_{i-1}) + wS(d_i, d_{i-1})\}. \quad (5)$$

The cost function C is calculated for $i = 1 \cdots m$. The minimum cost at $i = m$ gives the displacement of this point, which is traced back to $i = 1$ using the M function to calculate all the displacements (D)

$$D(i) = \arg\min_{d_i} \{C(i, d_i)\}, \ i = m$$
$$D(i) = M(i + 1, D(i + 1)), \ i = 1 \cdots m - 1. \quad (6)$$

The displacement map of all A-lines is calculated using the same procedure independently. In Section III, we present a method for coupling adjacent A-lines.

A. Hierarchical Search and Subpixel Displacement Estimation

Further speedup is achieved by downsampling the signal $g(i)$ by a factor of β to $g^*(i)$, and comparing it with the unaltered signal $g'(i)$. This is done by simply skipping $\beta - 1$ samples from $g(i)$ and performing DP on the βth sample, as illustrated in Fig. 2 left. This generates *integer displacement* estimations at m/β samples. The displacement of the skipped samples is then
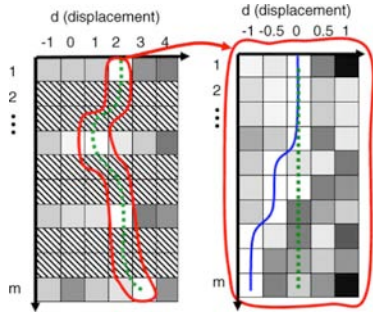
Fig. 2. In the left, the cost function C is shown when DP is performed on $g^*(i)$ ($g(i)$ downsampled by a factor of β) and $g'(i)$ (not downsampled). Hashed squares indicate no cost calculation is performed due to downsampling of $g(i)$, and white and black representing low and high cost values respectively. Displacement is calculated at m/β samples in this stage ($\beta = 3$ in this figure). In right, a new cost function around the optimum path of the first stage's cost function (the dashed line) is created, giving a $1/\gamma = 1/2$ pixel displacement accuracy at m samples.

simply approximated by the linear interpolation of two neighboring points whose displacements are calculated, as an initial guess for the next step.

The displacement estimates are then refined to *subpixel displacement* estimation at all m samples. The original signal $g(i)$ (not downsampled) is compared with $g'(i + d)$ upsampled by a factor of γ (Fig. 2 right) using parabolic interpolation. Repeating the refinement procedure n times results in a refinement factor of $1/\gamma^n$.

In cross correlation methods, subsample displacement is usually achieved by interpolation of the correlation function [22], which is subject to bias and jitter [22], [23]. Here, we interpolate the original RF data instead, which is shown to have similar performance [23]. Although cosine-fit outperforms parabolic-fit interpolation in terms of bias and jitter [22], [23], the latter is used here for computational simplicity.

B. Results

For experimental evaluation, RF data was acquired from an Antares Siemens system (Issaquah, WA) with a 7.27-MHz linear array at a sampling rate of 40 MHz. For the purposes of comparison, strain images were also calculated using a standard cross correlation method with a 3-mm window size and 80% overlap and a three point parabolic interpolation to find the subsample location of the correlation peak [22]. Linear regression with a 5-sample window is performed on the displacement field to calculate strain. Normalization was performed to decrease the dynamic range of the strain images: any strain value outside $\bar{s} \pm 3\sigma$ was set to $\bar{s} \pm 3\sigma$ to eliminate the outliers in the strain map ($\bar{s}$ and σ are the mean and standard deviation of the strain values across the whole image). The unitless performance metric signal-to-noise ratio (SNR) and contrast-to-noise ratio (CNR) were calculated according to [2]

$$\mathrm{CNR} = \frac{C}{N} = \sqrt{\frac{2(\bar{s}_b - \bar{s}_t)^2}{\sigma_b^2 + \sigma_t^2}}, \quad \mathrm{SNR} = \frac{\bar{s}}{\sigma} \quad (7)$$

where $\bar{s}_t$ and $\bar{s}_b$ are the spatial strain average of the target and background, σ_t^2 and σ_b^2 are the spatial strain variance of the
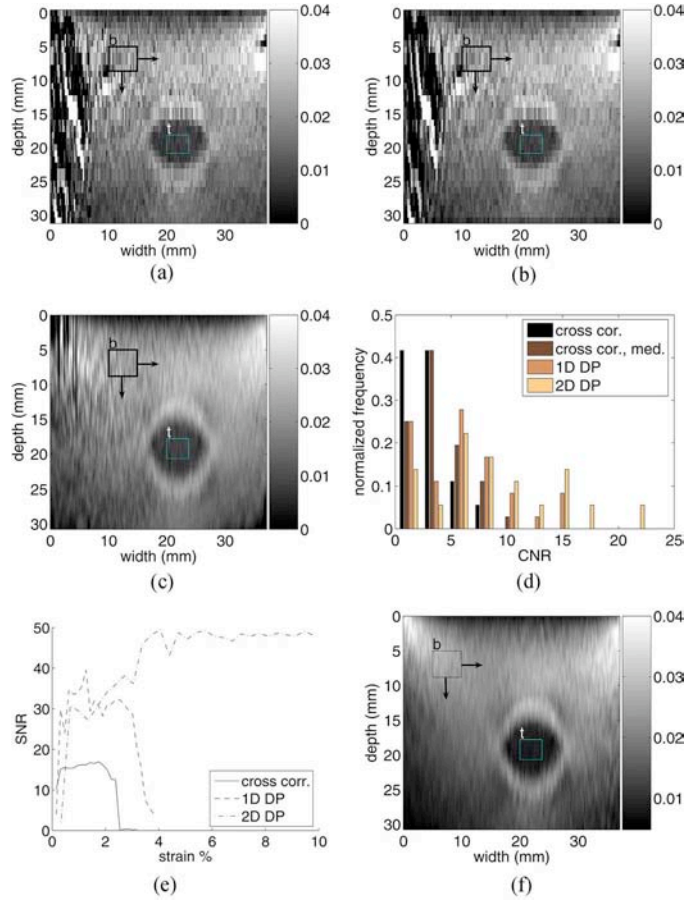

Fig. 3. (a)-(c) strain images obtained from freehand palpation of the phantom using cross correlation, cross correlation with a 3×3 median filter applied on the displacement image and 1-D DP respectively. The target window is fixed on the lesion and the background window is moved to allow multiple CNR calculation. (d) Normalized CNR values of the lesion, obtained by dividing each bin by the total of 36 CNR measurements. (e) SNR values of the cross correlation and 1-D DP techniques. (f) Strain images obtained from freehand palpation of the phantom using 2-D DP.

target and background, and $\bar{s}$ and σ are the spatial average and variance of a window in the strain image, respectively.

In the first experiment, a breast elastography phantom (CIRS, Norfolk, VA) with a lesion of 10 mm diameter and three times stiffer than the background was palpated freehand. In consecutive images, where axial compression is low and there is little nonaxial motion, both methods perform well. However, as the axial compression and attendant nonaxial motion increase, the DP method outperforms the cross correlation method. Fig. 3(a) shows the strain image obtained with cross correlation. In Fig. 3(b), a 3×3 median filter is applied to the displacement measurements, before differentiation, as a 2-D continuity check. Fig. 3(c) shows the strain image obtained with the 1-D DP method. A high level of lateral motion, slightly more than 2 A-lines, at the left of the image and high axial strain cause the cross correlation method to fail. To calculate the CNR values the target window was selected as specified in the figure. The background window was then moved across the strain image (with 3.8 mm margin from all four sides and from the lesion where the strain is expected to vary considerably) to allow for a more comprehensive CNR measurement. The histogram of Fig. 3(d) shows that 1-D DP gives better CNR values: the

mean value of the 36 CNR measurements for cross correlation, cross correlation with the 3×3 median filter, and 1-D DP are, respectively, 2.60, 3.98, and 6.24. The standard deviation value of CNR for cross correlation, cross correlation with the 3×3 median filter, and 1-D DP are, respectively, 2.08, 2.70, and 4.27, reflecting the changes in strain across the image caused by medium inhomogeneity and nonuniform loading condition.

To obtain a strain filter [2], a CIRS elasticity QA phantom with the Young's modulus of 33 kPa was compressed in 24 steps, each step 0.005 in. The experiment was performed far from the lesions of the phantom to generate close to uniform strain due to a uniform compression. The strain map between the first frame and all other frame was calculated using the cross correlation and DP methods. The SNR metric was calculated in a small window located at the top center of the image, where strain is approximately constant. Fig. 3(e) shows that the 1-D DP method has a higher dynamic range, an important elastography performance metric [2].

III. 2-D DISPLACEMENT ESTIMATION

Until now, we have assumed pure axial compression independently estimated on each A-line. However, lateral displacement in a soft material is inevitable even when it undergoes pure axial compression. This displacement is related to the Poisson's ratio, which describes the material compressibility. Also, freehand palpation is rarely a pure compression and thus also results in nonaxial tissue motion. As a result, a 2-D smoothness regularization that considers the displacements between adjacent A-lines is more natural. The DP algorithm of Section II is modified here to allow for 2-D displacement estimation and 2-D smoothness regularization.

Assuming that ultrasound images consist of n A-lines, the distance between the pre and postcompression signals is

$$\Delta(i, j, d_a, d_l) = \left| g_j(i) - g'_{j+d_l}(i + d_a) \right| \qquad (8)$$

where $d_{a,\min} \leq d_a \leq d_{a,\max}$ and $d_{l,\min} \leq d_l \leq d_{l,\max}$ are the axial and lateral displacements, respectively, and $j = 1 \cdots n$ refers to jth A-line and $i = 1 \cdots m$

$$S(d_{a_i}, d_{l_i}, d_{a_{i-1}}, d_{l_{i-1}}) = (d_{a_i} - d_{a_{i-1}})^2 + (d_{l_i} - d_{l_{i-1}})^2 \quad (9)$$

is the smoothness regularization with subscripts a and l referring to axial and lateral. The cost function at the ith sample of the jth A-line is

$$C_j(d_a, d_l, i) = \Delta(d_a, d_l, i) + \min_{\delta_a, \delta_l}$$
$$\left\{ \frac{C_j(\delta_a, \delta_l, i-1) + C_{j-1}(\delta_a, \delta_l, i)}{2} + wS(d_a, d_l, \delta_a, \delta_l) \right\}. \quad (10)$$

For memoization, δ_a and δ_l values that minimize the cost function are stored for all d_a, d_l and i values. The specific form of the cost function allows the calculation of the displacement of each A-line using the cost values of the previous A-line. The cost function of the jth line, $C_j(d_a, d_l, i)$, is calculated and is minimized, resulting in its displacement map. The $C_j(d_a, d_l, i)$ function is also used for the calculation of the next cost function
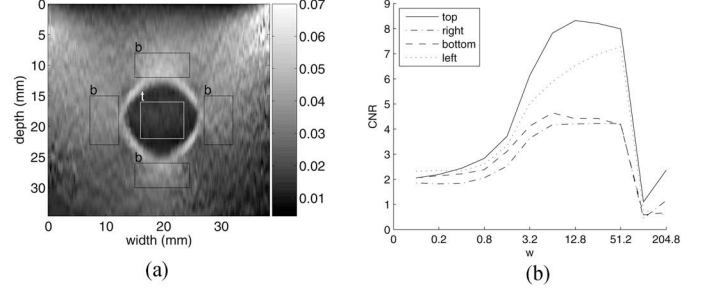

Fig. 4. Two-dimensional DP results of freehand palpation of the breast phantom. (a) Strain image with the target window and four background windows for CNR calculation. (b) CNR values between the target window and the four background windows on the top, right, bottom and left of the lesion calculated for different regularization coefficient values w in (10).

$C_{j+1}(d_a, d_l, i)$ and is deleted from the memory afterward. This makes the amount of memory required to store the cost function values independent of the number of A-lines.

A. Results

To study the effect of the regularization weight w on the CNR, the breast phantom is palpated freehand. For two RF frames, the elastogram is obtained using the 2-D DP algorithm with different w values. CNR is calculated between the shown target window and the four background windows on top, right, bottom, and left of the lesion (Fig. 4). At low w values, CNR is low because of high noise in the windows, while at high w values CNR drops because high displacement changes are heavily penalized. $3 < w < 50$ is optimizing the tradeoff between noise and contrast to maximize CNR, both in the lateral (background windows on the right and left of the target) and axial (background windows on the top and bottom of the target) directions. Since the background windows are close to the lesion, the strain within each window is not expected to be constant even though the phantom is homogeneous within them. This variation in the ground truth strain will be reflected as noise in the CNR calculation which is undesirable. However, we have selected the windows such that they best capture the effect of w on CNR close to an inhomogeneity, which also contains some resolution information.

Fig. 3(f) shows the strain image obtained using the 2-D DP method using the same two frames that are used to generate the strain images in Fig. 3(a)–(c). The CNR values [Fig. 3(d)] are calculated for the same target and 36 background windows as before, giving a mean of 8.96 and a standard deviation of 5.75. Since the elasticity QA phantom cannot be compressed more than 4%, we use the breast phantom for experimental evaluation of the strain filter of the 2-D DP method. Fig. 3(e) shows the SNR values, showing no degradation of the SNR even at a high strain of 10%. Comparing these results with the 1-D DP and cross correlation results, a significant increase in the image quality, CNR value, and maximum allowed strain is achieved.

Substituting other computationally more expensive similarity measures like normalized cross correlation in the Δ function resulted in no significant difference in the performance. Currently, the algorithm takes 0.72 s to calculate the displacement map of each pixel in an image with 1000×100 pixels with maximum

axial displacement of 10 samples (1% strain) and maximum lateral displacement of ± 1 A-lines on a 3.8 GHz P4 CPU. The current implementation is in MATLAB with the DP optimization in mex functions.

IV. DISCUSSION AND CONCLUSION

The lateral search is performed in the 2-D DP method only to decrease the noise and increase the robustness of the axial strain: the lateral displacements are integer values and are not suitable for calculating lateral strain. Results of Fig. 3 show that DP is more robust to the signal decorrelation (caused by scatterer motion in high axial compression, and lateral and out of plane motions of the probe) than standard cross correlation techniques. This is critically important since it tolerates higher axial compression [Fig. 3(e)], increasing the dynamic range of the elastogram which is crucial for lesion detection. Nonlinear elastic properties of tissue also only appear at high strain values [3]. It also generates low-noise elastograms using almost any two frames in freehand palpation, given that they both belong to the same compression or relaxation cycle of the palpation excitation. Finally, no postprocessing step such as median filtering is required.

The CNR and SNR metrics seem to indicate that the regularization creates smooth elastograms while preserving contrast. The only tunable parameter of the method, w in (10), was kept constant at $w = 10$ throughout this work. It can also be varied between 5 and 50, as Fig. 4 indicates, with almost no effect on CNR. This might indicate that the w value optimized for phantom will work well for real tissue. These features of the DP, along with its high speed make it a promising elastography method.

DP strain images in Figs. 3 and 4 show some stress concentration around the lesion which is not seen in the corresponding cross correlation images. We are not sure yet whether this is an artifact or high strains are created just around the lesion because of nonlinear mechanical properties of the phantom. We are planning for validation of the estimated displacement of DP using simulation and laboratory experiments for clarification. High strain is also seen on the top edges in both cross correlation and DP images. The curved shape of the breast phantom is probably the reason for this high strain: in order for the edges of the probe to touch the phantom, the part of the phantom just under middle of the probe has to compress considerably. If the phantom material hardens under high strains, the phantom around the edges experiences higher strain. The absence of this stress concentration in our experiments with noncurved phantoms seems to prove this.

We have chosen to use the cross correlation as a comparative benchmark to assess the potential of DP. This is because cross correlation is the most commonly used method and has been shown to accomplish at least as accurate results as any other method, and thus it represents a "gold-standard" [24], [23]. However, we are planning for a comprehensive comparison of the DP with other strain imaging techniques. Further work is required to study the effect of regularization on resolution [25]. To achieve real-time performance in freehand palpation imaging, an adaptive search range selection can be implemented by using the continuity of displacement in time to confine the search. The 2-D algorithm can be extended to 2-D + t to exploit the cost function in previous time, optimize frame selection [26], and incorporate a 2-D + t regularization.

REFERENCES

[1] B. Garra, E. Céspedes, J. Ophir, S. Spratt, R. Zuurbier, C. Magnant, and M. Pennanen, "Elastography of breast lesions: Initial clinical results," *Radiology*, vol. 202, pp. 79–86, 1997.

[2] J. Ophir, S. Alam, B. Garra, F. Kallel, E. Konofagou, T. Krouskop, and T. Varghese, "Elastography: Ultrasonic estimation and imaging of the elastic properties of tissues," *Annu. Rev. Biomed. Eng.*, vol. 213, pp. 203–233, Nov. 1999.

[3] J. Greenleaf, M. Fatemi, and M. Insana, "Selected methods for imaging elastic properties of biological tissues," *Annu. Rev. Biomed. Eng.*, vol. 5, pp. 57–78, Apr. 2003.

[4] T. Varghese, J. Ophir, E. Konofagou, F. Kallel, and Righetti, "Tradeoffs in elastographic imaging," *Ultrason. Imag.*, vol. 23, pp. 216–248, 2001.

[5] T. Varghese and J. Ophir, "Enhancement of echo-signal correlation in elastography using temporal stretching," *IEEE Trans. Ultrason. Ferroelectr. Freq. Control*, vol. 44, no. 1, pp. 173–180, Jan. 1997.

[6] P. Chaturvedi, M. Insana, and T. Hall, "2-D companding for noise reduction in strain imaging," *IEEE Trans. Ultrason. Ferroelectr. Freq. Control*, vol. 45, no. 1, pp. 179–191, Jan. 1998.

[7] W. Walker and G. Trahey, "A fundamental limit on delay estimation using partially correlated speckle signals," *IEEE Trans. Ultrason. Ferroelectr. Freq. Control*, vol. 42, no. 2, pp. 301–308, Mar. 1995.

[8] K. Hiltawsky, M. Kruger, C. Starke, L. Heuser, H. Ermert, and A. Jensen, "Freehand ultrasound elastography of breast lesions: Clinical results," *Ultrasound Med. Biol.*, vol. 27, pp. 1461–1469, 2001.

[9] H. Rivaz and R. Rohling, "An active dynamic vibration absorber for a hand-held vibro-elastography probe," *ASME Trans. Vibration Acoustics*, vol. 129, pp. 101–112, Feb. 2007.

[10] M. Doyley, J. Bamber, F. Fuechsel, and N. Bush, "A freehand elastographic imaging approach for clinical breast imaging: System development and performance evaluation," *Ultrasound Med. Biol.*, vol. 27, pp. 1347–1357, 2001.

[11] M. Yamakawa, N. Nitta, T. Shiina, T. Matsumura, S. Tamano, T. Mitake1, and E. Ueno, "High-speed freehand tissue elasticity imaging for breast diagnosis," *Jpn. J. Appl. Phys.*, vol. 42, pp. 3265–3270, May 2003.

[12] T. Hall, Y. Zhu, and C. Spalding, "In vivo real-time freehand palpation imaging," *Ultrasound Med. Biol.*, vol. 29, pp. 427–435, Mar. 2003.

[13] J. Lindop, G. Treece, A. Gee, and R. Prager, "3D elastography using freehand ultrasound," *Ultrasound Med. Biol.*, vol. 32, pp. 529–545, 2006.

[14] T. Shiina, M. Doyley, and J. Bamber, "Strain imaging using combined RF and envelope autocorrelation processing," in *IEEE Ultrason. Symp.*, San Antonio, TX, 1996, pp. 1331–1336.

[15] A. Pesavento, C. Perrey, M. Krueger, and H. Ermert, "A time-efficient and accurate strain estimation concept for ultrasonic elastography using iterative phase zero estimation," *IEEE Trans. Ultrason. Ferroelectr. Freq. Control*, vol. 46, no. 5, pp. 1057–1067, Sep. 1999.

[16] J. Jiang and T. Hall, "A regularized real-time motion tracking algorithm using dynamic programming for ultrasonic strain imaging," in *IEEE Ultrason. Symp.*, Vancouver, BC, Canada, Oct. 2006, pp. 606–609.

[17] C. Pellot-Barakat, F. Frouin, M. Insana, and A. Herment, "Ultrasound elastography based on multiscale estimations of regularized displacement fields," *IEEE Trans. Med. Imag.*, vol. 23, no. 2, pp. 153–163, Feb. 2004.

[18] E. Boctor, G. Fichtinger, G. Hager, and H. Rivaz, "Apparatus and method for computing 3D ultrasound elasticity images," U.S. Patent 26148.071.00us, Jun. 2006.

[19] R. Bellman, *Applied Dynamic Programming*. Princeton, NJ: Princeton Univ. Press, 1962.

[20] M. Brown, D. Burschka, and G. Hager, "Advances in computational stereo," *IEEE Trans. Pattern Anal. Mach. Intell.*, vol. 25, no. 8, pp. 993–1008, Aug. 2003.

[21] P. Huber, *Robust Statistics*. New York: Wiley, 1981.

[22] I. Céspedes, Y. Huang, J. Ophir, and S. Spratt, "Methods for estimation of subsample time delays of digitized echo signals," *Ultrason. Imag.*, vol. 17, pp. 142–171, Apr. 1995.

[23] F. Viola and W. Walker, "A spline-based algorithm for continuous time-delay estimation using sampled data," *IEEE Trans. Ultrason. Ferroelectr. Freq. Control*, vol. 52, no. 1, pp. 80–93, Jan. 2005.

[24] F. Viola and W. Walker, "A comparison of the performance of time-delay estimators in medical ultrasound," *IEEE Trans. Ultrason. Ferroelectr. Freq. Control*, vol. 50, no. 4, pp. 392–401, Apr. 2003.

[25] J. Liu, K. Abbey, and M. Insana, "Linear approach to axial resolution in elasticity imaging," *IEEE Trans. Ultrason. Ferroelectr. Freq. Control*, vol. 51, no. 6, pp. 716–725, Jun. 2004.

[26] M. Lubinski, S. Emelianov, and M. O'Donnell, "Adaptive strain estimation using retrospective processing," *IEEE Trans. Ultrason. Ferroelectr. Freq. Control*, vol. 46, no. 1, pp. 97–107, Jan. 1999.

Real-Time Regularized Ultrasound Elastography

Hassan Rivaz*, Emad M. Boctor, Michael A. Choti, and Gregory D. Hager

Abstract—**This paper introduces two real-time elastography techniques based on analytic minimization (AM) of regularized cost functions. The first method (1D AM) produces axial strain and integer lateral displacement, while the second method (2D AM) produces both axial and lateral strains. The cost functions incorporate similarity of radio–frequency (RF) data intensity and displacement continuity, making both AM methods robust to small decorrelations present throughout the image. We also exploit techniques from robust statistics to make the methods resistant to large local decorrelations. We further introduce Kalman filtering for calculating the strain field from the displacement field given by the AM methods. Simulation and phantom experiments show that both methods generate strain images with high SNR, CNR and resolution. Both methods work for strains as high as 10% and run in real-time. We also present *in vivo* patient trials of ablation monitoring. An implementation of the 2D AM method as well as phantom and clinical RF-data can be downloaded.**

Index Terms—**Kalman filter, radio-frequency (RF) ablation, real-time ultrasound elastography, regulariation, robust estimation, two-dimensional (2D) strain.**

I. INTRODUCTION

ELASTOGRAPHY involves imaging the mechanical properties of tissue and has numerous clinical applications. Among many variations of ultrasound elastography [1]–[4], our work focuses on real-time static elastography, a well-known technique that applies quasi-static compression of tissue and simultaneously images it with ultrasound. Within many techniques proposed for static elastography, we focus on freehand palpation elasticity imaging which involves deforming the tissue by simply pressing the ultrasound probe against it. It requires no extra hardware, provides ease of use and has attracted increasing interest in recent years [5]–[10]. Real-time elastography is of key importance in many diagnosis applications [11], [6], [12], [8], [13] and in guidance/monitoring of surgical operations [14]–[16].

Global and local decorrelation between the pre- and post-compression ultrasound images compromises the quality of the elasticity images. The main sources of global decorrelation in freehand palpation elastography are change of speckle appearance due to scatterer motion and out-of-plane motion of the probe (axial, lateral and out-of-plane directions are specified in Fig. 1). Examples of local decorrelation are: 1) a decrease in the ultrasonic signal to noise ratio with depth, 2) low correlation close to arteries due to complex motion and inside blood vessels due to blood motion, 3) extremely low correlation in lesions that contain liquid due to the incoherent fluid motion [17], [8], and 4) out-of-plane motion of movable structures within the image [17].

Most elastography techniques estimate local displacements of tissue based on amplitude correlation [18], [2] or phase correlation of the radio-frequency (RF) echoes [19]–[21]. Assuming a stationary signal model for the RF data, the use of large correlation windows helps to reduce jitter errors (variance) for all motion field estimation techniques studied in [18] and [22]. This is intuitive as larger windows contain more information. However, in practice RF data is not stationary and, for large deformations, the decorrelation increases with window size. Therefore, in addition to reducing the spatial resolution [23], larger windows result in significant signal decorrelation [24], [23], [18]. Coarse-to-fine hierarchical search is used in [23] to combine the accuracy of large windows with the good spatial resolution of small window. However, the issue of signal decorrelation within the window remains unresolved in this approach and can cause the highest level of the hierarchical search to fail.

All of the aforementioned methods either do not calculate the lateral displacement or they just calculate an approximate integer lateral displacement. A 2D displacement field is required to calculate the thermal expansion, lateral and shear strain fields [25] (i.e., reconstruct the strain tensor), Poisson's ratio and Young's modulus [26], [27]. The axial resolutions of ultrasound is determined by the pulse length, and the lateral resolutions is dictated by the center frequency of the excitation and the transducer pitch. Therefore, the lateral resolution is of order of magnitude lower than axial resolution. As a result, few 2D elastography techniques have been proposed to date. Initially, 2D motion estimation started in the field of blood flow estimation using speckle tracking [28]. Designed for blood flow estimation, these techniques are not immediately suitable for elastography which involves tissue deformation.

Attaching a coordinate system to the ultrasound probe as in Fig. 1, z, x, and y in the ultrasound image are generally defined as axial, lateral and out-of-plane directions. Assume that the applied compression to the tissue is the Z direction, and attach a coordinate system X, Y, Z to the applied force. Letting d_Z and d_N be the displacements in the Z and N directions where $N \perp Z$, axial and transverse strains are $\partial d_Z / \partial Z$ and $\partial d_N / \partial N$. In most experimental setups (including freehand palpation elastography), z and Z are parallel and N will be either lateral or out-of-plane, and therefore d_N cannot be estimated accurately.

*H. Rivaz is with the Engineering Research Center for Computer Integrated Surgery, Johns Hopkins University, Baltimore, MD 21218 USA.

E. Boctor and G. Hager are with the Engineering Research Center for Computer Integrated Surgery, Johns Hopkins University, Baltimore, MD 21218 USA.

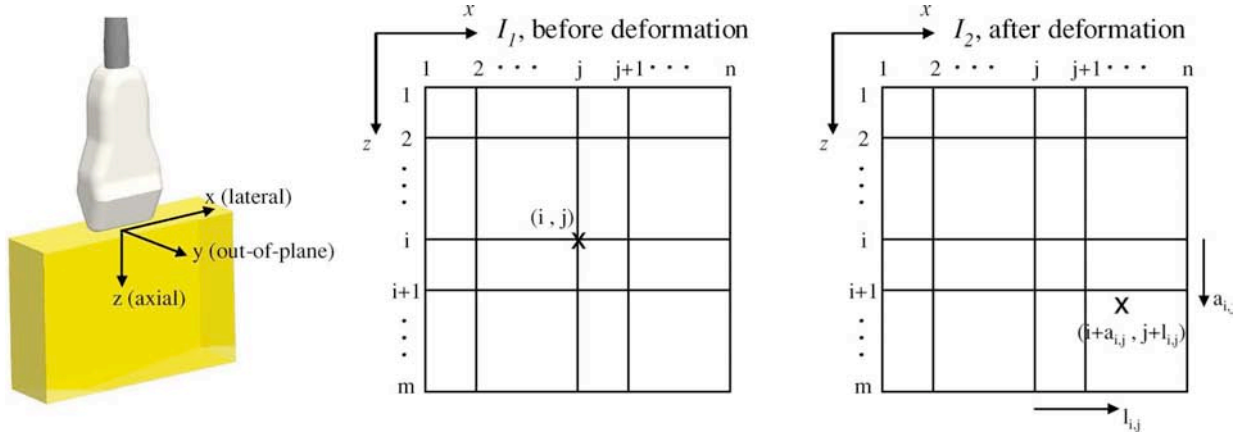M. Choti is with the Department of Surgery, Johns Hopkins Medicine, Baltimore, MD 21218 USA.

Fig. 1. Axial, lateral, and out-of-plane directions. The coordinate system is attached to the ultrasound probe. The sample (i,j) marked by x moved by $(a_{i,j}, l_{i,j})$. $a_{i,j}$ and $l_{i,j}$ are, respectively, axial and lateral displacements and initially are integer in DP.

To calculate an accurate transverse strain, Z and z are perpendicular in [29] by applying the compression force perpendicular to the ultrasound imaging axis. Therefore, transverse strain is in the z direction of the ultrasound probe and hence can be measured with high accuracy. However, such an experimental setup is not possible in many medical applications. Beam steering has been used to solve this issue [30]. In freehand palpation elastography, beam steering causes z and Z to be unparallel, so that a component of the d_X is in the z direction. The steering angle determines the angle between z and Z. Unfortunately, large steering angles are required to obtain accurate estimates of lateral strain, which is possible in phased arrays and not in linear arrays.

Lateral strain[1] estimation is obtained in [31] by iteratively calculating axial strain, companding RF data and interpolating in the lateral direction. In another work [32], tissue deformation is modeled by locally affine transformations to obtain both lateral and axial strains. Change of speckle appearance is taken into account by proposing a Lagrangian speckle model [33]. Although they provide high quality lateral strain, these techniques are computationally expensive and are not suitable for real-time implementation.

Axial strain is used in [34] to enhance the quality of lateral displacement estimation. Tissue is assumed to be incompressible and isotropic and therefore axial, lateral and out-of-plane strains should add to zero. However, many tissues cannot be considered incompressible. In fact, some research has even focused on imaging the ratio of the axial and lateral strain (i.e., the Poisson's ratio ν) [31].

While most previously mentioned methods use tissue motion continuity to confine the search range for the neighboring windows, the displacement of each window is calculated independently and hence is sensitive to signal decorrelation. Since data alone can be insufficient due to signal decorrelation, Pellot-Barakat *et al.* [35] proposed minimizing a regularized energy function that combines constraints of conservation of echo amplitude and displacement continuity. In another work [36], both signal shift and scale are found through minimization of a regu-

larized cost function. The computation time of these methods is reported to be few minutes and therefore are not immediately suitable for real time elastography. In [37] and [38], few phase-based methods are regularized and strain and elasticity modulus images are obtained. The regularization term is the Laplacian (second derivative) of the motion field and is spatially variant based on the peak-value of the correlation coefficient. The regularization makes the method significantly more robust to signal decorrelation. However, it is still prone to decorrelation within each window especially for large strain rates. In a recent work [39], a displacement field is first calculated by minimizing phase differences in correlation windows [21]. The strain image is then estimated from the displacement field by optimizing a regularized cost function. The regularization assures smooth strain image calculation from the noisy displacement estimates.

Dynamic programming (DP) can be used to speed the optimization procedure [40], but it only gives integer displacements. Subsample displacement estimation is possible [40], but it is computationally expensive, particularly if subsample accuracy is needed in both axial and lateral directions. Therefore, only axial subsample displacement is calculated [40]. In addition, a fixed regularization weight is applied throughout the image. To prevent regions with high local decorrelation from introducing errors in the displacement estimation one should use large weights for the regularization term, resulting in oversmoothing.

In this paper, we present two novel real-time elastography methods based on analytic minimization (AM) of cost functions that incorporate similarity of echo amplitudes and displacement continuity. Similar to DP, the first method gives subsample axial and integer lateral displacements. The second method gives subsample 2D displacement fields and 2D strain fields. The size of both displacement and strain fields is the same size as the RF-data (i.e., the methods are not window based and the displacement and strain fields are calculated for all individual samples of RF-data). We introduce a novel regularization term and demonstrate that it minimizes displacement underestimation caused by smoothness constraint. We also introduce the use of robust statistics implemented via iterated reweighted least squares (IRLS) to treat uncorrelated ultrasound data as

---

[1]We hereafter assume the applied force is in the z direction (i.e., Z and z are parallel) and therefore we use the term lateral strain instead of the term transverse strain.

outliers. Finally, for the first time to the best of our knowledge we introduce the use of Kalman filtering [41] for calculating strain image from the displacement field. Simulation and experimental results are provided for quantitative validation. The paper concludes with a clinical pilot study utilizing this system for monitoring thermal ablation in patients with liver tumors.

II. METHODS

Assume that the tissue undergoes a deformation and let I_1 and I_2 be two images acquired from the tissue before and after the deformation. Letting I_1 and I_2 be of size $m \times n$ (Fig. 1), our goal is to find two matrices A and L where the (i, j)th component of $A(a_{i,j})$ and $L(l_{i,j})$ are the axial and lateral motion of the pixel (i, j) of I_1 (we are not calculating the out-of-plane motion). The axial and lateral strains are easily calculated by spatially differentiating A in the axial direction (resulting in A_a) and L in the lateral direction (resulting in L_l). The shear strains (not calculated in this work) can also be easily calculated by spatially differentiating A in the lateral direction (resulting in A_l) or L in the axial direction (resulting in L_a).

In this section, we first give a brief overview of a previous work (DP) that calculates integer values for A and L. We then propose 1D analytic minimization (AM) as a method that takes the integer displacement field from DP and refines the axial displacement component. We then introduce 2D analytic minimization (AM) that takes the integer displacement of a single RF-line from DP and gives the subsample axial and lateral displacement fields for the entire image. We conclude this section by presenting a technique for calculating smooth strain field from the displacement field using Kalman filtering.

A. Dynamic Programming (DP)

In order to present the general DP formulation, we consider a single column j (an RF-line) in I_1 (the image before deformation) in Fig. 1. Let m and n be the length of the RF-lines and the number of RF-lines in the images (Fig. 1). Let a_i and l_i denote the axial and lateral displacements of the ith sample of the RF-line in column j. In DP elastography [40], a regularized cost function is generated by adding the prior of displacement continuity (the regularization term) to an amplitude similarity term. The displacement continuity term for column j is

$$R_j(a_i, l_i, a_{i-1}, l_{i-1}) = \alpha_a(a_i - a_{i-1})^2 + \alpha_l(l_i - l_{i-1})^2 \quad (1)$$

which forces the displacements of the sample i (i.e., a_i and l_i) be similar to the displacements of the previous sample $i - 1$ (i.e., a_{i-1} and l_{i-1}). α_a and α_l are axial and lateral regularization weights respectively. We write $R_j(a_i, l_i, a_{i-1}, l_{i-1})$ to indicate the dependency of a_i and l_i on j. The regularized cost function for column j is then generated as following:

$$
\begin{aligned}
C_j&(a_i, l_i, i) \\
&= [I_1(i, j) - I_2(i + a_i, j + l_i)]^2 \\
&\quad + \min_{d_a, d_l}\left\{ \frac{C_j(d_a, d_l, i-1) + C_{j-1}(d_a, d_l, i)}{2} \right. \\
&\quad \left. + R_j(a_i, l_i, d_a, d_l) \right\}
\end{aligned}
\quad (2)
$$

where d_a and d_l are temporary displacements in the axial and lateral directions that are varied to minimize the term in the bracket. After calculating C_j for $i = 2 \ldots m$, C_j is minimized at $i = m$ giving a_m and l_m. The a_i and l_i values that have minimized the cost function at $i = m$ are then traced back to $i = 1$, giving integer a_i and l_i for all samples of jth line. The process is performed for the next line $j + 1$ until the displacement of the whole image is calculated. The 2D DP method gives integer axial and lateral displacement maps. In [40], we performed hierarchical search to obtain subsample axial displacement (the lateral displacement was not refined to subsample). DP is an efficient method for global optimization and has been used extensively in many applications in computer vision including solving for optimal deformable models [42]. In the next section, we propose an alternative method for calculating subsample axial displacement which is both faster and more robust than hierarchical DP.

B. 1D Analytic Minimization (AM)

Tissue deformations in ultrasound elastography are usually very small and therefore a subsample displacement estimation is required. We now develop a method that analytically minimizes a regularized cost function and gives the refined displacement field following the work presented in [16]. We first consider a specialization of (2) in which we only consider refining axial displacements to subsample level.

Having the integer displacements a_i and l_i from DP, it is desired to find Δa_i values such that $a_i + \Delta a_i$ gives the value of the displacement at the sample i for $i = 1 \ldots m$ (l_i, a_i and Δa_i correspond to line j. Hereafter, wherever the displacements correspond to the jth line, j is omitted to prevent notation clutter). Such Δa_i values will minimize the following regularized cost function:

$$
\begin{aligned}
C_j&(\Delta a_1, \ldots, \Delta a_m) \\
&= \sum_{i=1}^{m}\{[I_1(i, j) - I_2(i + a_i + \Delta a_i, j + l_i)]^2 \\
&\quad + \alpha_a(a_i + \Delta a_i - a_{i-1} - \Delta a_{i-1})^2 \\
&\quad + \alpha_l(a_i + \Delta a_i - a_{i,j-1} - \Delta a_{i,j-1})^2]\}
\end{aligned}
\quad (3)
$$

where $\alpha_a > 0$ and $\alpha_l > 0$ are tunable axial and lateral regularization weights and subscript $j-1$ refers to the previous RF-line (adjacent RF-line in the lateral direction).

Substituting $I_2(i + d_i + \Delta d_i)$ with its first-order Taylor expansion approximation around d_i, we have

$$
\begin{aligned}
C_j&(\Delta a_1, \ldots, \Delta a_m) = \sum_{i=1}^{m}\{[I_1(i, j) \\
&\quad - I_2(i + a_i, j + l_i) - I_2'(i + a_i, j + l_i)\Delta a_i]^2 \\
&\quad + \alpha_a(a_i + \Delta a_i - a_{i-1} - \Delta a_{i-1})^2 \\
&\quad + \alpha_l(a_i + \Delta a_i - a_{i,j-1} - \Delta a_{i,j-1})^2]\}
\end{aligned}
\quad (4)
$$

where I_2' is the derivative of the I_2 in the axial direction. The optimal Δa_i values occur when the partial derivative of C_j with

respect to Δa_i is zero. Setting $(\partial C_j)/(\partial \Delta a_i) = 0$ for $i = 1 \ldots m$ we have

$$\left(\mathbf{I}_2'^2 + \alpha_a \mathbf{D} + \alpha_l \hat{\mathbf{I}}\right) \Delta \mathbf{a}_j = \mathbf{I}_2' \mathbf{e}$$
$$- (\alpha_a \mathbf{D} + \alpha_l \hat{\mathbf{I}}) \mathbf{a}_j + \alpha_l \mathbf{a}_{j-1}, \quad (5)$$

$$\mathbf{D} = \begin{bmatrix} 1 & -1 & 0 & 0 & \cdots & 0 \\ -1 & 2 & -1 & 0 & \cdots & 0 \\ 0 & -1 & 2 & -1 & \cdots & 0 \\ \vdots & & & & \ddots & \\ 0 & 0 & \cdots & 0 & -1 & 1 \end{bmatrix} \quad (6)$$

where $\mathbf{I}_2' = \mathrm{diag}(I_2'(1 + d_1, j + l_i) \ldots I_2'(m + d_m, j + l_i))$, $\Delta \mathbf{a}_j = [\Delta a_{1,j} \ldots \Delta a_{m,j}]^T$, $\mathbf{e} = [e_1 \ldots e_m]^T$, $e_i = I_1(i,j) - I_2(i + d_i, j + l_i)$, $\mathbf{a}_j = [a_{1,j} \ldots a_{m,j}]^T$, $\hat{\mathbf{I}}$ is the identity matrix and $\mathbf{a}_{j-1}$ is the total displacement of the previous line (i.e., when the displacement of the $j - 1$th line was being calculated, $\mathbf{a}_{j-1}$ was updated with $\mathbf{a}_{j-1} + \Delta \mathbf{a}_{j-1}$). $\mathbf{I}_2'$, $\mathbf{D}$ and $\hat{\mathbf{I}}$ are matrices of size m × m and $\Delta \mathbf{a}$, $\mathbf{e}$ and $\mathbf{a}$ are vectors of size m.

Comparing 1D AM [as formulated in (5)] and 2D DP, they both optimize the same cost function. Therefore, they give the same displacement fields (up to the refinement level of the DP). In the next two subsections, we will further improve 1D AM.

1) Biasing the Regularization: The regularization term $\alpha_a(a_i + \Delta a_i - a_{i-1} - \Delta a_{i-1})^2$ penalizes the difference between $a_i + \Delta a_i$ and $a_{i-1} + \Delta a_{i-1}$, and therefore can result in underestimation of the displacement field. Such underestimation can be prevented by biasing the regularization by ϵ to $\alpha_a(a_i + \Delta a_i - a_{i-1} - \Delta a_{i-1} - \epsilon)^2$, where $\epsilon = (a_m - a_1)/(m-1)$ is the average displacement difference (i.e., average strain) between samples i and $i-1$. An accurate enough estimate of $d_m - d_1$ is known from the previous line. With the bias term, the right-hand side of (5) becomes $\mathbf{I}_2' \mathbf{e} - (\alpha_a \mathbf{D} + \alpha_l \hat{\mathbf{I}}) \mathbf{a}_j + \alpha_l(\mathbf{a}_{j-1} + \Delta \mathbf{a}_{j-1}) + \mathbf{b}$ where the bias term is $\mathbf{b} = \alpha_a[-\epsilon \, 0 \ldots 0 \, \epsilon]^T$ (only the first and the last terms are nonzero) and all other terms are as before. In the other words, except for the first and the last equations in this system, all other $m - 2$ equations are same as (5).

Equation (5) can be solved for $\Delta \mathbf{a}_j$ in $4m$ operations since the coefficient matrix $\mathbf{I}_2'^2 + \alpha_a \mathbf{D} + \alpha_l \hat{\mathbf{I}}$ is tridiagonal. Utilizing its symmetry, the number of operations can be reduced to $2m$. The number of operations required for solving a system with a full coefficient matrix is more than $m^3/3$, significantly more than $2m$.

2) Making Elastography Resistant to Outliers: Even with pure axial compression, some regions of the image may move out of the imaging plane and decrease the decorrelation. In such parts the weight of the data term in the cost function should be reduced. The data from these parts can be regarded as outliers and therefore a robust estimation technique can limit their effect. Before deriving a robust estimator for $\Delta \mathbf{d}$, we rewrite (4) as

$$C(\Delta \mathbf{d}) = \sum_{i=1}^{m} \rho(r_i) + R(\Delta \mathbf{d}) \quad (7)$$

where $r_i = I_1(i) - I_2(i + d_i) - I_2'(i + d_i)\Delta d_i$ is the residual, $\rho(r_i) = r_i^2$ and R is the regularization term. The M-estimate of $\Delta \mathbf{d}$ is $\Delta \mathbf{d} = \arg\min_{\Delta \mathbf{d}}\{\sum_{i=1}^{m} \rho(r_i) + R(\Delta \mathbf{d})\}$ where $\rho(r_i)$

is a robust loss function [43]. The minimization is solved by setting $(\partial C)/(\partial \Delta d_i) = 0$

$$\rho'(r_i)\frac{\partial r}{\partial \Delta d_i} + \frac{\partial R(\Delta \mathbf{d})}{\partial \Delta d_i} = 0. \quad (8)$$

A common next step [44] is to introduce a weight function w, where $w(r_i).r_i = \rho'(r_i)$. This leads to a process known as "iteratively reweighted least squares" (IRLS) [45], which alternates steps of calculating weights $w(r_i)$ for $r_i = 1 \ldots m$ using the current estimate of $\Delta \mathbf{d}$ and solving (8) to estimate a new $\Delta \mathbf{d}$ with the weights fixed. Among many proposed shapes for $w(\cdot)$, we compared the performance of Huber [44], [43]

$$w(r_i) = \begin{cases} 1 & |r_i| < T \\ \frac{T}{|r_i|} & |r_i| > T \end{cases} \quad (9)$$

and Cauchy [45]

$$w(r_i) = \frac{1}{1 + (r_i/T)^2} \quad (10)$$

functions and discovered that the more strict Cauchy function (which decreases with inverse of the *square* of the residual) is more suitable in our application. To better discriminate outliers, we calculate the residuals r_i at linear interpolation of the integer sample displacements provided by DP. With the addition of the weight function, (8) becomes

$$\left(\mathbf{w}\mathbf{I}_2'^2 + \alpha_a \mathbf{D} + \alpha_l \hat{\mathbf{I}}\right) \Delta \mathbf{a}_j = \mathbf{w}\mathbf{I}_2'\mathbf{e}$$
$$- (\alpha_a \mathbf{D} + \alpha_l \hat{\mathbf{I}})\mathbf{a}_j + \alpha_l \mathbf{a}_{j-1} + \mathbf{b} \quad (11)$$

where $\mathbf{w} = \mathrm{diag}(w(r_1) \ldots w(r_m))$. This equation will converge to a unique local minimum after few iterations [45]. The convergence speed however depends on the choice of T, which in this work is defined manually. Since the Taylor approximation gives a local quadratic approximation of the original nonquadratic cost function, the effect of higher orders terms increase if Δa_j is large. Assuming that DP gives the correct displacements, $\|\Delta a_j\|_\infty \leq \epsilon$ where $\|\cdot\|_\infty$ is the infinity norm and $\epsilon \leq 0.5$. In practice, however, $\epsilon \ll 0.5$ because the linear interpolation of the DP displacements (which is very close to the correct displacement) is used to calculate the residuals r_i. Therefore, a small value can be assigned to T in 1D AM provided that DP results are trusted.

The coefficient matrix $Q = \mathbf{w}\mathbf{I}_2'^2 + \alpha_a \mathbf{D} + \alpha_l \hat{\mathbf{I}}$ in (11) is the Hessian of the cost function C whose minimum is sought. This matrix is strictly diagonally dominant (i.e., $|q_{ii}| > \sum_{j \neq i} |q_{ij}|$ for all i where q_{ij} is the i,jth element of Q), symmetric and all diagonal entries are positive. Therefore, it is positive definite, which means that setting the gradient of C to zero results in the global minimum of C (not in a saddle point, a local maximum or a local minimum). All of the 1D AM results presented in this work are obtained with one iteration of the above equation.

1D AM takes the integer axial and lateral displacement fields from DP and gives refined axial displacement. It inherits the robustness of DP and adds more robustness when calculating the fine axial displacements via IRLS. However, there are redundant calculations in this method which are eliminated in 2D AM as described next.

C. 2D Analytic Minimization (AM)

In 2D AM, we modify (2) to calculate subsample axial and lateral displacement fields *simultaneously*. The outline of our proposed algorithm is as follows.

1) Calculate the integer axial and lateral displacements of one or more seed RF-lines (preferably in the middle of the image) using DP [(2)]. Calculate the linear interpolation of the integer displacements as an initial subsample estimate.

2) Calculate subsample axial and lateral displacements of the *seed* RF-line using 2D AM, as explained below. Add the subsample axial and lateral displacements to the initial estimate to get the displacement of the seed line.

3) Propagate the solution to the right and left of the seed RF-line using the 2D AM method, taking the displacement of the previous line as the initial displacement estimate.

Benefits of 2D AM are two-fold. First it computes subsample displacements in both axial and lateral directions. Lateral strain contains important information from tissue structure that is not available from axial strain [31], [46], [47]. Second, it is only required to calculate the displacement of a single line using DP (the seed), eliminating the need to have the integer displacement map for the entire image. This is significant as in the 1D AM method, the initial step to calculate the 2D integer displacements using DP takes about **10** times more than the 1D AM.

Assume that initial displacement estimates in the axial direction, a_i, and in the lateral direction, l_i, are known for all $i = 1 \ldots m$ samples of an RF-line. Note that a_i and l_i are not integer; for the seed line they are the linear interpolation of the integer DP displacements and for the rest of the lines are the displacement of the previous line. It is desired to find Δa_i and Δl_i values such that the duple $(a_i + \Delta a_i, l_i + \Delta l_i)$ gives the axial and lateral displacements at the sample i. Such $(\Delta d_i, \Delta a_i)$ values will minimize the following regularized cost function:

$$C_j(\Delta a_1, \ldots, \Delta a_m, \Delta l_1, \ldots, \Delta l_m)$$
$$= \sum_{i=1}^{m} \{ [I_1(i,j) - I_2(i + a_i + \Delta a_i, j + l_i + \Delta l_i)]^2$$
$$+ \alpha(a_i + \Delta a_i - a_{i-1} - \Delta a_{i-1})^2$$
$$+ \beta_a(l_i + \Delta l_i - l_{i-1} - \Delta l_{i-1})^2$$
$$+ \beta_l'(l_i + \Delta l_i - l_{i,j-1})^2 \} \quad (12)$$

where $I(i,j)$ is the ith sample on the jth RF-line. Since we perform the calculations for one RF-line at a time, we dropped the index j to simplify the notations: $a_i, l_i, \Delta a_i,$ and Δl_i are $a_{i,j}, l_{i,j}, \Delta a_{i,j},$ and $\Delta l_{i,j}$. $l_{i,j-1}$ is the lateral displacement of the previous RF-line (note that $l_{i,j-1}$ is the total lateral displacement of the previous line, i.e., when the displacement of the $j - 1$th line was being calculated, $l_{i,j-1}$ was updated with $l_{i,j-1} + \Delta l_{i,j-1}$). Since in the first iteration a_i and l_i (the initial displacement estimates) are in fact the displacements of the previous RF-line, for the first iteration we have $l_{i,j-1} = l_i$. This simplifies the last term in the right-hand side to $\beta_l' \Delta l_i^2$. The regularization terms are α, β_a and β_l': α determines how close the axial displacement of each sample should be to its neighbor on the top and β_a and β_l' determine how close lateral displacement of each sample should be to its neighbors on the top and left

(or right if propagating to the left). If the displacement of the previous line is not accurate, it will affect the displacement of the next line through the last term in the right-hand side of (12). Although its effect will decrease exponentially with j, it will propagate for few RF-lines. Therefore, we set

$$\beta_l' = \frac{\beta_l}{1 + |r_{i,j-1}|} \quad (13)$$

to prevent such propagation where $r_{i,j-1}$ is the residual associated with the displacement of the ith sample of the previous line. A large residual indicates that the displacement is not accurate and therefore its influence on the next line should be small, which is realized via the small weight β_l'. This is, in principle, similar to guiding the displacement estimation based on a data quality indicator [48]. The effect of the tunable parameters α, β_a and β_l is studied in Section III. Writing the 2D Taylor expansion of the data term in (12) around $(i + a_i, j + l_i)$

$$I_2(i + a_i + \Delta a_i, j + l_i + \Delta l_i)$$
$$\approx I_2(i + a_i, j + l_i) + \Delta a_i I_{2,a}' + \Delta l_i I_{2,l}' \quad (14)$$

where $I_{2,a}'$ and $I_{2,l}'$ are the derivatives of the I_2 at point $(i + a_i, j + l_i)$ in the axial and lateral directions respectively. Note that since the point $(i + a_i, j + l_i)$ is not on the grid (a_i and l_i are not integer), interpolation is required to calculate $I_{2,a}'$ and $I_{2,l}'$. We propose a method in Section II-C1 that eliminates the need for interpolation. The optimal $(\Delta a_i, \Delta l_i)$ values occur when the partial derivatives of C_j with respect to both Δa_i and Δl_i are zero. Setting $(\partial C_j)/(\partial \Delta a_i) = 0$ and $(\partial C_j)/(\partial \Delta l_i) = 0$ for $i = 1 \ldots m$ and stacking the $2m$ unknowns in $\Delta \mathbf{d} = [\Delta a_1 \, l_1 \, \Delta a_2 \, \Delta l_2 \ldots \Delta a_m \, \Delta l_m]^T$ and the $2m$ initial estimates in $\mathbf{d} = [a_1 \, l_1 \, a_2 \, l_2 \ldots a_m \, l_m]^T$ we have

$$\left(\mathcal{I}_2'^2 + \mathcal{D}_1 + \mathcal{D}_2 \right) \Delta \mathbf{d} = \mathcal{I}_2' e - \mathcal{D}_1 \mathbf{d}, \quad (15)$$

$$\mathcal{D}_1 = \begin{bmatrix} \alpha & 0 & -\alpha & 0 & 0 & 0 & \cdots & 0 \\ 0 & \beta_a & 0 & -\beta_a & 0 & 0 & \cdots & 0 \\ -\alpha & 0 & 2\alpha & 0 & -\alpha & 0 & \cdots & 0 \\ 0 & -\beta_a & 0 & 2\beta_a & 0 & -\beta_a & \cdots & 0 \\ 0 & 0 & -\alpha & 0 & 2\alpha & 0 & \cdots & 0 \\ \vdots & & & & & & \ddots & \\ 0 & 0 & 0 & \cdots & -\alpha & 0 & \alpha & 0 \\ 0 & 0 & 0 & \cdots & 0 & -\beta_a & 0 & \beta_a \end{bmatrix}$$

where $\mathcal{D}_2 = \text{diag}(0, \beta_l', 0, \beta_l', \ldots, 0, \beta_l')$ is a diagonal matrix of size $2m \times 2m$, $\mathcal{I}_2'^2 = \text{diag}(\mathcal{J}'^2(1) \ldots \mathcal{J}'^2(m))$ is a symmetric tridiagonal matrix of size $2m \times 2m$ with

$$\mathcal{J}'^2(i) = \begin{bmatrix} I_{2,a}'^2 & I_{2,a}' I_{2,l}' \\ I_{2,a}' I_{2,l}' & I_{2,l}'^2 \end{bmatrix} \quad (16)$$

blocks on its diagonal entries where $I_{2,a}'$ and $I_{2,l}'$ are the derivatives of the I_2 at point $(i + a_i, j + l_i)$ in the axial and lateral directions

$$\mathcal{I}_2' = \text{diag}(I_{2,a}'(1), I_{2,l}'(1), I_{2,a}'(2), I_{2,l}'(2) \ldots$$
$$I_{2,a}'(m), I_{2,l}'(m)) \quad (17)$$

where $I'_{2,a}(i)$ and $I_{2,l}(i)'$ are calculated at point $(i+a_i, j+l_i)$, and $\mathbf{e} = [e_1\ e_1\ e_2\ e_2\ldots e_m]^T$, $e_i = I_1(i,j) - I_2(i+a_i, j+l_i)$.

We make four modifications to (15). First, we take into account the attenuation of the ultrasound signal with depth. As the signal gets weaker with depth, the first term in the right-hand side of (15) $(\mathcal{I}_2'\mathbf{e})$ gets smaller. This results in increasing the share of the regularization term in the cost C_j and therefore over-smoothing the bottom of the image. The attenuation of the ultrasound signal [49] reflected from the depth d is $\zeta(d) = e^{-2\log(10)a_t f_0 d/20}$ where a_t is the frequency dependent attenuation coefficient of tissue and is equal to 0.63 dB/cm/MHz for fat [49], f_0 is the center frequency of the wave (in MHz) and d is in cm. Having the exponential attenuation equation, the attenuation level at sample i will be

$$\zeta_i = x^{-i},\ x = e^{\frac{1540\times 10^2 a_t f_0 \log(10)}{20 f_s \times 10^6}},\ i = 1\ldots m \qquad (18)$$

where 1540×10^2 is the speed of sound in tissue (in cm/sec) and f_s is the sampling rate of the ultrasound system (in MHz). This is assuming that the TGC (time gain control) is turned off. Otherwise, the TGC values should be taken into account in this equation. Let the $2m \times 2m$ diagonal matrix $\mathbf{Z}$ be $\mathbf{Z} = \mathrm{diag}(\zeta_1, \zeta_1, \zeta_2, \zeta_2 \ldots \zeta_m, \zeta_m)$. To compensate for the attenuation, we multiply the $\mathcal{D}_1$ and $\mathcal{D}_2$ matrices in (15) by $\mathbf{Z}$, and therefore reduce the regularization weight with depth. As we will show in Sections III and IV, the regularization weight can vary substantially with no performance degradation. Therefore approximate values of the speed of sound and attenuation coefficient will suffice. Second, we add a bias term in the regularization similar to the 1D case. Here we only bias the axial displacement since the difference between the lateral displacements of the points on a RF-line is very small, usually less than 4 RF-lines. Third, we exploit the fact that, because the tissue is in contact with the ultrasound probe, the axial displacement of the top of the image is zero relative to the probe (the lateral displacement of the top of the image is not zero as tissue might slip under the probe). Therefore, we enforce the axial displacement of the first sample to be zero by changing the first row of $\mathcal{D}_1$, $\mathcal{I}_2'^2$, and $\mathcal{I}_2'$. Fourth, we make the displacement estimation robust via IRLS using the Cauchy function (10). Similar to 1D AM, T is selected manually. For the first (seed) RF-line, a small value can be selected for T if DP results are trusted. For the next lines, the value of $\Delta\mathbf{d}$ determines the accuracy of the Taylor expansion 14: for a small $\Delta\mathbf{d}$, the residuals of the inliers are small and therefore a small T can be chosen, while for a large $\Delta\mathbf{d}$ the inliers might give large residuals and therefore a large value for T is required. Since the tissue motion is mostly continuous, $\Delta\mathbf{d}$ mostly depends on the lateral sampling of the image (i.e., the number of A-line per cm). Therefore if many A-lines are given per cm of the image width, a small value of T will give the optimum results. Since the amplitude of signal is decreasing due to attenuation, we decrease the IRLS parameter T with depth by multiplying it with ζ_i at each sample i. With these modifications, (15) becomes

$$(\mathcal{W}\mathcal{I}_2'^2 + \mathbf{Z}\mathcal{D}_1 + \mathbf{Z}\mathcal{D}_2)\Delta\mathbf{d} = \mathcal{W}\mathcal{I}_2'\mathbf{e} - \mathbf{Z}\mathcal{D}_1\mathbf{d} + \mathbf{s} \qquad (19)$$

where $\mathcal{W} = \mathrm{diag}(0, w(r_1), w(r_2), w(r_2)\ldots w(r_m), w(r_m))$ (i.e., $\mathcal{W}_{2i,2i} = \mathcal{W}_{2i-1,2i-1} = w(r_i)$ for $i = 1\ldots m$ except for

$\mathcal{W}_{1,1} = 0$ which guarantees the displacement of the first sample to be zero) is the weight function determined by the residuals $r_i = I_1(i,j) - [I_2(i+d_i, j+a_i) + \Delta d_i I'_{2,z} + \Delta a_i I'_{2,x}]$, w is as before (10), the bias term $\mathbf{s}$ is a vector of length $2m$ whose all elements are zero except the $2m-1$th element: $s_{2m-1} = \alpha\epsilon$, and $\epsilon = (d_m - d_1)/(m-1)$ is as before. Similar to (11), the coefficient matrix $\mathcal{Q} = \mathcal{W}\mathcal{I}_2'^2 + \mathbf{Z}\mathcal{D}_1 + \mathbf{Z}\mathcal{D}_2$ is strictly diagonally dominant, symmetric and all the diagonal entries are positive. Therefore $\mathcal{Q}$ is positive definite which means that solving (19) results in the global minimum of the cost function C. The updated displacement field (axial and lateral) will be $d + \Delta d$.

Equation (19) can be solved for $\Delta\mathbf{d}$ in 9 m operations since the coefficient matrix $\mathcal{W}\mathcal{I}_2'^2 + \mathbf{Z}\mathcal{D}_1 + \mathbf{Z}\mathcal{D}_2$ is pentadiagonal and symmetric. This number is again significantly less than $((2m)^3)/(3)$, the number of operations required to solve a full system.

1) Inverse Gradient Estimation: With the subsample initial displacement field, the Taylor expansion should be written around off-grid points, which requires calculation of image gradient at these points [matrices $\mathcal{I}_2'^2$ and $\mathcal{I}_2'$ in (19)]. In Fig. 2(a), this is equivalent to calculating gradient of I_2 on the off-grid marks. There are two disadvantages associated with this: 1) it requires interpolation of the gradients, and 2) the image gradient should be recalculated after each iteration. As proposed by [44], [50], image gradient can be instead calculated at on-grid locations on image 1 in the following way.

Consider two problems: 1) to find the matches for grid points on I_1 having the initial off-grid estimates on I_2, and 2) to find the matches for the off-grid points on I_2 having the initial grid estimates on I_1. For both problems, I_2 values must be interpolated on the off-grid values. However, the second problem does not require interpolation of the image gradient since the Taylor expansion is written around grid points of I_1 [Fig. 2(b)]. It is shown in [51] that the two techniques converge to the same results. Therefore, on one hand inverse gradient calculation is both faster and easier to implement, and on the other hand it causes no performance degradation. Exploiting this, (19) becomes

$$\left(\mathcal{W}\mathcal{I}_1'^2 + \mathbf{Z}\mathcal{D}_1 + \mathbf{Z}\mathcal{D}_2\right)\Delta\mathbf{d} = \mathcal{W}\mathcal{I}_1'\mathbf{e} - \mathbf{Z}\mathcal{D}_1\mathbf{d} + \mathbf{s} \qquad (20)$$

where $\mathcal{I}_1'^2$ and $\mathcal{I}_1'$ are now calculated on the grid points of image 1.

All the 2D AM results presented in this work are obtained using (20). For the seed line where the initial estimate might be inaccurate, this equation is iterated multiple times (about 10 times). For all other lines, this equation is iterated only once.

D. Strain Estimation Using Kalman Filter

Strain estimation requires spatial derivation of the displacement field. Since differentiation amplifies the signal noise, least squares regression techniques are commonly used to obtain the strain field. Adjacent RF-lines are usually processed independently in strain calculation. However, the strain value of each pixel is not independent from the strain value of its neighboring pixels. The only exception is the boundary of two tissue types with different mechanical properties where the strain field is discontinuous. We use the prior of piecewise strain continuity via
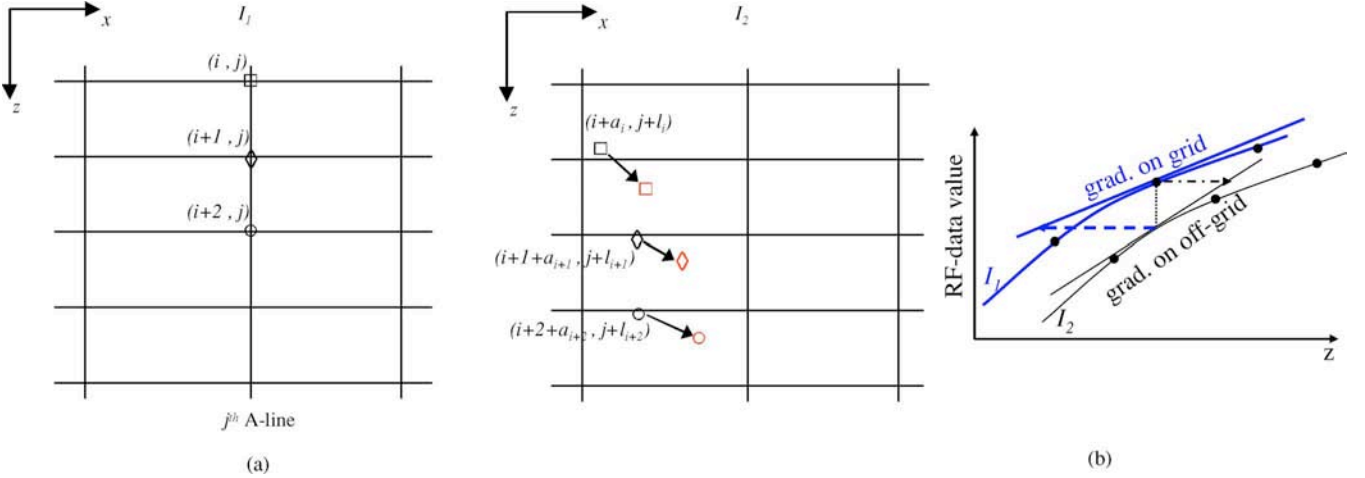
Fig. 2. (a) In I_2 the initial estimates (in black) are updated by the arrows (three components of $\Delta \mathbf{d}$) to new estimates (in red) after an iteration of 2D AM. To find $\Delta \mathbf{d}$ using (19), it is required to calculate image gradient at the off-grid initial estimate locations (in black) on I_2. (b) Schematic plot of two RF-data I_1 and I_2, each sampled at three locations (black dots). The black dashed–dotted arrow shows Δa of the sample on I_1 (ignoring the regularization term) which requires calculating the gradient on I_2 at an off-grid location. The blue dashed arrow shows Δa of an off-grid sample on I_2 (ignoring the regularization term) which requires calculating the gradient on I_1 at an on-grid location. Ignoring second-order derivatives, the length of the two arrows is equal. (a) Three samples on I_1 (left) and corresponding matches on I_2 (right). (b) Inverse gradient estimation.

a Kalman filter to improve the quality of strain estimation. Although locations with strain discontinuity are limited, we will develop a technique to take such discontinuities into account.

We first calculate the strain using least squares regression. Each RF-line is first differentiated independently: for each sample i, a line is fitted to the displacement estimates in a window of length $2k + 1$ around i, i.e., to the samples $i - k$ to $i + k$. The slope of the line, $z_{i,j}$, is calculated as the strain measurement at i. The center of the window is then moved to $i + 1$ and the strain value $z_{i+1,j}$ is calculated. We reuse overlapping terms in calculation of $z_{i,j}$ and $z_{i+1,j}$, and therefore the running time is independent of the window length $2k + 1$. Having $z_{i,j}$ for $i = 1 \ldots m$ and $j = 1 \ldots n$, we propose the following algorithm based on Kalman filter to take into account the prior of strain continuity.

$z_{i,j}$ are the noisy measurements of the underlying strain field $\epsilon_{i,j}$. Since the $z_{i,j}$ values are calculated using axial windows, we apply the Kalman filter in the lateral direction. Let r_j be the Gaussian process noise and s_j be the Gaussian measurement noise to be removed. We have [52], [41]

$$\epsilon_{i,j} = \epsilon_{i,j-1} + r_{i,j} \qquad (21)$$
$$z_{i,j} = \epsilon_{i,j} + s_{i,j}. \qquad (22)$$

Let $\hat{\epsilon}_{i,j}^-$ (note the super minus) be our *a priori* strain estimate from the process prior to step j [i.e., from the (21)] and $\hat{\epsilon}_{i,j}$ be our *a posteriori* strain estimate at step j given measurement z_j. Let also the variances of $\hat{\epsilon}_{i,j}^-$ and $\hat{\epsilon}_{i,j}$ be respectively p^- and p. The time update (i.e., prior estimation) equations will be [41]

$$\hat{\epsilon}_{i,j}^- = \hat{\epsilon}_{i,j-1} \qquad (23)$$
$$p_{i,j}^- = p_{i,j-1} + \sigma_r^2 \qquad (24)$$

where σ_r^2 is the variance of the process noise r. $p_{i,j-1}$ is initialized to zero for the first sample $j = 1$. The measurement update equations will be [41]

$$\hat{\epsilon}_{i,j} = \hat{\epsilon}_{i,j}^- + \frac{p_{i,j}^-}{p_{i,j}^- + \sigma_s^2}(z_{i,j} - \hat{\epsilon}_{i,j}^-) \qquad (25)$$
$$p_{i,j} = \left(1 - \frac{p_{i,j}^-}{p_{i,j}^- + \sigma_s^2}\right) p_{i,j}^- \qquad (26)$$

where σ_s^2 is the variance of the measurement noise s. Note that since both the state $\epsilon_{i,j}$ and measurement $z_{i,j}$ are scalars, all the update equations only require scalar operations. We estimate σ_r^2 and σ_s^2 as following. Let the mean (calculated using a Gaussian kernel of standard deviation of $\sigma_G = 0.6$ sample) of the strain values in 3×3 blocks around samples $(i, j - 1)$ and (i, j) be μ_{j-1} and μ_j, respectively. Then σ_r^2 is [52]

$$\sigma_r^2 = (\mu_{j-1} - \mu_j)^2. \qquad (27)$$

This is a reasonable estimate of σ_r^2 as it tries to capture the difference between pixel values at adjacent RF-lines. If the difference between the mean strain values is high, less weight is given to the *a priori* estimate. This space-variant estimation of the model noise provides a better match to local variations in the underlying tissue leading to a greater noise reduction. σ_s^2 is the variance of $z_{i,j}$ measurements in the entire image and is constant throughout the image.

The strain estimation algorithm can be summarized as following.

1) Perform least squares regression in the *axial* direction for each RF-line. Generate a (noisy) strain image Z whose pixel i, j is $z_{i,j}$. This step ensures continuity in the axial direction.

2) Apply the Kalman filter to the noisy strain image Z in the *lateral* direction. Generate a (denoised) strain image whose

pixel i, j is $\hat{\epsilon}_{i,j}$. This step ensures continuity in the lateral direction.

Both steps are applied once and are not iterated. We show in the experimental results how the Kalman filter removes the noise from the strain image with minimal blurring, owing to the model noise update (27).

III. SIMULATION RESULTS

Field II [53] and ABAQUS (Providence, RI) software are used for ultrasound simulation and for finite element simulation. Many scatterers are distributed in a volume and an ultrasound image is created by convolving all scatterers with the point spread function of the ultrasound and adding the results using superposition. The phantom is then meshed and compressed using finite element simulation, giving the 3D displacement of each node of the mesh. The displacement of each scatterer is then calculated by interpolating the displacement of its neighboring nodes. Scatterers are then moved accordingly and the second ultrasound image is generated. The displacement and strain fields are then calculated using the AM methods and are compared with the ground truth. The unitless metric signal-to-noise ratio (SNR) and contrast to noise ratio (CNR) are also calculated to assess the performance of the AM method according to

$$\text{CNR} = \frac{C}{N} = \sqrt{\frac{2(\bar{s}_b - \bar{s}_t)^2}{\sigma_b^2 + \sigma_t^2}}, \quad \text{SNR} = \frac{\bar{s}}{\sigma} \qquad (28)$$

where $\bar{s}_t$ and $\bar{s}_b$ are the spatial strain average of the target and background, σ_t^2 and σ_b^2 are the spatial strain variance of the target and background, and $\bar{s}$ and σ are the spatial average and variance of a window in the strain image, respectively.

The parameters of the ultrasound probe are set to mimic commercial probes. The probe frequency is 7.27 MHz, the sampling rate is 40 MHz and the fractional bandwidth is 60%. A Hanning window is used for apodization, the single transmit focus is at 22.5 mm, equi-distance receive foci are from 5 to 45 mm at each 5 mm, the transmit is sequential, and the number of active elements is 64.

Two simulated phantoms are generated. The first phantom is $50 \times 10 \times 55$ mm and the second one is $36 \times 10 \times 25$ mm. Respectively 5×10^5 and 1.4×10^5 scatterers with Gaussian scattering strengths [54] are uniformly distributed in the first and second phantom, ensuring more than 10 scatterers [55] exist in a resolution cell.

The mechanical properties of both phantoms, required for finite element simulation, is assumed to be isotropic and homogeneous. The first phantom is uniform while the second phantom contains a circular hole filled with blood that can move out-of-plane, simulating a blood vessel in tissue [Fig. 7(a)]. The scatterers are distributed in the vessel, also with the same intensity and distribution as the surrounding material. A uniform compression in the z direction is applied and the 3D displacement field of phantoms is calculated using ABAQUS. The Poisson's ratio is set to $\nu = 0.49$ in both phantoms to mimic real tissue [56], [57] which causes the phantoms to deform in x and y directions as a result of the compression in the z direction.

The first phantom undergoes compressions in the z direction to achieve strain levels of 1%–10%. Fig. 3 shows the SNR of the axial strain of the 1D AM and 2D AM methods [the window for SNR calculation covers the entire strain image in (a) and (f)]. The sharp drop of the SNR with strain in graph (a) is mainly due to the strain underestimation in the bottom part of the image. It can be explained as following. The unbiased regularization term tries to force constant displacement [dashed–dotted red line in (b)]. Assuming an ideal noiseless case where the data term gives a smooth ramp displacement [dashed black line in (b)], minimizing the cost function (which is the summation of the data and the regularization terms) will underestimate the displacement at the two ends [solid blue line in (b)]. This underestimation decays exponentially moving towards the center of the image. This artifact is shown in the simulation experiment at 2% and 6% strain levels in (c) and (d). Since we exploit the fact that the axial displacement of the first sample is zero (Section II-C), the underestimation does not happen in the top of the image. Biasing the regularization prevents this artifact, as is shown in (c) and (d). The AM method with or without the bias term gives the same result away from the bottom of the image: part (e) shows that if we ignore 300 (5.8 mm) samples at the bottom of the image, the SNR will not drop sharply unlike in part (a). Part (f) shows the SNR of the AM methods with biased regularization calculated in the entire image. The SNR at 1% strain in parts (e) and (f) is the same. At higher strain levels, the strain underestimation propagates more into the middle of the image, and therefore the SNR decreases at higher strain levels in graph (e). Part (e) shows 2D AM gives slightly better axial strain compared to 1D AM. IRLS slightly increases the SNR. However, we will see in the simulation results of the second phantom that in the presence of outliers significant improvement in SNR and CNR is achieved using IRLS.

The SNR of the lateral strain field is much lower than that of the axial strain field (Fig. 4). Unbiased regularization gives the lowest SNR, mainly due to artifacts in the bottom of the image. Similar to the axial strain, the SNR improves as 300 samples from the bottom of image are omitted from the SNR calculation (results not shown).

The effect of the regularization weights on bias and variance of the axial strain image at 2% ground truth axial strain is shown in Fig. 5. The blue curves show the bias and variance of the entire strain image obtained with unbiased regularization. It shows the tradeoff between the bias and variance: increasing the regularization weight increases the bias and decreases the variance. The variance starts to increase at $\alpha \approx 12$ which is caused by the underestimation of the strain at the bottom of the image [the artifact in Fig. 3(c)]. If we exclude the bottom 300 samples of the strain image from the bias and variance calculation (the black dashed curve), we see a consistent drop of variance as α is increased. The black curves show the bias and variance of the entire strain image obtained with biased regularization. Biasing the regularization causes the bias to decrease as the regularization weight α is increased which is a nonstandard behavior. It can be explained by the simple ground truth strain field which is uniform, exactly what the regularization term is trying to achieve. Even in the unbiased case, only the bias of the bottom part of the strain field increases as α is increased (i.e., in the bias plot, the
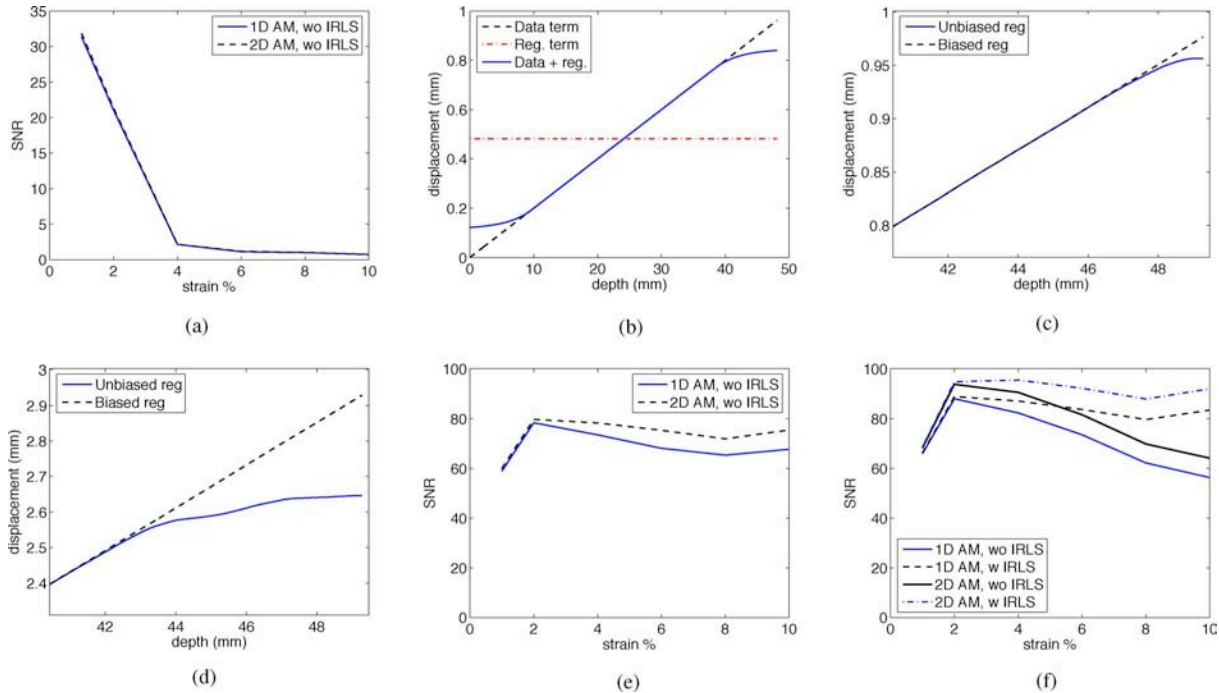
Fig. 3. Axial strain estimation in the first simulated phantom. (a) The SNR values corresponding to the unbiased regularization calculated in the entire image. (b) Schematic plot showing the underestimation of the displacement (Data + reg. curve) with unbiased regularization (refer to the text). (c), (d) The calculated displacements at the bottom of a RF-line at 2% strain and 6% strain levels respectively with biased and unbiased regularization terms. *The ground truth matches the displacement given by the biased regularization almost perfectly, and therefore is not shown in (c) and (d) not to block the biased regularization results.* The length of the RF-line is 2560 (49.3 mm). (e) The SNR values corresponding to the unbiased regularization calculated by omitting the bottom 300 samples of the image. (f) The SNR values corresponding to the biased regularization calculated in the entire image. Note that the scale of the SNR in graph (a) is much smaller than that of graphs (e) and (f). (a) Unbiased reg. Entire image. (b) Schematic displacements. (c) Calculated displacements at 2% strain. (d) Calculated displacements at 6% strain. (e) Unbiased reg. Top of the image. (f) Biased reg. Entire image.
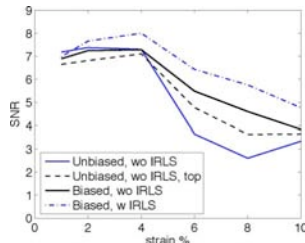

Fig. 4. Lateral strain estimation using the 2D AM method in the first simulated phantom.

Fig. 5. Bias and Variance of the axial strain as a function of the axial regularization weight α. The ground truth axial and lateral strain fields are respectively uniform 2% and 2ν% fields ($\nu = 0.49$ is the Poisson's ratio). The solid blue and dashed black curves both correspond to unbiased regularization and the solid black curve corresponds to the biased regularization. In the solid blue and solid black curves, the entire image is included in the calculation of the bias and noise. In the dashed black curve the bottom part of the strain field which suffers from high bias [Fig. 3(b)] is excluded from the calculation of the bias and noise. 1D AM and 2D AM have very similar bias and variance. The curves with and without IRLS are also very close. Therefore each curve corresponds to 1D AM or 2D AM with or without IRLS. (a) Bias. (b) Variance.

blue curve increases while the black dashed curve decreases). Therefore, one cannot conclude from this experiment that higher α is beneficial to both bias and variance. To prove this, we designed a simulation study where the underlying axial strain field continuously varied with depth and the lateral and out-of-plane strains were zero (such strain field is not physically realizable). We observed that the absolute value of the bias monotonically increases with α with both unbiased and biased regularizations. To save space, we do not present the full results here. Similar curves for the lateral strain field is shown in Fig. 6.

The second simulation experiment is designed to show the effect of smoothness weight and IRLS threshold CNR when the correlation is lower in parts of the image due to fluid motion. The phantom contains a vein oriented perpendicular to the image plane (Fig. 7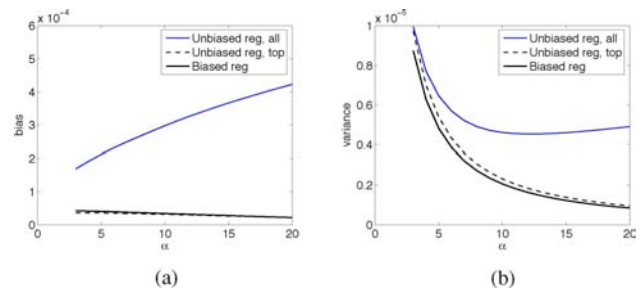). The background window for CNR calculation is located close to the target window to show how fast the strain is allowed to vary, a property related to the spatial resolution. The maximum CNR with IRLS is 5.3 generated at $T = 0.005$ and $\alpha_a = 38$, and without IRLS is 4.8 at $\alpha_a = 338$. Such high α_a value makes the share of the data term in the cost function very small and causes over-smoothing.
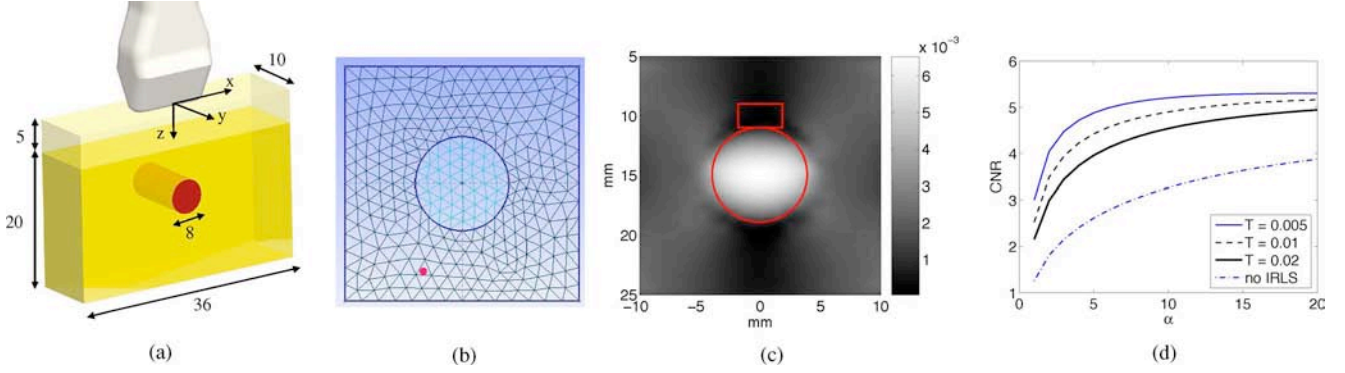
Fig. 6.   Bias and Variance of the lateral strain as a function of the axial regularization weight α. The ground truth axial and lateral strain fields are respectively uniform 2% and 2ν% fields ($\nu = 0.49$ is the Poisson's ratio). The solid blue curve corresponds to unbiased regularization and the dashed and solid black curves correspond to the biased regularization. IRLS is not used in the solid blue and dashed black curves. (a) Bias. (b) Variance.
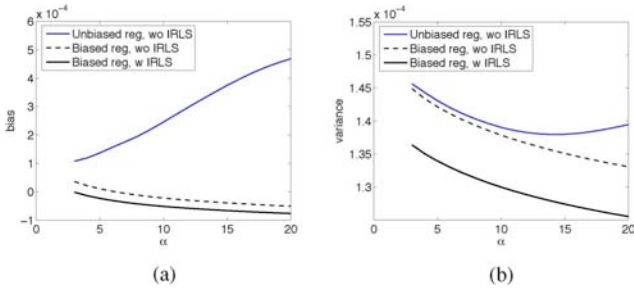

Fig. 7.   Measurements in (a) are in mm. In (b), a scatterer is shown in the bottom left part as a red dot. Its displacement is calculated by interpolating the displacements of its three neighboring nodes on the mesh. The target (circular) and background (rectangular) windows for CNR calculation of (d) are shown in (c). (a) Simulation phantom. (b) Finite element mesh. (c) Finite element strain. (d) CNR.

A. Displacement Simulation

To study the performance of the Kalman filter, we simulate a displacement field of size 100×100 samples whose strain image (calculated using least squares regression) is as shown in Fig. 8(a). One hundred samples in the axial direction corresponds to approximately 1.9 mm (assuming 40 MHz sampling rate), and 100 samples in the lateral direction corresponds to 10–25 mm depending on the probe. To be consistent with the notations of Section II-D, let $\epsilon_{i,j}$ denote the strain values of the uncontaminated image in (a). We then contaminate the displacement field with a Gaussian noise with standard deviation of 1.5 samples, and perform least squares regression to calculate the noisy estimates $z_{i,j}$ [Fig. 8(b)]. We then apply the Kalman filter as described in Section II-D to the noisy estimates $z_{i,j}$ in the lateral direction (i.e., row-by-row). The posterior estimates of the strain values, $\hat{\epsilon}_{i,j}$ are shown in (c). The strain values of the shown line in (a)–(c) (at $i = 50$ samples) is shown in (d) and (e) [The plot in (d) around the step in magnified in (e)]. The Kalman filter formulation is eliminating the noise without over-smoothing the strain image. This is due to the model variance update (27). We note that although displacement is generally continuous in tissue, its spatial derivation (strain) is not: at the boundary of two tissues with different elasticity moduli, strain field is discontinuous.

IV. EXPERIMENTAL RESULTS

For experimental evaluation, RF data is acquired from an Antares Siemens system (Issaquah, WA) at the center frequency of 6.67 MHz with a VF10-5 linear array at a sampling rate of 40 MHz. Only the 2D AM method is used in the experimental results. Phantom results and patient trials are presented in this section. The tunable parameters of the 2D AM algorithm are set to $\alpha = 5$, $\beta_a = 10$, $\beta_l = 0.005$ and $T = 0.2$ [(12) and (20)], and the tunable parameters of the DP (run for the seed RF-line in the 2D AM algorithm) are $\alpha_a = \alpha_l = 0.15$ (1) in all the phantom results (except if specified otherwise). In the patient results, all the parameters are the same except for β_a which is increased to $\beta_a = 20$ because the data is noisier. The strain images in all the patient trials are obtained using the least squares regression and Kalman filtering as described in Section II-D.

A. Phantom Results

1) Effect of Regularization on Residuals: The cost function of the AM method (7) is composed of residuals (i.e., the data term) and the regularization terms. The AM method minimizes this summation. Therefore the AM method will not necessarily minimize the residuals. We now show that the data term alone is nonconvex and has many local minima. Adding the regularization term will eliminate many of the local minima and makes optimization of the data term easier. This is in addition to the effect of regularization that makes the displacement field smooth, a generally desired attribute.

The effect of regularization on the residuals is studied using experimental data. An elastography phantom (CIRS elastography phantom, Norfolk, VA) is compressed 0.2 in axially using a linear stage, resulting in an average strain of 6%. Two RF frames are acquired corresponding to before and after the compression. The Young's elasticity modulus of the background and the lesion under compression are respectively 33 kPa and 56 kPa. The displacement map is calculated using the 2D AM method and the residuals corresponding to the displacement map are obtained. Fig. 9(a)–(c) shows the axial and lateral strains at such a high strain rate (minimum of 2% and maximum of 11%). The mean and median of the residuals $\rho(r_i)$ in the entire image is shown in (d). One could expect the graph to monotonically increase as the regularization weight α
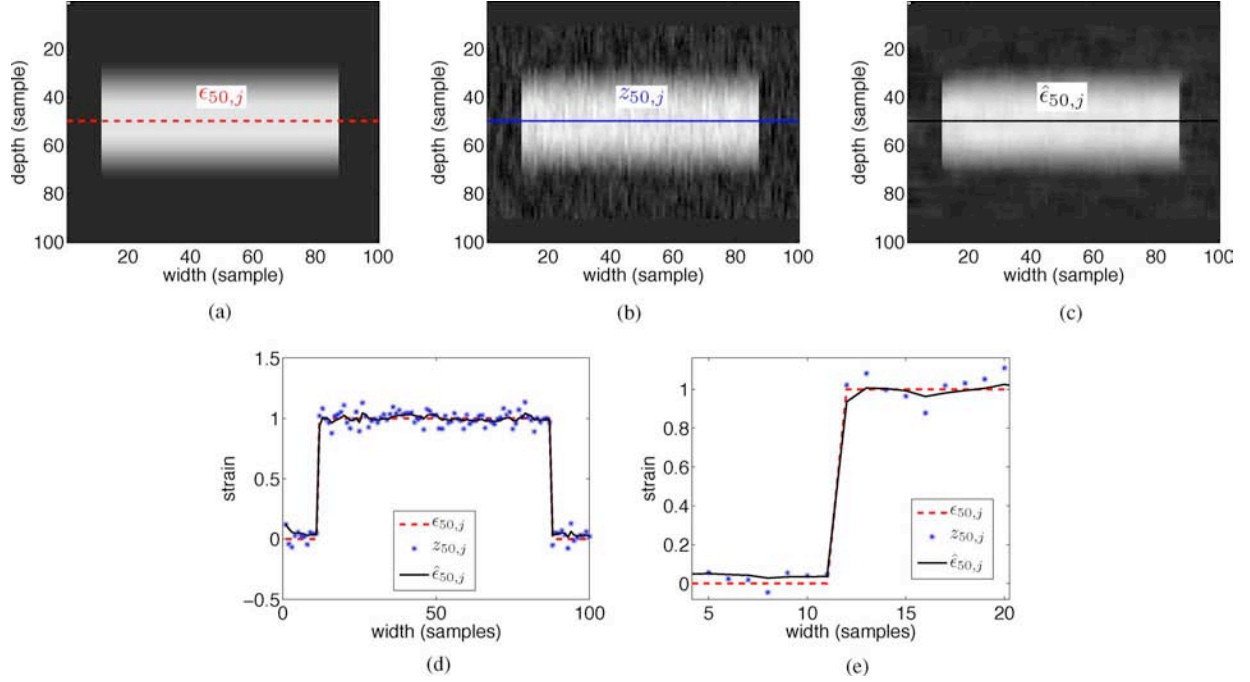
Fig. 8. (a) shows the strain field calculated using least squares regression of the uncontaminated displacement field. (b) depicts the strain field calculated using least squares regression of the contaminated displacement field. (c) shows the strain field calculated from the noisy measurements of (b) using the proposed Kalman filter (KF in (b) and (c) refers to Kalman filter). The pixels of images in (a) to (c) are respectively the ground truth (unavailable) strain values $\epsilon_{i,j}$, the noisy measurements $z_{i,j}$, and posterior strain values $\hat{\epsilon}_{i,j}$. The brightness scale in (a)–(c) is the same. (d), (e) are the strain estimation at the horizontal line shown in (a)–(c). (d) is magnified in (e) around the step. The Kalman filter removes the noise while keeping the image sharp, due to the variable model noise of (27). (a) Ground truth strain. (b) Strain without KF. (c) Strain with KF. (d) Strain estimate. (e) Strain estimates.

increases, since the difference between the objective function C and the residuals $\sum_{i=1}^{m} \rho(r_i)$ is increased as α is increased. However, the residual values are very high at very low α. Therefore, numerical minimization of $\sum_{i=1}^{m} \rho(r_i) + R(\Delta \mathbf{d})$ gives a smaller value for $\sum_{i=1}^{m} \rho(r_i)$ compared to trying to directly minimize $\sum_{i=1}^{m} \rho(r_i)$. This indicates that the nonregularized cost function is not quasi-convex and is very hard to minimize.

2) Resolution of the Strain Images Generated With AM: The effect of the regularization on spatial resolution is evaluated experimentally using the experimental setup of the previous experiment. The compression is set to 0.1 in in this experiment. Fig. 10(a) shows the strain image obtained by compression the lesion with the Young's modulus of 56 kPa. Spatial resolution is evaluated using modulation transfer function (MTF), an established method for estimating the spatial resolution of medical imaging systems that was relatively recently extended to elastography [58]. The spatial resolution of the reconstructed images is determined with a three-step approach [59], [60]. First, the edge spread function is computed by averaging the pixel values across the background-inclusion interface [the line in Fig. 10(a)]. Second, the line spread function (LSF) is computed by differentiating the edge spread function. Third, the MTF is determined by computing the Fourier transform of the LSF and normalizing the resulting function to zero spatial frequency

$$\text{MTF}(k) = \frac{\Xi(k)}{\Xi(0)}. \quad (29)$$

Fig. 10(c) shows the MTF for five different normalization coefficients respectively. Strain results are obtained with a regression window of length $2k + 1 = 65$ [Section II-D]. Increasing the

regularization weight is adversely affecting spatial resolution. Spatial resolution is defined as the spatial frequency when the value of MTF is 0.1. At $\alpha = 1$, $\alpha = 2$ and $\alpha = 4$ this value is respectively 2 cycles/mm, 1 cycles/mm, and 0.5 cycles/mm. In addition to α, this value also depends on the length of the regression window $2k + 1$.

3) Image Quality Versus Axial and Lateral Sampling Rates of the RF-Data: Sampling rate of the RF-data usually ranges from 20 to 50 MHz depending on the hardware of the device. The number of the A-lines provided in an image also varies significantly. In addition, bandwidth limitations of the data transfer can impose limits on the size of the image for real-time operations. In this study, we downsample the RF-data by a factor of 2–4 in the axial direction and by a factor of 2–8 in the lateral direction. Fig. 11(a)–(g) shows axial and lateral displacement and strain images of the CIRS elastography phantom undergoing maximum axial strain of 5%. Axial sampling rate can be reduced by a factor of 2 without significant impact on the strain image quality [part (h)]. Downsampling the images in the lateral direction by a factor of 4 results the CNR of the axial and lateral strain images to drop respectively 12% (from 16.3 to 14.3) and 56% (from 2.55 to 1.13) as shown in (i). While the axial strain is robust to the number of A-line in the image even at a high strain level of 5%, the lateral strain is sensitive to it (i). Similar study with lower axial strain levels shows that as the axial strain decreases, higher downsampling rates in both axial and lateral directions are possible without a large impact on the results.

4) Kalman Filter: The performance of the Kalman filter is studied using the RF-data used in Fig. 9. The linear least squares
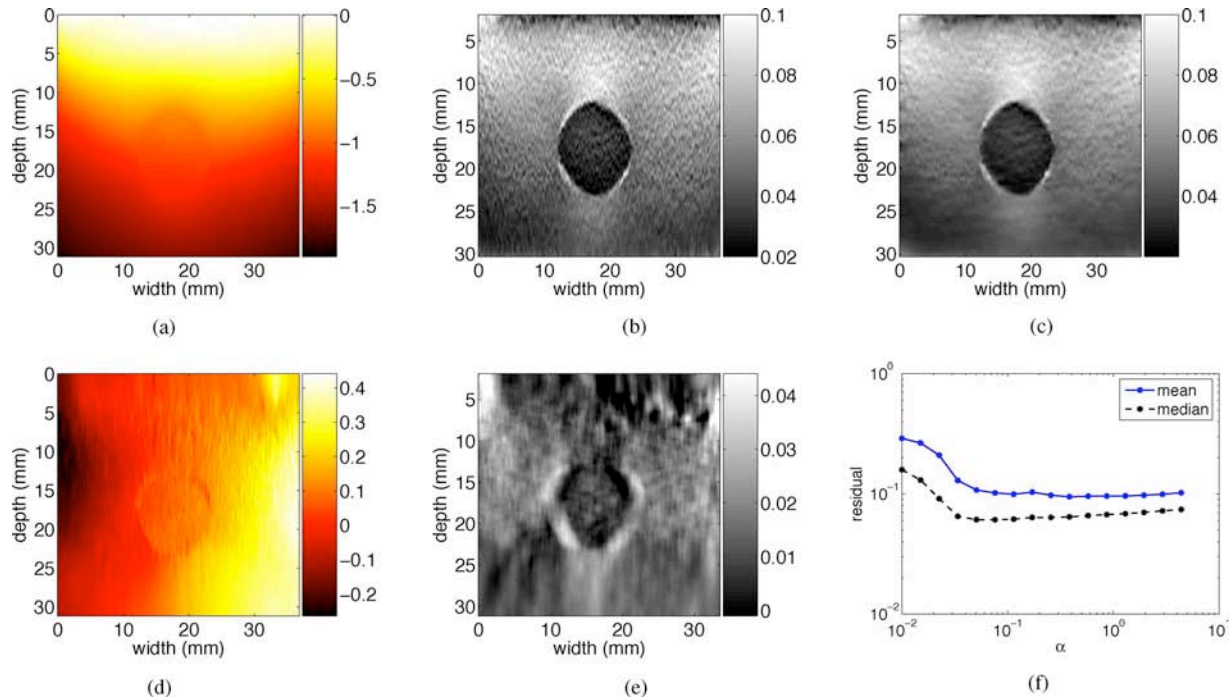
Fig. 9. Phantom experimental results. The top row shows axial displacement and axial strains as labeled (KF in (c) refers to Kalman filter). Average axial strain and maximum strain are approximately 6.6% and 11%. (d) and (e) show lateral displacement and lateral strain, respectively. (f) shows residuals as the regularization weight varies. (a) Axial displacement (mm). (b) Axial strain. (c) Axial strain with KF. (d) Lateral displacement (mm). (e) Lateral strain. (f) Residuals.
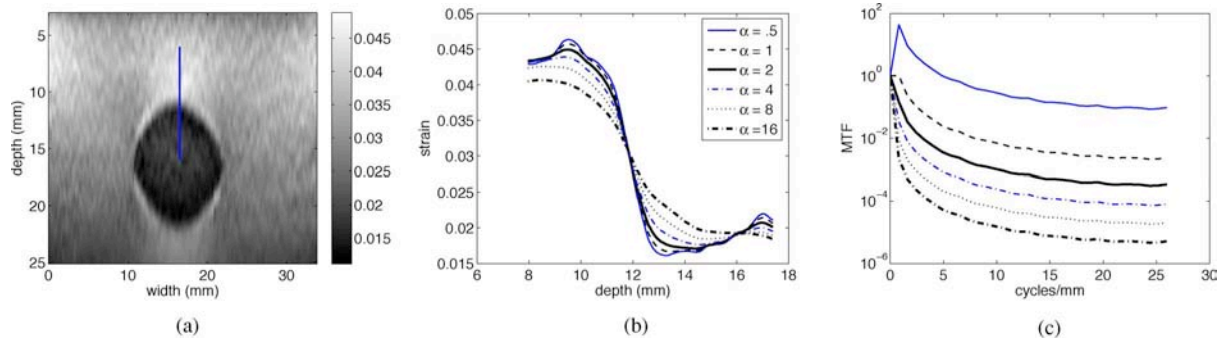

Fig. 10. Phantom experimental results showing the resolution of the 2D AM. (a) Strain image. The edge spread function is evaluated along the vertical line. (b) The strain across the edge [vertical line in (a)] for the five shown regularization values. (c) The MTF calculated across the vertical line in (a). Spatial resolution is defined as the spatial frequency when the value of MTF is 0.1. (a) Axial strain. (b) Strain profile. (c) MTF.

differentiation technique is applied to the axial displacement field calculated with 2D AM, resulting in $z_{i,j}$ [Fig. 12(a)]. The Kalman filter is then applied to $z_{i,j}$ measurements of (a), giving the posterior $\hat{\epsilon}_{i,j}$ measurements of (b). Comparing the strain values at a horizontal line of (a) and (b), the noisy $z_{i,j}$ measurements are smoothed in the lateral direction using the proposed Kalman filter, with minimal blurring of the edge.

B. Clinical Study

Seven patients undergoing open surgical radiofrequency (RF) thermal ablation for primary or secondary liver cancer were enrolled between February 06, 2008 and July 28, 2009. All patients enrolled in the study had unresectable disease and were candidates for RF ablation following review at our institutional multidisciplinary conference. Patients with cirrhosis or suboptimal tumor location were excluded from the study. All patients provided informed consent as part of the protocol, which was approved by the institutional review board. RF ablation was administered using the RITA Model 1500 XRF generator (Rita Medical Systems, Fremont, CA). Strain images are generated offline. Some preliminary results are published in [15].

We show the results from only four patients due to space limitations. Fig. 13 shows the *B*-mode scan, the strain images and CT scans performed after RF ablation. Tissue is simply compressed freehand at a frequency of approximately 1 compression per 2 s with the ultrasound probe without any attachment. The shadow in Fig. 13(a) at 20 mm depth is produced by the thermal lesion. Note that it is not possible to ascertain the size and position of the thermal lesions from *B*-mode images. In addition, the thermal lesion has different appearances in the three *B*-scans. However, the thermal lesions show very well as hard lesions in the strain images. After gross correlation of the post ablation CT scan and the thermal lesion in the strain images, the size of the lesion seems to correspond well. However, a more
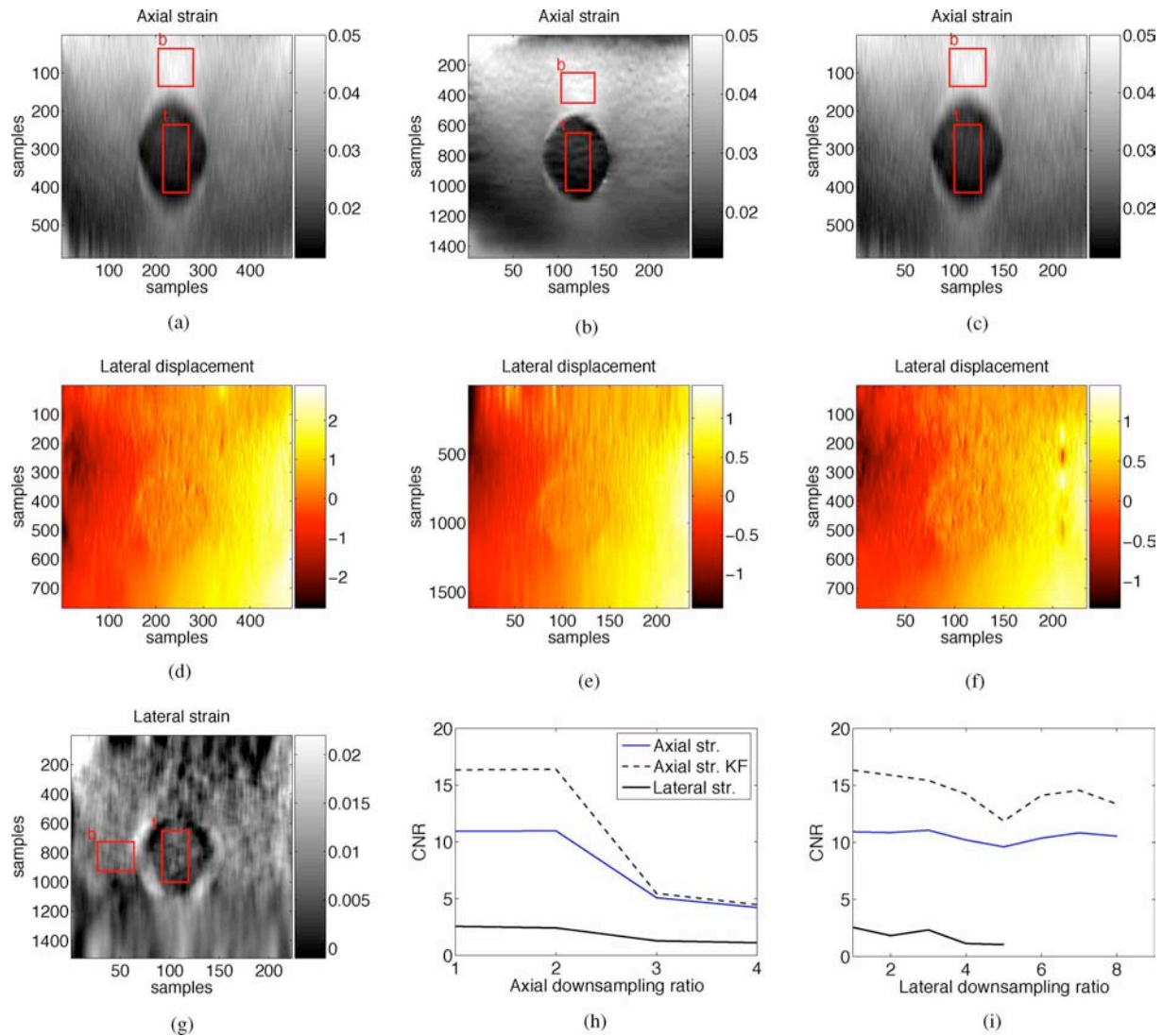
Fig. 11.   Results of the CIRS elastography phantom at 5% maximum strain at different axial and lateral sampling rates. The hard lesion is spherical and has a diameter of 1 cm. Downsampling is performed by simply skipping samples in the axial or (and) lateral directions. In (c) and (f), a downsampling ratio of 2 is applied in both axial and lateral directions. The lateral displacement is shown in number of samples in (d)–(f). (h) and (i) show the CNR between the target and background windows in the strain images as the axial or lateral downsampling rates change. The target and background windows are shown in the axial strain images (a)–(c) and the lateral strain image (g). In (i), the lateral strain curve is not calculated for downsampling ratios of 6 and higher because the background window moves out of the image. The black dashed curve with the highest CNR is the strain obtained with the Kalman filter (KF). (a) Axial downsamp. ratio = 2. (b) Lateral downsamp. ratio = 2. (c) Ax.-lat. downsamp. rat = 2. (d) Axial downsamp. ratio = 2. (e) Lateral downsamp. ratio = 2. (f) Ax.-lat. downsamp. rat = 2. (g) Lateral downsamp. ratio = 2.

rigorous validation of the size and shape of the ablated lesion in the elastography image is underway using nonrigid registration of CT and ultrasound images. To the best of our knowledge, this is also the first demonstration of the success of elastography in imaging the thermal lesion in an *in vivo* human experiment.

We have also acquired patient RF data of liver ablation prior and after ablation in one of the patient trials. Fig. 14 shows the *B*-mode, strain and venous and arterial phase[2] CT images obtained before ablation, and Fig. 15 shows the *B*-mode, strain and lateral displacement images after ablation. In Fig. 14, the tumor [marked in the CT images (f) and (g)] is not visible in

the *B*-mode image (a), but is clearly visible in the strain images (b) and (c). While the tissue is getting compressed with the ultrasound probe, the middle hepatic vein (marked as 5) which is only 4–8 cm from vena cava inferior pulsates at high amplitude. The graph in (e) schematically shows the probe motion and variations in the diameter of the vein. Therefore, the vein can look soft as in (c) or hard as in (b) depending on whether its diameter variation is in the same [marked by ellipse 1 in (e)] or opposite [marked by ellipse 2 in (e)] direction as the probe motion. The effect of pulsation of vessels, a well-known cause of signal decorrelation, is minimized via IRLS resulting in a low noise strain image. In addition, since the 2D AM method gives a dense motion field (same size as RF data), the small artery at the diameter of less than 2 mm [marked as 4 in (a)] is discernible in (b) from the low pressure portal vein. The ablated lesion is also

---

[2]CT scans are performed at different phases after intravenous injection of a contrast agent. In the arterial phase (directly after injection of a contrast agent) arteries will enhance, where as in the venous phase (30–60 s after injection) the hepatic parenchyma and veins will enhance.
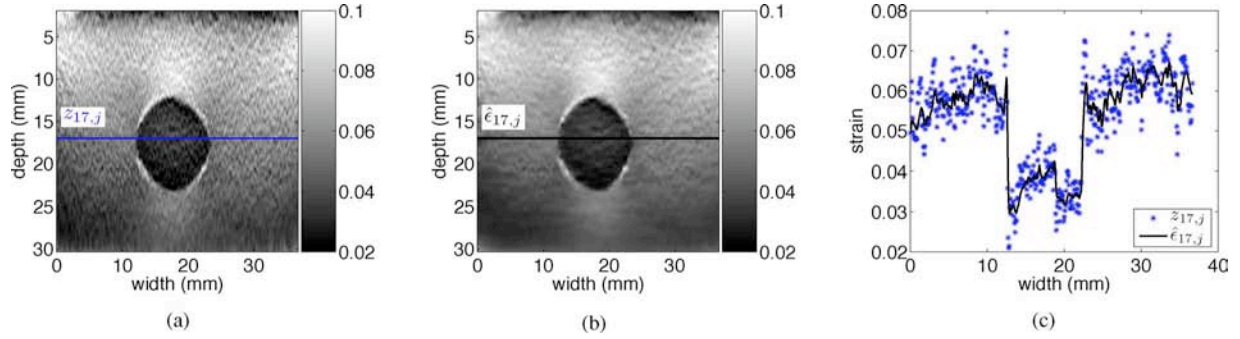
Fig. 12.   (a) Shows the axial strain field calculated by least squares regression of the noisy displacement field. (b) depicts the strain field calculated from the noisy measurements of (a) using the proposed Kalman filter (KF in (a) and (b) refers to Kalman filter). The pixels of images in (a) and (b) are respectively the least squares measurements $z_{i,j}$, and posterior strain values $\hat{\epsilon}_{i,j}$. (c) shows the strain estimation at the 17 mm deep horizontal line shown in (a) to (b). The Kalman filter removes the noise while keeping the image sharp, due to the variable model noise of (27). (a) Strain without KF. (b) Strain with KF. (c) Strain plots.
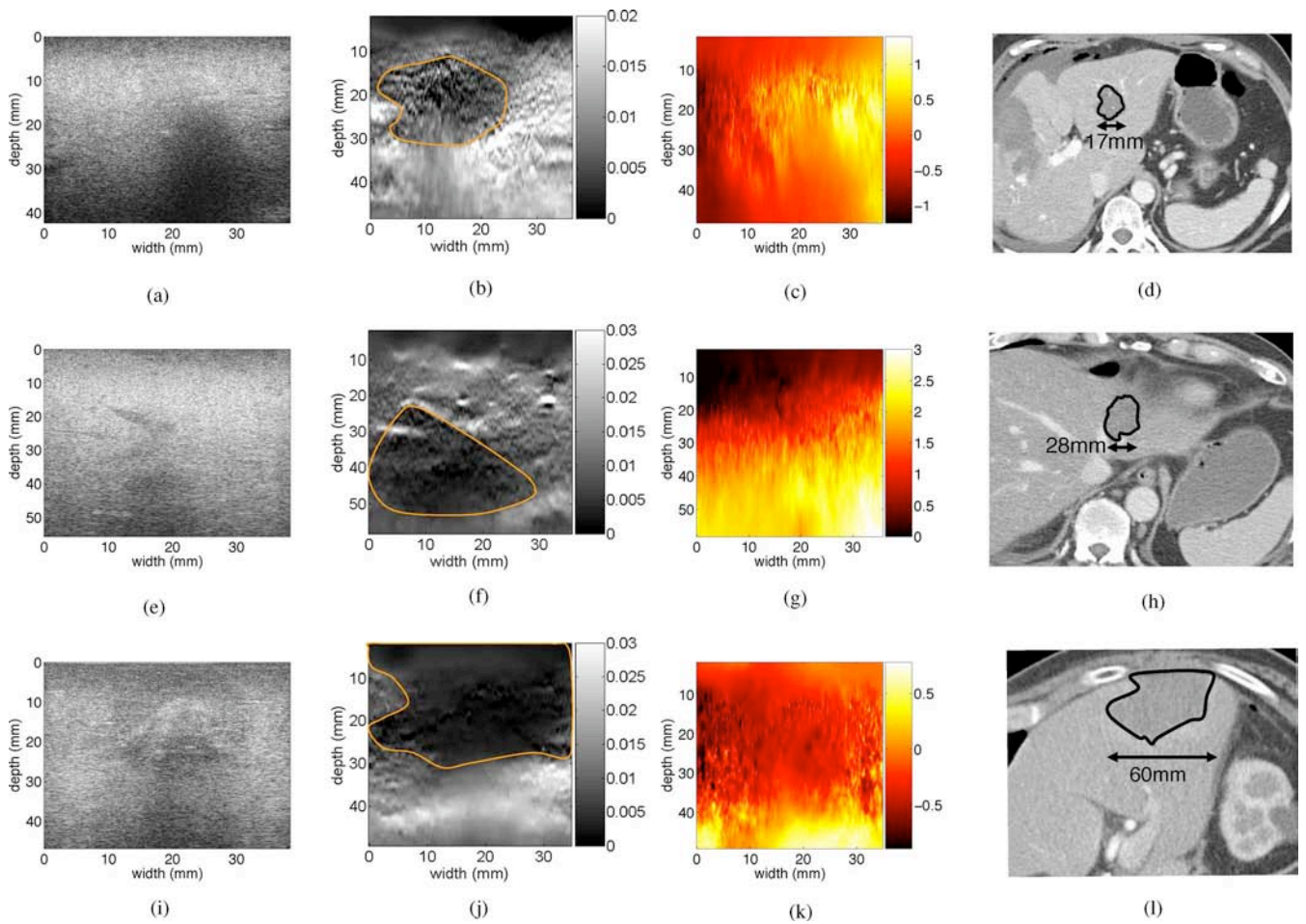

Fig. 13.   *In vivo* images of the thermal lesion produced by RF ablation therapy of liver cancer. All images acquired after ablation. First, second, and third rows correspond to the first, second and third patients respectively. The thermal lesion shows in (b), (f) and (j) as dark, surrounded by normal tissue in white. The lateral displacement images are shown in number of samples (they do not immediately carry anatomical information). In (b), (d), (f), (h), (j), and (l) the delineated thermal lesions is shown. The nonunity aspect ratio in the axes of the *B*-mode and strain images should be considered when comparing them to the CT scans. (a) *B*-mode patient 1. (b) Axial strain. (c) Lateral displacement. (d) CT patient 1. (e) *B*-mode patient 2. (f) Axial strain. (g) Lateral displacement. (h) CT patient 2. (i) *B*-mode patient 3. (j) Axial strain. (k) Lateral displacement. (l) CT patient 3.

discernible in the strain images of Fig. 15(b) and (c). We believe the soft region in the middle of the two hard ablation lesions in (b) and (c) (at the depth of 25–30 mm and width of 10–25 mm) is not close to any of the 10 tines of the ablation probe. Therefore because of its proximity to veins and vessels its temperature has remained low.

V. DISCUSSION

The resolution of the method is formally studied in Section IV-A using the phantom experiment. Future work will include more intuitive measures for resolution in terms of the smallest detectable target as a function of its elasticity difference with the background.
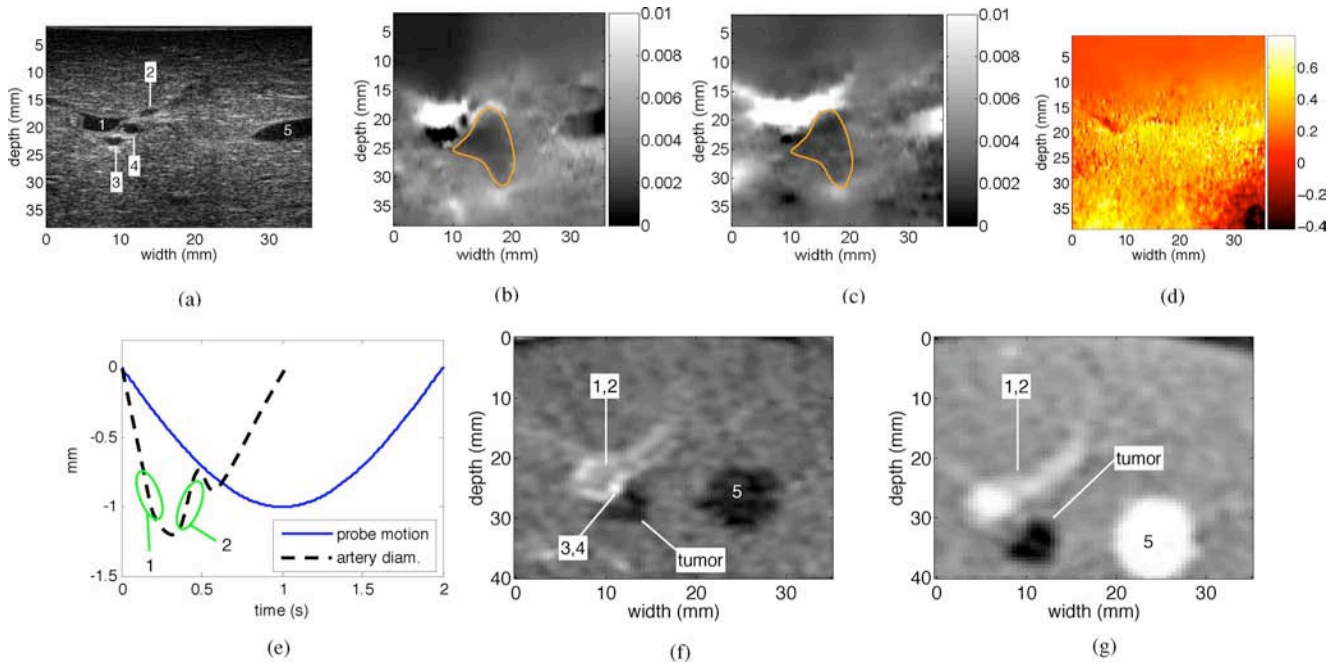
Fig. 14. *In vivo* images of the fourth patient before RF ablation. In (a), the left anterior branch of portal vein is marked as 1 and 2 and has low pressure and therefore compresses easily. Arteries (marked as 3 and 4) and the middle hepatic vein (marked as 5) however pulsate with the heart beat and may have low or high pressure. (b) and (c) both show the axial strain from the same location before ablation. They are calculated at two different phases of the heart beat. The cancer tumor is discernible in (b) and (c) (regardless of the systolic or diastolic blood pressure), and its boundary is shown. 1 and 2 [as marked in (a)] correspond to the high strain area in both (b) and (c). Since 3, 4, and 5 [as marked in (a)] pulsate, they may look hard [as in (b)] or soft [as in (c)]. (d) shows the lateral displacement. The tumors is not visible in this image. (e) shows the motion of the probe and the variation in the diameter of the arteries due to the heart beat (refer to the text). (f) is the arterial phase and (g) is the venous phase contrast CT images. The numbers 1–5 mark the same anatomy as (a). (a) *B*-mode pre-ablation. (b) Axial strain pre-ablation. (c) Axial strain pre-ablation. (d) Lateral displacement pre-ablation. (e). (f) CT pre-ablation. (g) CT pre-ablation.
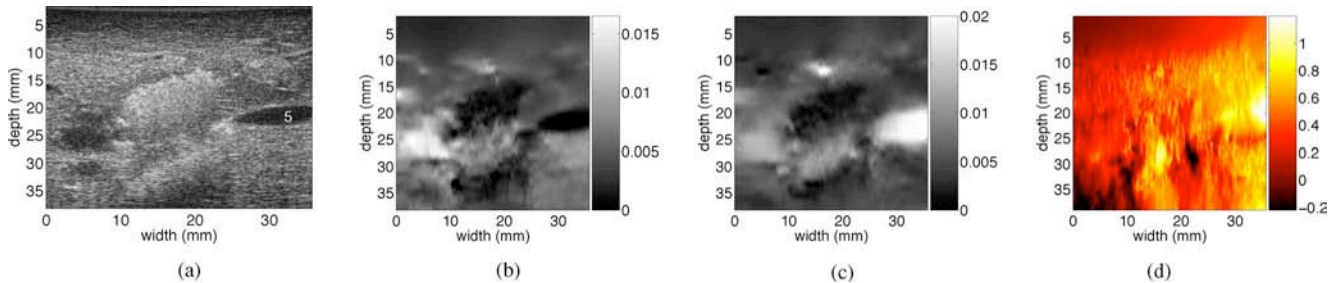

Fig. 15. *In vivo* images of the fourth patient after RF ablation. Similar to Fig. 14, the hepatic vein (marked as 5) can have low strain [as in (b)] or high strain [as in (c)] values. (a) *B*-mode post-ablation. (b) Axial strain post-ablation. (c) Axial strain postablation. (d) Lateral displacement postablation.

The cost function is a regularized function of all displacements on an A-line. This makes the methods robust to noise which exist throughout the image. Besides, the AM methods are not window-based and therefore they do not suffer from decorrelation within the window. As a result, both AM methods work for strains as high as 10%. In addition, the IRLS outlier rejection technique makes the AM methods robust to local sources of decorrelation such as out-of-plane motion of movable structures or blood flow.

Global stretching assumes a constant strain across the depth and stretches one of the RF-limes accordingly. It is shown that it enhances the quality of correlation based elastography methods. The reason is that the strain of each point can be assumed to be the global strain (fixed for each RF-line) plus some perturbation, i.e., constant strain is a better approximation than zero strain. Biasing the regularization is motivated by the same reason and involves almost no additional computational cost.

Improvement in the SNR and CNR achieved with Kalman filtering differentiation is due to utilizing the (piecewise) continuity of the strain field. One could think of a unified framework which includes both the 2D AM and the Kalman filtering and directly calculates the strain field. We made an effort to formulate (15) in terms of strain values. Unfortunately, the coefficient matrix in the left-hand side. became a full matrix for our desired regularization. Such large full system cannot be solved in real-time.

The least squares differentiation of Section II-D can be incorporated in the Kalman filter. This can be simply done by defining the state at each point to be the displacement and the strain of that point. The observed variables are the noisy displacement measurements from 2D AM. Solving for the state gives a strain estimate at each point. However, we preferred to follow the common approach of first finding the strain by solving least squares. In addition, the axial and lateral displace-

ments can be considered as two channels of a measurement and a Kalman filter that takes into account both intra-channel (spatial) and inter-channel variations can be developed. This is a subject of future work.

Lateral displacement estimation with 2D AM is of order of magnitude less accurate than the axial displacement estimates. We tested the following algorithm for calculating the lateral displacement field based on 1D AM: run 1D AM to find the axial displacement field A, then transpose both ultrasound images I_1 and I_2 and run 1D AM again using A calculated in the previous step. The axial displacement field calculated for the transposed images is in fact the lateral displacement of the original images. Although considerably more computationally expensive than 2D AM, this algorithm did not improve the lateral displacement estimation. Therefore only images of lateral displacement are provided for the patient trials because the lateral strain did not show the ablation lesion. This is in accordance with recent work [36] which only shows the lateral displacement. A 2D displacement field can be utilized to calculate the thermal expansion and to reconstruct the strain tensor. Incorporation of the synthetic lateral phase [61]–[63], into 2D AM to further improve the accuracy of the lateral displacement measurement is also a subject of future work.

In cases where the two ultrasound frames correlate very poorly throughout the image, 1D AM outperforms 2D AM because DP is run for the entire image in 1D AM. However, in those cases the strain images are of very low quality even with 1D AM. In cases where the images correlate reasonably, the 2D AM algorithm slightly outperforms 1D AM in terms of the SNR of the axial strain as shown in Fig. 3(e) and (f). Also, 1D AM and 2D AM are very similar in terms of bias and variance as mentioned in the caption of the Fig. 5. And finally, 2D AM is more than 10 times faster than 1D AM because it eliminates the redundant calculations in the DP step of 1D AM. This is important considering that there are combinatorial many ways of choosing two frames for elastography from a sequence of images. Having a fast algorithm, like 2D AM, makes it plausible to invest time to perform real-time frame selection, an area that we are currently working on [16], [64].

Recent work [65] has attempted to reconstruct elasticity from the displacement field for monitoring thermal ablation. It has also shown that [66] compared to strain images, elasticity images have both higher correlation with the ablation zone and give higher CNR. Another work [67] has utilized the solution of the elasticity reconstruction to improve motion estimation in an iterative framework. Calculation of the elasticity modulus in our ablation monitoring trials is an area of future work.

Statistical analysis of the residuals is a subject of future work. The sum of squared differences used as the similarity metric in our cost function is suitable if ultrasound noise can be modeled as additive Gaussian noise. However, ultrasound noise is not simply additive Gaussian and it has been shown that similarity metrics that model the noise process considering physics of ultrasound give more accurate results [68]. Performance of the 2D AM method for images that are not fully developed speckles (i.e., have few scatterers per resolution cell) is also a subject of future work.

Current implementations of the 1D AM and 2D AM take, respectively, 0.4 s and 0.04 s to generate strain images (axial for 1D AM and axial and lateral for 2D AM) of size 1000×100 on a 3.8 GHz P4 CPU. DP contributes to more than 90% of the running time of the 1D AM, and that's why it is slower than 2D AM where DP is only run for a single A-line. The running time of both methods changes linearly with the size of the image.

VI. CONCLUSION

Two regularized elastography methods, 1D AM and 2D AM, are introduced for calculating the motion field between two ultrasound images. They both give dense subsample motion fields (1D AM gives subsample axial and integer sample lateral and 2D AM gives subsample axial and lateral) in real-time. The size of the motion fields is the same as the size of the RF-data (except for few samples from the boundary whose displacements are not calculated). Such dense motion fields lead to dense strain fields which are critical in detecting small lesions. The prior of tissue motion continuity is exploited in the AM methods to minimize the effect of signal decorrelation. The regularization term is biased with the average strain in the image to minimize underestimation of the strain values. Parts of the image that have very low correlation are treated as outliers and their effect is minimized via IRLS. The strain image is calculated by differentiating the motion fields using least squares regression and Kalman filtering. The performance of the proposed elastography algorithms is analyzed using Field II and finite element simulations, and phantom experiments. Clinical trials of monitoring RF ablation therapy for liver cancer in four patients are also presented. An implementation of the 2D AM method, the least squares regression and the Kalman filter in MATLAB mex functions, as well as some of the phantom and patient RF data used in this work are available for academic research and can be downloaded.[3]

REFERENCES

[1] K. Parker, L. Taylor, S. Gracewski, and D. Rubens, "A unified view of imaging the elastic properties of tissue," *J. Acoust. Soc. Amer.*, vol. 117, pp. 2705–2712, May 2005.

[2] J. Greenleaf, M. Fatemi, and M. Insana, "Selected methods for imaging elastic properties of biological tissues," *Annu. Rev. Biomed.*, vol. 5, pp. 57–78, Apr. 2003.

[3] J. Ophir, S. Alam, B. Garra, F. Kallel, E. Konofagou, T. Krouskop, and T. Varghese, "Elastography," *Annu. Rev. Biomed. Eng.*, vol. 213, pp. 203–233, Nov. 1999.

[4] L. Gao, K. Parker, R. Lerner, and S. Levinson, "Imaging of the elastic properties of tissue—A review," *Ultrasound Med. Biol.*, vol. 22, no. 8, pp. 959–977, Aug. 1996.

[5] K. Hiltawsky, M. Kruger, C. Starke, L. Heuser, H. Ermert, and A. Jensen, "Freehand ultrasound elastography of breast lesions: Clinical results," *Ultrasound Med. Biol.*, vol. 27, pp. 1461–1469, Nov. 2001.

[6] M. Doyley, J. Bamber, F. Fuechsel, and N. Bush, "A freehand elastographic imaging approach for clinical breast imaging: System development and performance evaluation," *Ultrasound Med. Biol.*, vol. 27, pp. 1347–1357, 2001.

[3]http://www.cs.jhu.edu/~rivaz/UltrasoundElastography/

[7] M. Yamakawa, N. Nitta, T. Shiina, T. Matsumura, S. Tamano, T. Mitake, and E. Ueno, "High-speed freehand tissue elasticity imaging for breast diagnosis," *Jpn. J. Appl. Phys.*, vol. 42, no. 5B, pp. 3265–3270, May 2003.

[8] T. Hall, Y. Zhu, and C. Spalding, "In vivo real-time freehand palpation imaging," *Ultrasound Med. Biol.*, vol. 29, pp. 427–435, Mar. 2003.

[9] J. Lindop, G. Treece, A. Gee, and R. Prager, "3D elastography using freehand ultrasound," *Ultrasound Med. Biol.*, vol. 32, pp. 529–545, Apr. 2006.

[10] E. Turgay, S. Salcudean, and R. Rohling, "Identifying the mechanical properties of tissue by ultrasound strain imaging," *Ultrasound Med. Biol.*, vol. 32, no. 2, pp. 221–235, Feb. 2006.

[11] A. Lorenz, H. Sommerfeld, M. Garcia-Schurmann, S. Philippou, T. Senge, and H. Ermert, "A new system for the acquisition of ultrasonic multicompression strain images of the human prostate in vivo," *IEEE Trans. Ultrason. Ferroelectr. Freq. Control*, vol. 46, no. 9, pp. 1147–1154, Sep. 1999.

[12] E. Konofagou, J. D'hooge, and J. Ophir, "Myocardial elastography—A feasibility study in vivo," *Ultrasound Med. Biol.*, vol. 28, no. 4, pp. 475–482, Apr. 2002.

[13] J. Rubin, S. Aglyamov, T. Wakefield, M. ODonnell, and S. Emelianov, "Internal displacement and strain imaging using ultrasound speckle tracking," *IEEE Trans. Ultrason. Ferroelectr. Freq. Control*, vol. 22, pp. 443–448, 2003.

[14] T. Varghese, J. Zagzebski, and F. Lee, "Elastography imaging of thermal lesion in the liver following radio frequency ablation: Preliminary results," *Ultrasound Med. Biol.*, vol. 28, no. 11, pp. 1467–1473, 2002.

[15] H. Rivaz, I. Fleming, L. Assumpcao, G. Fichtinger, U. Hamper, M. Choti, G. Hager, and E. Boctor, "Ablation monitoring with elastography: 2d in-vivo and 3d ex-vivo studies," in *Med. Image Comput. Comput. Assist. Intervent. MICCAI*, New York, Sep. 2008, pp. 458–466.

[16] H. Rivaz, P. Foroughi, I. Fleming, R. Zellars, E. Boctor, and G. Hager, "Tracked regularized ultrasound elastography for targeting breast radiotherapy," in *Med. Image Comput. Computer Assist. Intervent. MICCAI*, London, U.K., Sep. 2009, pp. 507–515.

[17] A. Lyshchik *et al.*, "Thyroid gland tumor diagnosis at US elastography," *Radiology*, vol. 237, no. 1, pp. 202–211, Aug. 2005.

[18] F. Viola and W. Walker, "A comparison of the performance of time-delay estimators in medical ultrasound," *IEEE Trans. Ultrason. Ferroelectr. Freq. Control*, vol. 50, no. 4, pp. 392–401, Apr. 2003.

[19] A. Pesavento, C. Perrey, M. Krueger, and H. Ermert, "A time efficient and accurate strain estimation concept for ultrasonic elastography using iterative phase zero estimation," *IEEE Trans. Ultrason. Ferroelectr. Freq. Control*, vol. 46, pp. 1057–1067, Sep. 1999.

[20] H. Hasegawa and H. Kanai, "Improving accuracy in estimation of artery wall displacement by referring to center frequency of RF echo," *IEEE Trans. Ultrason. Ferroelectr. Freq. Control*, vol. 53, no. 1, pp. 52–63, Jan. 1999.

[21] J. Lindop, G. Treece, A. Gee, and R. Prager, "Phase-based ultrasonic deformation estimation," *IEEE Trans. Ultrason. Ferroelectr. Freq. Control*, vol. 55, no. 1, pp. 94–111, 2008.

[22] W. Walker and G. Trahey, "A fundamental limit on delay estimation using partially correlated speckle signals," *IEEE Trans. Ultrason. Ferroelectr. Freq. Control*, vol. 42, no. 2, pp. 301–308, Mar. 1995.

[23] F. Yeung, S. Levinson, and K. Parker, "Multilevel and motion model-based ultrasonic speckle tracking algorithms," *Ultrasound Med. Biol.*, vol. 24, pp. 427–441, Mar. 1998.

[24] M. O'Donnell, R. Skovoroda, M. Shapo, and S. Emelianov, "Internal displacement and strain imaging using ultrasonic speckle tracking," *IEEE Trans. Ultrason. Ferroelectr. Freq. Control*, vol. 41, no. 3, pp. 314–325, Mar. 1994.

[25] C. Sumi, "Usefulness of ultrasonic strain measurement-based shear modulus reconstruction for diagnosis and thermal treatment," *IEEE Trans. Ultrason. Ferroelectr. Freq. Control*, vol. 52, no. 10, pp. 1670–1689, Oct. 2005.

[26] P. Barbone and J. Bamber, "Quantitative elasticity imaging: What can and cannot be inferred from strain images," *Phys. Med. Biol.*, vol. 47, pp. 2147–2164, Jun. 2002.

[27] C. Sumi, "Reconstructions of shear modulus, Poisson's ratio, and density using approximate mean normal stress lambda epsilon alpha alpha as unknown," *IEEE Trans. Ultrason. Ferroelectr. Freq. Control*, vol. 53, no. 12, pp. 2416–2434, Dec. 2006.

[28] L. Bohs and G. Trahey, "A novel method for angle independent ultrasonic imaging of blood flow and tissue motion," *IEEE Trans. Ultrason. Ferroelectr. Freq. Control*, vol. 38, no. 3, pp. 280–286, Mar. 1991.

[29] P. Chaturvedi, M. Insana, and T. Hall, "2-d companding for noise reduction in strain imaging," *IEEE Trans. Ultrason. Ferroelectr. Freq. Control*, vol. 45, no. 1, pp. 179–191, Jan. 1998.

[30] M. Rao, Q. Chen, H. Shi, T. Varghese, E. Madsen, J. Zagzebski, and T. Wilson, "Normal and shear strain estimation using beam steering on linear-array transducers," *Ultrasound Med. Biol.*, vol. 33, no. 1, pp. 57–66, Jan. 2007.

[31] E. Konofagou and J. Ophir, "A new elastographic method for estimation and imaging of lateral displacements, lateral strains, corrected axial strains and Poisson's ratios in tissues," *Ultrasound Med. Biol.*, vol. 24, no. 8, pp. 1183–1199, 1998.

[32] R. Maurice, J. Ohayon, Y. Fretigny, M. Bertrand, G. Soulez, and G. Cloutier, "Noninvasive vascular elastography: Theoretical framework," *IEEE Trans. Med. Imag.*, vol. 23, no. 2, pp. 164–180, Feb. 2004.

[33] R. Maurice and M. Bertrand, "Lagrangian speckle model and tissue-motion estimation theory," *IEEE Trans. Med. Imag.*, vol. 18, no. 7, pp. 593–603, Jul. 1999.

[34] M. Lubinski, S. Emelianov, K. Raghavan, A. Yagle, A. Skovoroda, and M. O'Donnell, "Lateral displacement estimation using tissue incompressibility," *IEEE Trans. Ultrason. Ferroelectr. Freq. Control*, vol. 43, no. 2, pp. 247–255, Mar. 1996.

[35] C. Pellot-Barakat, F. Frouin, M. Insana, and A. Herment, "Ultrasound elastography based on multiscale estimations of regularized displacement fields," *IEEE Trans. Med. Imag.*, vol. 23, no. 2, pp. 153–163, Feb. 2004.

[36] E. Brusseau, J. Kybic, J. Deprez, and O. Basset, "2-D locally regularized tissue strain estimation from radio-frequency ultrasound images: Theoretical developments and results on experimental data," *IEEE Trans. Med. Imag.*, vol. 27, no. 2, pp. 145–160, Feb. 2008.

[37] C. Sumi, "Regularization of tissue shear modulus reconstruction using strain variance," *IEEE Trans. Ultrason. Ferroelectr. Freq. Control*, vol. 55, no. 2, pp. 297–307, Feb. 2008.

[38] C. Sumi and K. Sato, "Regularization for ultrasonic measurements of tissue displacement vector and strain tensor," *IEEE Trans. Ultrason. Ferroelectr. Freq. Control*, vol. 55, no. 4, pp. 787–799, Apr. 2008.

[39] G. Treece, J. Lindop, A. Gee, and R. Prager, "Uniform precision ultrasound strain imaging," *IEEE Trans. Ultrason. Ferroelectr. Freq. Control*, vol. 56, no. 11, pp. 2420–2436, Nov. 2009.

[40] H. Rivaz, E. Boctor, P. Foroughi, G. Fichtinger, and G. Hager, "Ultrasound elastography: A dynamic programming approach," *IEEE Trans. Med. Imag.*, vol. 27, no. 10, pp. 1373–1377, Oct. 2008.

[41] G. Welch and G. Bishop, An introduction to the Kalman filter Univ. North Carolina, Chapel Hill, TR 95-041, 1995.

[42] A. Amini, T. Weymouth, and R. Jain, "Using dynamic programming for solving variational problems in vision," *IEEE Trans. Pattern Anal. Mach. Intell.*, vol. 12, no. 9, pp. 855–867, Sep. 1990.

[43] P. Huber, *Robust Statistics*. New York: Wiley.

[44] G. Hager and P. Belhumeur, "Efficient region tracking with parametric models of geometry and illumination," *IEEE Trans. Pattern Anal. Mach. Intell.*, vol. 20, no. 10, pp. 1025–1039, Oct. 1998.

[45] P. Holland and R. Welsch, "Robust regression using iteratively reweighted least squares,," *Commun. Statist. Theory Methods*, vol. A6, pp. 813–827, 1977.

[46] L. Sandrin, M. Tanter, S. Catheline, and M. Fink, "Shear modulus imaging with 2-D transient elastography," *IEEE Trans. Ultrason. Ferroelectr. Freq. Control*, vol. 49, no. 4, pp. 426–435, Apr. 2002.

[47] M. Tanter, J. Bercoff, L. Sandrin, and M. Fink, "Ultrafast compound imaging for 2-d motion vector estimation: Application to transient elastography," *IEEE Trans. Ultrason. Ferroelectr. Freq. Control*, vol. 49, no. 10, pp. 1363–1374, Oct. 2002.

[48] L. Chen, G. Treece, J. Lindop, A. Gee, and R. Prager, "A quality-guided displacement tracking algorithm for ultrasonic elasticity imaging," *Med. Imag. Anal.*, vol. 13, no. 2, pp. 286–296, Apr. 2009.

[49] J. Prince and J. Links, *Medical Imaging Signals and Systems*. Upper Saddle River, NJ: Prentice Hall, 2006.

[50] H. Shum and R. Szeliski, "Construction of panoramic mosaics with global and local alignment," *Int. J. Comput. Vis.*, vol. 36, no. 2, pp. 101–130, 2000.

[51] S. Baker and I. Matthews, "Lucas-kanade 20 years on: A unifying framework," *Int. J. Comput. Vis.*, vol. 56, no. 3, pp. 221–255, Feb. 2004.

[52] R. Dugad and N. Ahuja, "Video denoising by combining Kalman and Wiener estimates," in *Int. Conf. Image Process. ICIP*, 1999, vol. 4, pp. 152–156.

[53] A. Jensen, "Field: A program for simulating ultrasound systems," *Med. Biol. Eng. Comput.*, vol. 34, pp. 351–353, 1996.

[54] R. Wagner, S. Smith, J. Sandrik, and H. Lopez, "Statistics of speckle in ultrasound B-Scans," *IEEE Trans. Sonics Ultrasonics*, vol. 17, no. 3, pp. 251–268, May 1983.

[55] H. Rivaz, E. Boctor, and G. Fichtinger, "Ultrasound speckle detection using low order moments," in *IEEE Int. Ultrason. Symp.*, Oct. 2006, pp. 2092–2095.

[56] D. Bertsimas and J. Tsitsiklis, *Biomechanics: Mechanical Properties of Living Tissues*. New York: Springer-Verlag, 1993.

[57] T. Krouskop, T. Wheeler, F. Kallel, B. Garra, and T. Hall, "The elastic moduli of breast and prostate tissues under compression," *Ultrason. Imag.*, vol. 20, pp. 260–274, 1998.

[58] J. Liu, K. Abbey, and M. Insana, "Linear approach to axial resolution in elasticity imaging," *IEEE Trans. Ultrason. Ferroelectr. Freq. Control*, vol. 51, no. 6, pp. 716–725, Jun. 2004.

[59] R. Padgett and C. Korte, "Assessment of the effects of pixel loss on image quality in direct digital radiography," *Phys. Med. Biol.*, vol. 49, no. 6, pp. 977–986, Mar. 2004.

[60] M. Doyley, Q. Feng, J. Weaver, and K. Paulsen, "Performance analysis of steady-state harmonic elastography," *Phys. Med. Biol.*, vol. 52, no. 10, pp. 2657–2674, May 2007.

[61] X. Chen, M. Zohdy, S. Emelianov, and M. O'Donnell, "Lateral speckle tracking using synthetic lateral phase," *IEEE Trans. Ultrason. Ferroelectr. Freq. Control*, vol. 51, no. 5, pp. 540–550, May 2004.

[62] E. Ebbini, "Phase-coupled two-dimensional speckle tracking algorithm," *IEEE Trans. Ultrason. Ferroelectr. Freq. Control*, vol. 53, no. 5, pp. 972–990, May 2006.

[63] C. Sumi, "Displacement vector measurement using instantaneous ultrasound signal phase—Multidimensional autocorrelation and Doppler methods," *IEEE Trans. Ultrason. Ferroelectr. Freq. Control*, vol. 55, no. 1, pp. 24–43, Jan. 2008.

[64] P. Foroughi, H. Rivaz, I. Fleming, G. Hager, and E. Boctor, "Tracked ultrasound elastography (true)," *Med. Image Computing Computer Assist. Intervent.*, to be published.

[65] J. Jiang, T. Varghese, E. M. C. Brace, T. Hall, S. Bharat, M. Hobson, J. Zagzebski, and F. Lee, "Youngs modulus reconstruction for radio frequency ablation electrode-induced displacement fields: A feasibility study," *IEEE Trans. Med. Imag.*, vol. 28, pp. 1325–1334, Aug. 2009.

[66] J. Jiang, C. Brace, A. Andreano, R. DeWall, N. Rubert, T. Pavan, T. Fisher, T. Varghese, F. Lee, and T. Hall, "Ultrasound-based relative elastic modulus imaging for visualizing thermal ablation zones in a porcine model," *Phys. Med. Biol.*, vol. 55, pp. 2281–2306, 2010.

[67] M. Miga, "A new approach to elastography using mutual information and finite elements," *Phys. Med. Biol.*, vol. 48, pp. 467–480, 2003.

[68] M. Insana, L. Cook, M. Bilgen, P. Chaturvedi, and Y. Zhu, "Maximum-liklihood approach to strain imaging using ultrasound," *IEEE Trans. Ultrason. Ferroelectr. Freq. Control*, vol. 107, no. 3, pp. 1421–1434, 2000.

Ablation Monitoring with Elastography: 2D *In-vivo* and 3D *Ex-vivo* Studies

Hassan Rivaz*, Ioana Fleming, Lia Assumpcao, Gabor Fichtinger,
Ulrike Hamper, Michael Choti, Gregory Hager, and Emad Boctor

ERC for Computer Integrated Surgery, Johns Hopkins University. Dept. of Surgical
Oncology, Johns Hopkins Medicine. School of Computing, Queens University
{rivaz,inicola1}@jhu.edu, eboctor1@jhmi.edu

Abstract. The clinical feasibility of 2D elastography methods is hindered by the requirement that the operator avoid out-of-plane motion of the ultrasound image during palpation, and also by the lack of volumetric elastography measurements. In this paper, we develop and evaluate a 3D elastography method operating on volumetric data acquired from a 3D probe. Our method is based on minimizing a cost function using dynamic programming (DP). The cost function incorporates similarity of echo amplitudes and displacement continuity. We present, to the best of our knowledge, the first *in-vivo* patient studies of monitoring liver ablation with freehand DP elastography. The thermal lesion was not discernable in the B-mode image but it was clearly visible in the strain image as well as in validation CT. We also present 3D strain images from thermal lesions in *ex-vivo* ablation. Good agreement was observed between strain images, CT and gross pathology.

1 Introduction

Hepatocellular carcinoma (HCC) is one of the most common tumors, causing 662,000 deaths worldwide annually. Minimally invasive RF ablation [1] has gained much interest recently since only 10% to 20% of patients with HCC are amenable to traditional therapy of surgical resection of the tumor. In RF ablation, an electrode is placed into the tumor to cauterize it [1]. Monitoring the ablation process in order to document adequacy of margins during treatment is a significant importance. Ultrasonography is the most common modality for both target imaging and for ablation monitoring. However, ultrasonographic appearance of ablated tumors only reveals hyperechoic areas due to microbubbles and outgasing and cannot adequately visualize the margin of tissue coagulation.

Accordingly, ultrasound elastography (Ophir et al, 1991) has emerged as a useful augmentation to conventional ultrasound imaging. Elastography has been used for monitoring RF ablation [2], [3] by observing that ablated region is harder than surrounding tissue. In the most common variation of elastography, ultrasound images are captured while the tissue is being compressed, and images

---

* Supported by the Link Foundation Fellowship.

are processed to provide a grid of local displacement measurements. These displacement fields are then used to determine the elastic properties of the tissue at each grid location. The grid of calculated elastic properties can be displayed as an image.

Elastography is computationally expensive, making it challenging to display strain images in real-time. Real-time feedback, however, is required for image guided ablation operations. Another aspect is that signal decorrelation between the pre- and post-compression images induces significant noise in the obtained displacement map and is one of the major limiting factors in elastography [4]. Methods based on cross-correlation and phase zero estimation are currently the most popular real-time elastography techniques which provide fast and accurate motion tracking. In RF ablation, however, high decorrelation between pre- and post-compression images results in high noise in the strain images obtained using cross-correlation [3]. Phase zero estimation methods require an estimate of the center frequency of the ultrasound RF signal, which varies with depth due to frequency-dependent attenuation in tissue [5]. This variation can be significant in RF ablation, leading to poor displacement estimation [5].

We have recently developed a real-time 2D elastography method based on dynamic programming (DP) [6]. The method is more robust to signal decorrelation than standard cross-correlation methods and is therefore a good candidate for ablation monitoring where being real-time and robustness to noise are critically important. Here we report, to the best of our knowledge, the first *in-vivo* patient results on monitoring RF ablation with 2D DP elastography and corroborate the results with CT scans. As initial clinical studies revealed limitations of 2D elastography in monitoring the thermal ablation, we were compelled to progress toward 3D. We think the readership will find it informative to see how our concept and methodology evolved. We extend our DP method to operate on 3D volumes. The benefits of 3D strain imaging of RF ablation are two-fold: 1) 3D imaging eliminates the need to image the same plane while palpating the tissue, which can be very difficult in the presence of breathing and cardiac motion, and 2) 3D imaging allows more precise monitoring of temperature deposition which exhibits variations in 3D, particularly in the presence of blood vessels which act as heat sinks. Previous work has generated 3D elastography by moving a conventional 2D probe out-of-plane using mechanical guidance [7,8] or freehand [9]. In recent work by Treece et al. [10] and Fisher et al. [11] a 3D probe is used to acquire 3D elastography, using phase zero and cross-correlation based motion tracking methods respectively. Here, we use 3D probe to acquire 3D data and introduce a 3D DP motion tracking algorithm. We show that 3D elastography can be successfully used to monitor ablation in 3D.

2   3D Displacement Estimation Using DP

Compared to other optimization techniques, DP is an efficient non-iterative method of global optimization [12,13]. We have recently developed a real-time

2D elastography method using DP [6]. In DP elastography, a cost function which incorporates similarity of echo amplitudes and displacement continuity is minimized. Since data alone can be insufficient to solve ambiguities of motion tracking due to signal decorrelation, the physical priors of tissue motion continuity increases the robustness of the technique [6]. We have showed that DP generates high quality strain images of freehand palpation elastography with up to 10% compression, indicating that the method is more robust to signal decorrelation (caused by scatterer motion in high axial compression and non-axial motions of the probe) in comparison to the standard correlation techniques. The method operates in less than 1sec and is thus also suitable for real time elastography.

Here, we extend this method to operate on 3D volumes. Devising a DP algorithm for optimization involves:

1. Breaking the total optimization cost into a sum of individual costs, such that each cost corresponds to a discrete decision. The decisions should follow each other sequentially and the cost corresponding to each decision should only depend on the previous and not the future decisions (causality).
2. Determining what decisions are possible at each stage.
3. Writing a recursion on the optimal cost from the first stage to the final stage.

Let $g_j^k(i)$ be the intensity of the ith sample (axial direction), j^{th} A-line (lateral direction) and k^{th} frame (out-of-plane direction) of the pre-compression ultrasound volume. Let $g_{j+d_l}^{k+d_e}{}'(i + d_a)$ correspond to the post-compression volume where d_a, d_l and d_e represents axial, lateral and elevational displacements respectively, and the size of the volume be $m \times n \times p$. The difference between the two signals, Δ, can be quantified using sum of absolute differences (SAD), which is computationally inexpensive to compute and has been shown to have good robustness against outliers [14]:

$$\Delta(i, j, k, d_a, d_l, d_e) = \left| g_j^k(i) - g_{j+d_l}^{f+d_e}{}'(i + d_a) \right| \tag{1}$$

where the axial, lateral and elevational search ranges are limited by $d_{a,min} \leq d_a \leq d_{a,max}$, $d_{l,min} \leq d_l \leq d_{l,max}$ and $d_{e,min} \leq d_e \leq d_{e,max}$.

$$R(d_{a_i}, d_{l_i}, d_{e_i}, d_{a_{i-1}}, d_{l_{i-1}}, d_{e_{i-1}}) = (d_{a_i} - d_{a_{i-1}})^2 + (d_{l_i} - d_{l_{i-1}})^2 + (d_{e_i} - d_{e_{i-1}})^2 \tag{2}$$

is the smoothness regularization. The cost function at each point i, j and k is

$$C_j^k(d_a, d_l, d_e, i) = \Delta(i, j, k, d_a, d_l, d_e) + w_1 R(d_a, d_l, d_e, d_a^{k-1}, d_l^{k-1}, d_e^{k-1}) \tag{3}$$

$$+ \min_{\delta_a, \delta_l, \delta_e} \left\{ \frac{C_j^k(\delta_a, \delta_l, \delta_e, i - 1) + C_{j-1}^k(\delta_a, \delta_l, \delta_e, i)}{2} + w_2 R(d_a, d_l, d_e, \delta_a, \delta_l, \delta_e) \right\}$$

where w_1 is a weight for governing smoothness in the elevational direction and w_2 is a weight for governing axial and lateral smoothness[1]. Generally, the optimum values of $\delta_a, \delta_l, \delta_e$ should be sought in the entire $[d_{a,min} \ d_{a,max}] \times [d_{l,min} \ d_{l,max}] \times [d_{e,min} \ d_{e,max}]$ space. However, since the strain value is low in elastography, it is expected and desired that at each sample of RF data, the change between the displacement of a sample and its previous sample is not more than 1. Therefore, the search range is limited to the nine values of $\{d_a - 1, \ d_a, \ d_a + 1\} \times \{d_l - 1, \ d_l, \ d_l + 1\} \times \{d_e - 1, \ d_e, \ d_e + 1\}$, which results in a significant gain in speed. This limit on the search range does not affect the results even in a high strain of 10%: Δd is zero for nine samples and one for the tenth sample on average. For memoization [12], $\delta_a, \ \delta_l$ and δ_e values that minimize the cost function are stored:

$$M_j^k(i, d_i, d_l, d_e) = \qquad (4)$$

$$\arg \min_{\delta_a, \delta_l, \delta_e} \left\{ \frac{C_j^k(\delta_a, \delta_l, \delta_e, i-1) + C_{j-1}^k(\delta_a, \delta_l, \delta_e, i)}{2} + w_2 R(d_a, d_l, d_e, \delta_a, \delta_l, \delta_e) \right\}$$

The cost function C_j^k is calculated for $i = 1 \cdots m$, $d_a = d_{a,min} \cdots d_{a,max}$, $d_l = d_{l,min} \cdots d_{l,max}$ and $d_e = d_{e,min} \cdots d_{e,max}$. The minimum cost at $i = m$ gives the displacement of this point, which is traced back to $i = 1$ using the M function to calculate the three axial, lateral and elevational displacements ($D = (d_a, d_l, d_e)$):

$$D_j^k(i) = \arg \min_{d_a, d_l, d_e} \left\{ C_j^k(d_a, d_l, d_e, i) \right\}, \ \ i = m$$

$$D_j^k(i) = M(i+1, D_j^k(i+1)), \ \ \ i = 1 \cdots m - 1 \qquad (5)$$

This gives all three displacements simultaneously, in contrast with other 3D elastography methods which give displacement in each direction in separate steps.

Further speed-up is achieved by downsampling the signal $g(i)$ in the axial direction by a factor of β to $g^*(i)$, and comparing it with the unaltered signal $g'(i)$. This is done by simply skipping $\beta - 1$ samples from $g(i)$ and performing DP on the βth sample as illustrated in Figure 1 left. This generates *integer displacement* estimations at m/β samples. The displacement of the skipped samples is then simply approximated by the linear interpolation of two neighboring points whose displacements are calculated, as an initial guess for the next step.

The displacement estimates are then refined to *subpixel displacement* estimation in the axial direction. The original signal $g(i)$ (not downsampled) is compared with $g'(i + d)$ upsampled by a factor of γ (Figure 1 right) in the axial

---

[1] The inclusion of the cost of the previous line ($C_{j-1}^k(\cdots)$) guarantees lateral smoothness. Instead, we could force the displacements of each pixel to be similar to the displacements of the neighboring pixel in the previous A-line, similar to what we did in the $w_1 R(\cdots)$ term to enforce elevational smoothness. The former is preferred since a wrong displacement estimation does not affect the neighboring A-line's displacement estimation. However, it requires the $C_{j-1}^k(\cdots)$ to be kept until the calculation of $C_j^k(\cdots)$ is completed. Therefore, at each time only two cost finctions are stored in the memory, making the memory requirement independent of the number of A-lines.
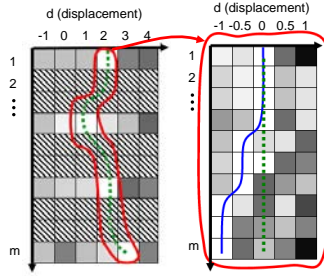
Fig. 1. In the left, the cost function C is shown when DP is performed on $g^*(i)$ ($g(i)$ downsampled by a factor of β) and $g'(i)$ (not downsampled). Hashed squares indicate no cost calculation is performed due to downsampling of $g(i)$, and white and black representing low and high cost values respectively. Displacement is calculated at m/β samples in this stage ($\beta = 3$ in this figure). In right, a new cost function around the optimum path of the first stage's cost function (the dashed line) is created, giving a $1/\gamma = 1/2$ pixel displacement accuracy at m samples.

direction using parabolic interpolation. Repeating the refinement procedure n times results in a refinement factor of $1/\gamma^n$. The code runs in approximately 30sec for a typical volume on a 3.8GHz P4 CPU.

In cross correlation methods, subsample displacement is usually achieved by interpolation of the correlation function, which is subject to bias and jitter [15]. Here we interpolate the original RF data instead, which is shown to have similar performance [15]. Although cosine-fit outperforms parabolic-fit interpolation in terms of bias and jitter [15], the latter is used here for computational simplicity.

3   Results

We first present *in-vivo* elastographic monitoring of RF ablation therapy of HCC in human during surgery using 2D DP elastography. RF ablation was administered using the RITA Model 1500X RF generator (Rita Medical Systems, Fremont, CA). Ultrasound RF data is acquired from an Antares Siemens system (Issaquah, WA) with a 7.27MHz linear array at a sampling rate of 40MHz. Figure 2 shows the B-mode scan, the strain image obtained using the DP method and CT scans performed after RF ablation (first and second row corresponding to first and second patient respectively). Tissue is simply compressed freehand with the ultrasound probe without any attachment. The shadow in Figure 2(a) at 20mm depth is produced by the thermal lesion. Note that it is not possible to ascertain the size and position of the thermal lesions from B-mode images. In addition, the thermal lesion has different appearances in the two B-scans. However, the thermal lesions show very well as hard lesions in both the strain images. The size of the thermal lesion in the strain images and in CT scans are also in accordance. The strain images provide with higher contrast of the thermal lesion and lower noise in the image, compared to the strain images of RF ablation
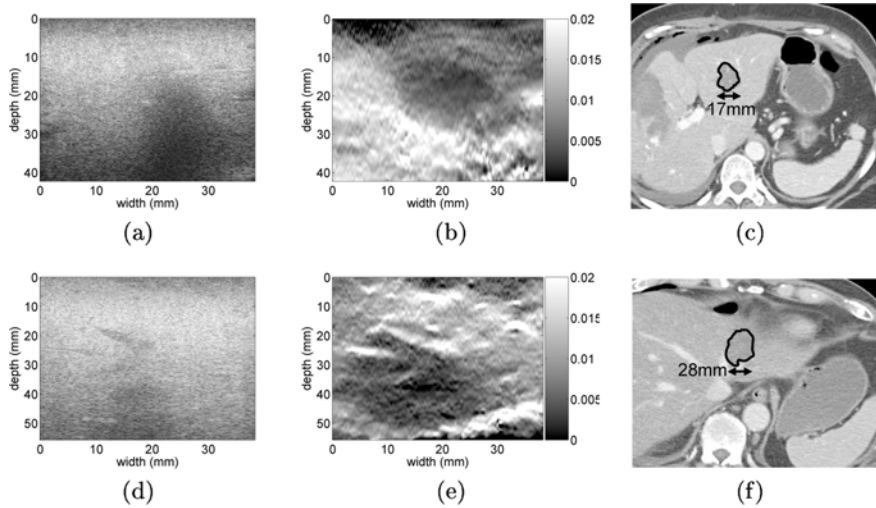
Fig. 2. *In-vivo* images of the thermal lesion produced by RF ablation therapy of HCC, first and second row corresponding to the first and second patients. (a) & (d) B-scan after RF ablation. The shadow in (a) indicates the presence of thermal lesion. It is almost impossible to ascertain the size and position of the thermal lesion from the B-scans. (b) & (e) Strain images after RFA ablation, generated using 2D DP elastography and freehand palpation of the liver tissue. The thermal lesion is visible in dark surrounded by normal tissue in white. (c) & (f) Post-ablation CT scans, with the delineated thermal lesions (The non-unity aspect ratio in the axes of the B-mode and strain images should be considered when comparing them with the CT scans).

reported in [3,8] which are obtained with cross-correlation. To the best of our knowledge, this is also the first demonstration of the success of elastography in imaging the thermal lesion in an *in-vivo* human experiment.

A Radionics device (Valleylab, Boulder, CO) is used for *ex-vivo* RF ablation. For 3D elastography, we use a 3D probe that consists of a curvilinear array that is mechanically rotated to scan a volume. Ultrasound RF data is acquired from an Ultrasonix system (Vancouver, BC) at 4.5MHz frequency, 20MHz sampling rate and 30% bandwidth. Figure 3 shows the experimental setup and results. Comparing strain images obtained during ablation and after ablation, the growth of the thermal lesion can be observed. There is also a good agreement between the size of the lesion in axial and lateral directions in the post-ablation strain images and gross pathology photograph. The ablation goes beyond the field of view of the 3D ultrasound probe in the elevational direction. The volumetric elastography contrast to noise ratio (CNR) [2] ($\text{CNR} = \sqrt{\frac{2(\bar{s}_b - \bar{s}_t)^2}{\sigma_b^2 + \sigma_t^2}}$ where $\bar{s}_t$ and $\bar{s}_b$ are the spatial strain average of the target and background and σ_t^2 and σ_b^2 are the spatial strain variance of the target and background) between two 3mm x 3mm x 3mm cubes, one in the thermal lesion and the other half way between the liver surface and the lesion, is 3.4. Note that due to the lateral and elevational
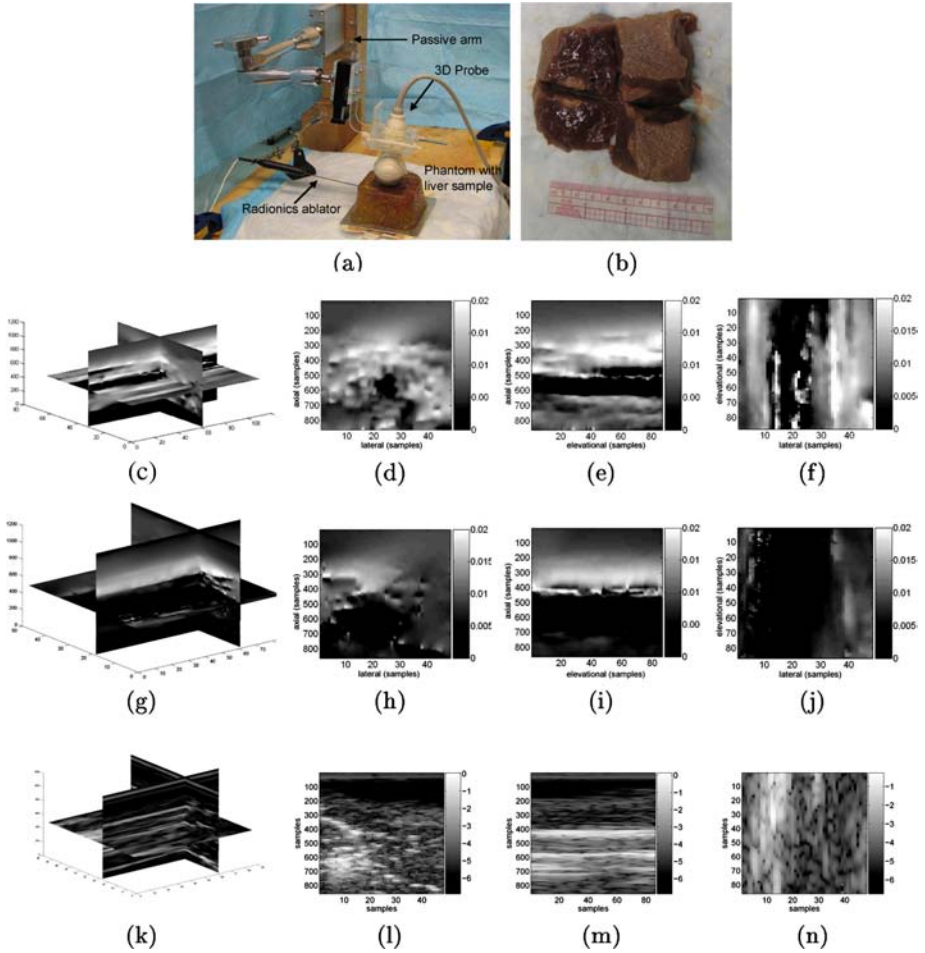
Fig. 3. *Ex-vivo* liver RF ablation experiment. The ablation power is set to 8W for 10 min and the cooler is turned off throughout the experiment. (a) The experimental setup. The passive arm is holding the 3D probe and the liver is contained in the gelatin phantom. (b) The liver sample after ablation (cut into four pieces) with the thermal lesion. (c)-(f) 3D strain images 6min after the start of the ablation (target temperature reached 90°C in 3min and was approximately constant in the next 7min of ablation). (g)-(j) 3D strain images after the ablation. (k)-(n) 3D B-mode images after the ablation. Each 650 axial samples correspond to 25mm in the strain and B-mode images. Each 40 lateral samples correspond to 16.6mm and 30.4mm on the top and bottom of each image (different values on the top and bottom since the probe is curved). Each 80 elevational samples correspond to 3.4mm and 6.3mm on the top and bottom of each image.

regularization, DP elastography is working reasonably in the presence of the ablation needle.

4   Discussion and Conclusion

Previous work has shown promise in monitoring ablation in 2D *ex-vivo* and animal experiments. In this paper, we present high quality *in-vivo* 2D strain images of thermal lesions and compared them to post-ablation CT data. Comparison is more qualitative, however, since strain images are 2D and CT data is 3D and ultrasound is not tracked. We also present formulation and experimental results of a 3D strain imaging system based on DP. In DP, we regularize the problem of 3D displacement estimation: regularization in 2D is shown to increase robustness [6]. As a result, no post processing step such as median filtering is performed.

   We demonstrate the feasibility of 3D elastography monitoring of RF ablation for the first time using a 3D probe; however, we are planning for a comprehensive comparison of the 3D DP with other 3D strain imaging techniques [10,11]. The lateral and elevational search is performed only to increase the quality of the axial strain: the lateral and elevational displacements are integer values and are not suitable for calculating strain. Good volumetric CNR between the thermal lesion and background suggests that the regularization is not adversely affecting CNR. However, a study similar to [6] on the effect of the 3D regularization on the CNR and resolution should be done. Having an elastography system for 3D ablation monitoring with promising *ex-vivo* results, *in-vivo* patient studies under our active Institutional Review Board (IRB) approval are to commence.

References

1. Rossi, S., Di-Stasi, M., Buscarini, E., et al.: Percutaneous RF interstitial thermal ablation in the treatment of hepatic cancer. AJR 167, 759–768 (1996)
2. Righetti, R., et al.: Elastographic characterization of hifu-induced lesions in canine livers. Ultras. Med. Biol. 25, 1099–1113 (1999)
3. Varghese, T., et al.: Elastographic imaging of thermal lesions in the liver in vivo following radiofrequency ablation: prelim results. US Med. Biol. 28, 1467–1473 (2002)
4. Varghese, T., et al.: Tradeoffs in elastographic imaging. US. Imag. 23, 216–248 (2001)
5. Xie, H., et al.: The role of local center frequency estimation in doppler-based strain imaging. In: IEEE Ultrasonics Symp., New York, NY, pp. 1965–1968 (2007)
6. Rivaz, H., Boctor, E., et al.: Ultrasound elastography: a dynamic programmimg approach. IEEE Trans. Medical Imaging (in press)
7. Krueger, M., et al.: Ultrasonic strain imaging of the female breast using phase root seeking and three-dimensional "optical flow". IEEE US Symp. 60, 1757–1760 (1998)
8. Liu, W., Zagzebski, J., Varghese, et al.: Segmentation of elastographic images using a coarse-to-fine active contour model. Ultrasound Med. Biol. 32, 397–408 (2006)
9. Lindop, J., et al.: 3D elastography using freehand ultrasound. Ultrasound Med. Biol. 32, 529–545 (2006)
10. Treece, G., et al.: Freehand elastog using a 3-D probe. US Med. Biol. (in press)
11. Fisher, T., et al.: Volumetric strain imaging. In: IEEE US Symp., pp. 355–358 (2007)

12. Bellman, R.: Applied dynamic programming. Princeton U. Press (1962)
13. Brown, M., et al.: Adv in computational stereo. IEEE PAMI 25, 993–1008 (2003)
14. Huber, P.: Robust statistics. John Wiley & Sons, Chichester (1981)
15. Viola, F., Walker, W.: A spline-based algorithm for continuous time-delay estima-
    tion using sampled data. IEEE Trans. Ultras. Ferr. Freq. Cont. 52, 80–93 (2005)

Novel Reconstruction and Feature Exploitation Techniques for Sensorless Freehand 3D Ultrasound

Hassan Rivaz[a], Hyun J. Kang[a], Philipp J. Stolka[a], Richard Zellars[b],
Frank Wacker[c], Gregory Hager[a] and Emad Boctor[c]

Department of [a]Computer Science, [b]Radiation Oncology, and [c]Radiology,
Johns Hopkins University

ABSTRACT

Out-of-plane motion in freehand 3D ultrasound can be estimated using the correlation of corresponding patches, leading to sensorless freehand 3D ultrasound systems. The correlation between two images is related to their distance by calibrating the ultrasound probe: the probe is moved with an accurate stage (or with a robot in this work) and images of a phantom are collected, such that the position of each image is known. Since parts of the calibration curve with higher derivative gives lower displacement estimation error, previous work limits displacement estimation to parts with maximum derivative. In this paper, we first propose a novel method for exploiting the entire calibration curve by using a maximum likelihood estimator (MLE). We then propose for the first time using constrains inside the image to enhance the accuracy of out-of-plane motion estimation. We specifically use continuity constraint of a needle to reduce the variance of the estimated out-of-plane motion. Simulation and real tissue experimental results are presented.

Keywords: 3D ultrasound, Speckle decorrelation, Fully developed speckle

1. INTRODUCTION

Most common techniques for acquiring 3D ultrasound data are oscillating head probes and freehand 3D ultrasound. In oscillating head probes, a 1D ultrasound transducer is automatically swept inside the probe, enabling 3D image acquisition. In freehand 3D ultrasound, a position sensor is attached to an ordinary probe which is swept over the desire region by the clinician.

Freehand 3D ultrasound is inexpensive, works with the existing 2D probes, and allows arbitrary 3D volume acquisition. However, the need for the additional sensor makes it difficult to use. Sensorless volume reconstruction of freehand 3D ultrasound is possible using the information in the images themselves: out of plane motion estimation can be obtained from image correlation,[1] which is the focus of this work, while in plane motion can be estimated through image registration[2–4] or by using techniques similar to elastography.[5–7]

The granular appearance of ultrasound images is the key factor in out-of-plane motion estimation (Figure 1). Each pixel in an ultrasound image is formed by the back-scattered echoes from an approximately ellipsoidal region called the resolution cell.[8] The interference of scatterers in a resolution cell creates the granular appearance of the ultrasound image, called speckle. Although of random appearance, speckle pattern is identical if the same object is scanned from the same direction and under the same focusing and frequency. Speckle characterization is essential in many areas of quantitative ultrasound. In this work, it is a prerequisite for speckle-based distance

estimation. We use low order moments to discriminate fully developed speckle (FDS) patches versus coherent speckle patches.[9]

$$R = \text{SNR} = \frac{\langle A^{v_r} \rangle}{\sqrt{\langle A^{2v_r} \rangle - \langle A^{v_r} \rangle^2}} \tag{1}$$

$$S = \text{skewness} = \frac{\langle (A^{v_s} - \langle A^{v_s} \rangle)^3 \rangle}{(\langle A^{2v_s} \rangle - \langle A^{v_s} \rangle^2)^{\frac{3}{2}}} \tag{2}$$

where A is the amplitude of the ultrasound RF envelope in the analysis patch, v_r and v_s are the signal powers and $\langle \cdots \rangle$ denotes the mean. Here we use[10] $v_r = 2v_s = 1$. An elliptical discrimination function is calculated in the R-S plane by performing principal component analysis (PCA) on the data from simulated FDS patches.[10] A patch is then classified as FDS if its R-S duple falls inside this ellipse.

Having found FDS patches in two ultrasound images, the correlation between them is used for estimating the distance between the two images.[11] The R-S metric requires approximately 3500 pixels per patch (depending on the correlation of data[12]), but such large patches (which are rectangles) of FDS are unlikely to be found in real tissue because of its inhomogeneity.[11] Gee et al.[13] proposed a heuristic technique that is robust to the lack of FDS patches in the ultrasound image. This method allows the calculation of the elevational distance for all patches of the image, regardless of their level of coherency, by measuring the axial and lateral correlation of each patch. Since the behavior of coherent reflectors in the elevational direction can be different from their behavior in the axial and lateral directions, the performance of the method can decline depending on the level of anisotropy of the tissue.

In,[14] we proposed a fast algorithm to find irregularly shaped FDS patches and showed that this algorithm finds significantly more FDS patches. Here, we use beam steering as another technique to increase the number of FDS patches found in the image.[15] This is achieved by obtaining more data from a certain region of tissue, hence reducing the size of the analysis patch. Having found such small FDS patches, we further use the steered images for better out-of-plane (elevational) motion estimation.

Coherent scattering causes the elevational distance measurement from the conventional correlation algorithms to be underestimated.[11] Thus, distance measurement is limited to the patches of the ultrasound image that contain only FDS.[11] To completely determine the out-of-plane degrees of freedom between two planes, at least three non-collinear pairs of such patches are required.[4]
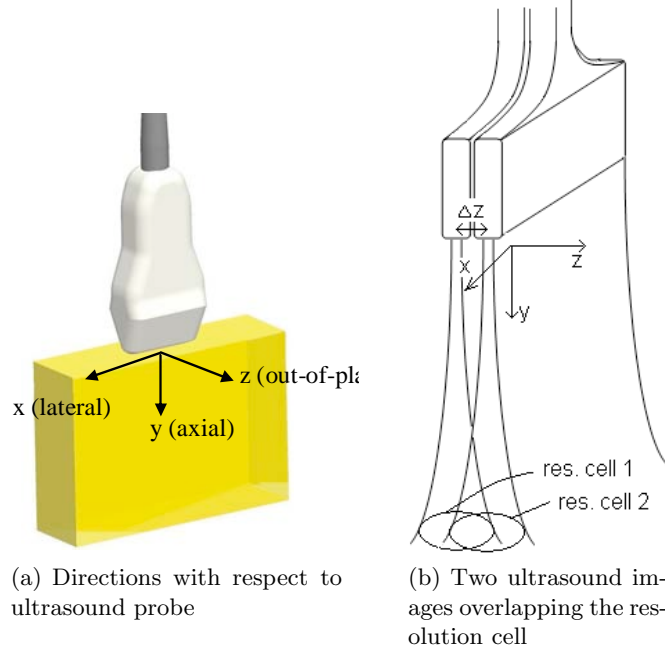
Since FDS patches are extremely rare in real tissue, these methods usually have a low accuracy and are only relevant in limited tissue types. Gee et al.[13] proposed a heuristic technique that is robust to the lack of FDS patches in the ultrasound image. This method allows the calculation of the elevational distance for all patches of the image, regardless of their level of coherency, by measuring the axial and lateral correlation of each patch. Since the behavior of coherent reflectors in the elevational direction can be different from their behavior in the axial and lateral directions, the performance of the method can decline depending on the level of anisotropy of the tissue. The purpose of this work is to devise a method applicable to a various tissue types that accurately reconstructs 3D volumes from ultrasound images.

Recently, Laporte and Arbel[16, 17] have proposed probabilistic fusion of noisy out-of-plane motion estimation. This work is most similar to these works, in that it calculates the maximum likelihood estimate (MLE) of the out-of-plane motion. We also use beam steering to obtain more data and increase the accuracy of the out of plane motion estimation similar to.[15]

2. METHODS

2.1. Combining Steered Images

We are looking for rectangular FDS patches using images acquired from the same location at different steering angles. The key idea is to combine data acquired from a certain region at different steering angles and therefore reducing the size of the analysis patch. Figure 2 shows two images acquired at 0 and θ steering angles. A

(a) Directions with respect to ultrasound probe

(b) Two ultrasound images overlapping the resolution cell

Figure 1. (a) shows the three directions relative to the ultrasound probe. Out-of-plane direction and elevational direction are used interchangably in this work. (b) shows aquisition of two ultrasound images at a distance of Δz. Ultrasound beam is in order of a millimeter wide. This wideness affects the resolution of ultrasound image in the lateral, y, and elevational, z, directions, as well as creating a granular pattern, called speckle. The size of the resolution cell in the axial direction, x, is determined by the wavelength of the ultrasound wave and is magnified in this image.

rectangle patch in the left image is warped into a parallelogram and is shifted in the steered right image. The position of the parallelogram can be simply found as a function of θ, x and y. Therefore, samples n_X and n_Y from the steered image correspond to samples n_x and n_y from the non-steered image and

$$
\begin{aligned}
n_X &= n_x - \frac{v_{US}}{2\nu} \cdot \frac{n}{w} \cdot \sin(\theta) \cdot n_y \\
n_Y &= \frac{n_y}{\cos(\theta)}
\end{aligned}
\tag{3}
$$

where $v_{US} = 1540000$mm/s is the speed of ultrasound in tissue, ν is the sampling frequency of the ultrasound machine, n is the total number of the A-lines and w is the width of image in mm. To find the correspondence of a patch, the correspondent of its four corners are found using these equations and applying nearest neighbor interpolation. The parallelogram connecting these four corners is the correspondent of the patch.

2.2. Maximum Likelihood Motion Estimation

Assume we have two parallel ultrasound images with ground truth out-of-plane distance z (Figure 1), and that we have measured correlation coefficients ρ_i for $i = 1 \cdots n$ patches between the two images (Figure 3). The goal is to find μ_z which is maximum likelihood estimate of z given all the ρ_i measurements. Let $\rho_i = f_i(z_i)$ be the calibration function that relates the out-of-plane motion z_i to correlation coefficient ρ_i for patch i (each patch has a different calibration function depending on its depth, see Figure 6). Assuming that ρ_i is drawn from a Gaussian distribution with mean $f(\mu_z)$ and variance σ_i, the conditional probability of ρ_i is

$$
\Pr(\rho_i \mid \mu_z, \sigma_i^2) = \frac{1}{(2\pi\sigma_i^2)^{1/2}} \ e^{-\frac{(\rho_i - f_i(\mu_z))^2}{2\sigma_i^2}}
\tag{4}
$$
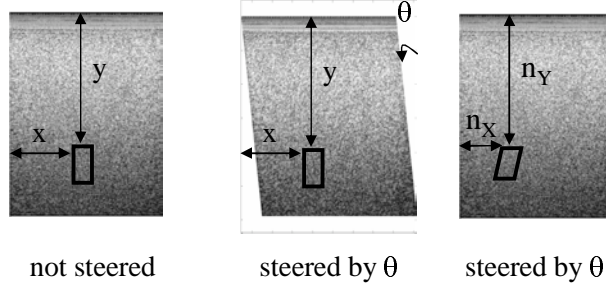
Figure 2. Corresponding patches in images acquired with different steering angles. In the left, a patch is shown in the not-steered image. In the middle, the patch which corresponds to the same tissue is shown in the scan-converted steered image. In the right, the patch is shown in the raw steered image (not scan-converted).
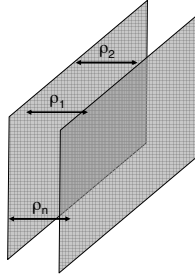
Figure 3. The correlation coefficient ρ_i is calculated between n patches of the two images.

We assume that ρ_i measurements are independent. Therefore, the conditional probability of observing all the ρ_i values will be simply their multiplication. Looking at the product as a function of μ and σ_i and taking its logarithm to convert multiplication to summation, we have the familiar log-likelihood equation

$$L(\vec{\rho}\,|\,\mu_z,\vec{\sigma^2}) = -\Sigma_{i=1}^{n}\left[\frac{1}{2}\log\sigma_i^2 + \frac{(\rho_i - f_i(\mu_z))^2}{\sigma_i^2}\right] + \frac{n}{2}\log(2\pi) \tag{5}$$

where $\vec{\rho}$ and $\vec{\sigma^2}$ are two vectors containing all the ρ_i and σ_i^2 measurements. In the above equation, ρ_i is the correlation of two corresponding patches and is known. σ_i^2 is also known: it is the variance of the correlation and is calculated in the calibration process (Figure 6). To find the ML estimate of the μ_z, we differentiate this equation with respect to μ_z and set it to zero, arriving at

$$\Sigma_{i=1}^{n}\frac{f_i'(\mu_z)(\rho_i - f_i(\mu_z))}{\sigma_i^2} = 0 \tag{6}$$

where f' denotes derivative of f. Unfortunately this equation is not easy to solve for μ_z. Instead, lets transform ρ_i to z_i and write the log-likelihood functions in terms of z_i's. Equation 5 becomes

$$L(\vec{z}\,|\,\mu_z,\vec{\sigma_z^2}) = -\Sigma_{i=1}^{n}\left[\frac{1}{2}\log\sigma_{zi}^2 + \frac{(z_i - \mu_z)^2}{\sigma_{zi}^2}\right] + \frac{n}{2}\log(2\pi) \tag{7}$$

where $\sigma_{zi}^2 = \frac{\sigma_i^2}{f'(\rho_i)^2}$ is the transformed variance in the ρ domain (σ_i) to the z domain (σ_{zi}). Differentiating with respect to μ_z and setting it to zero gives

$$\Sigma_{i=1}^{n}\frac{z_i - \mu_z}{\sigma_{zi}^2} = 0 \tag{8}$$

which can be easily solved to give

$$\mu_z = \frac{\sum_{i=1}^{n} \frac{z_i}{\sigma_{zi}^2}}{\sum_{i=1}^{n} \frac{1}{\sigma_{zi}^2}} \tag{9}$$

Finally, we utilize constraints in the images to enhance out-of-plane motion estimation. Many surgical procedures such as biopsy, drug delivery and brachytherapy involve inserting a needle into the tissue. The prior of needle continuity can be used to decrease the variance of the measured out of plane motion (we are assuming that the needle crosses US image plane and is not parallel to the image). Assume that the tip of the needle can be measured at each image with a variance of $[\sigma_{needle}^*]^2$, and that the angle of the needle with the normal of the ultrasound image (i.e the angle between the needle and the axes y in Figure 1) is α. Also, let $\sigma_{cor.}^2$ denote the variance of the out-of-plane motion estimation using the correlation method and $\sigma_{needle} = \sigma_{needle}^*/\tan(\alpha)$. Assuming both noises are Gaussian, variance of the final estimate which combines the two estimates is $\frac{\sigma_{needle}^2 \sigma_{cor.}^2}{\sigma_{needle}^2 + \sigma_{cor.}^2}$. It can be easily shown that this quantity is less than both σ_{needle}^2 and $\sigma_{cor.}^2$, meaning that the resulting variance is less than both initial variances.

2.3. Calibration and Data Acquisition

The system operates in two distinct modes - calibration mode and image-based 3DUS reconstruction mode (Figure 4). Both will be described from a process flow perspective. In the calibration mode, information necessary to calibrate the distance estimations is collected (Figure 4). To this end, the robot control component steps the robot through a series of precisely defined positions and triggers the acquisition of a single US frame (RF data) at each position from a homogeneous fully developed speckle (FDS) phantom. These frames are associated with their respective coordinates and stored for offline use. Then, the software system reads the batch of frames and positions and subdivides the frames into distinct subpatches. Pairs of patches from the same location originating from frames at different distances are correlated, thus creating a set of (strictly monotonous) calibration (or decorrelation) curves x,y(d). These curves depend on the characteristics of the selected probe, the imaging frequency, and the image location x, y (in particular the depth y) of the respective patches. Currently, the offline calibration process takes 2-3 minutes including scan time to generate the needed calibration curves (decorrelation curves). Before this recent development, manual data collection and offline processing using MATLAB scripts used to take many hours of effort.
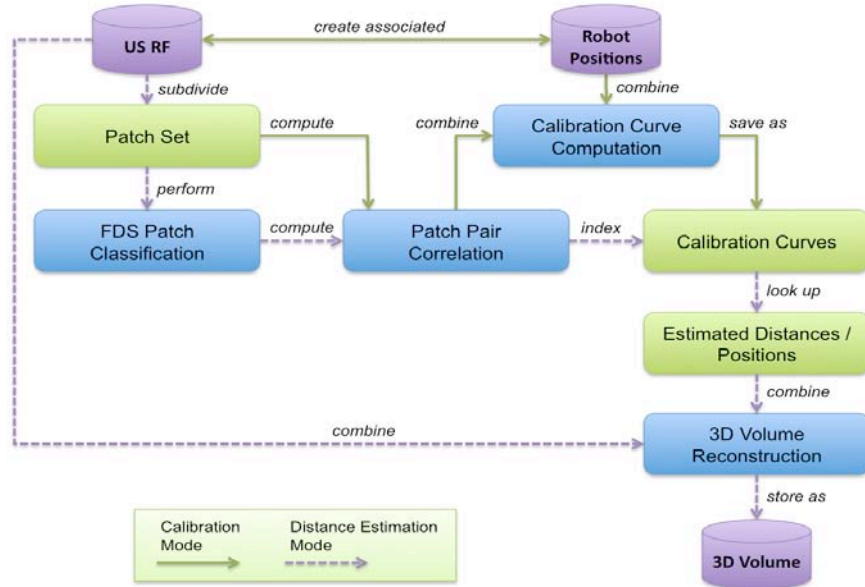
Figure 4. The data acquisition and calibration system (some of the blocks are the subject of future work).

(a) Calibration experiment

(b) Out-of-plane motion estimation using real tissue
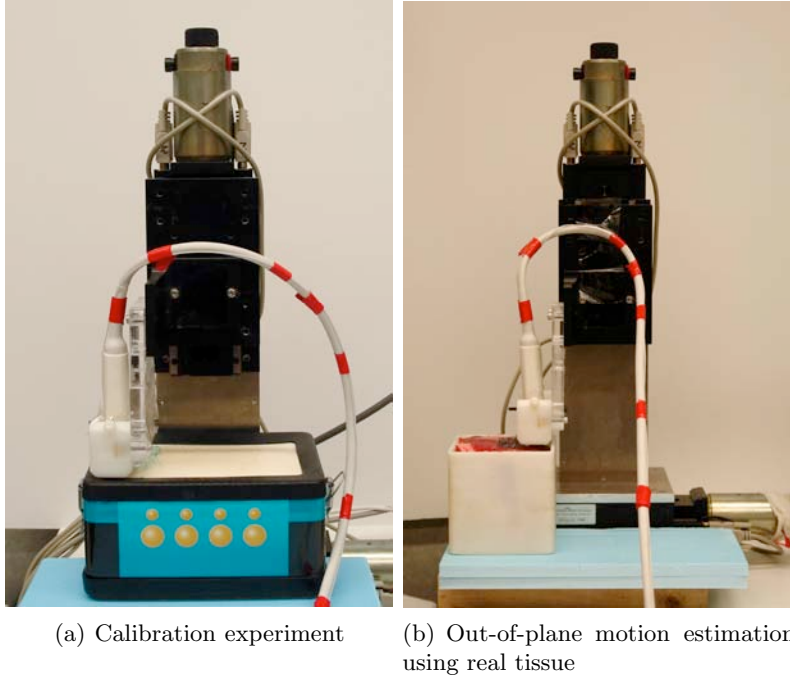
Figure 5. The experimental setup for moving the probe out-of-plane and acquiring ultrasound images. In (a), the robot moves the probe in the out-of-plane direction while the ultrasound is imaging a FDS phantom to generate the calibration curves. In (b), the robot is moving the probe while the ultrasound is imaging real tissue, so that the speckle correlation results can be compared to ground truth (i.e. robot readings).

3. EXPERIMENTAL SETUP

The ultrasound RF data was sampled with a robot-based system in order to achieve reliable, high-accuracy ground truth readings for the displacements. This will give us the images we need for calibration and also the gives us the ground truth when we reconstruct the volume. This process yielded a series of planar-parallel RF slices through the respective phantom, in a fashion somewhat comparable to a freehand sweep. The phantoms were positioned within the workspace of a high-precision three degrees-of-freedom (DoF) cartesian robot stage (DMC-21x3 with three servo motor stages, by Galil Motion Control; relative accuracy better 0.005 mm). For calibration, the stage translated the probe to new positions every $\Delta x = 0.05$ mm apart, then triggered RF slice acquisition via a TTL signal connected to the ultrasound machine's ECG trigger port, where the data was written to file. For calibration data acquisition, a FDS phantom is imaged. For volume reconstruction, real tissue (beef steak) is used. Figure 5 shows the experimental setup.

An Ultrasonix ultrasound machine (Burnaby, BC) with a sampling frequency of $\nu = 20$MHz is used to acquire RF data. To calibrate the rate of image decorrelation with out-of-plane motion, RF data of 5x80 parallel frames were acquired from a FDS phantom at an elevational distance of 0.05 mm between consecutive images: five frames at each location with steering angles of -5, -2.5, 0, 2.5 and 5.5 degrees. The experimental setup is shown in Figure 5: the probe is moved with a micrometer with the accuracy of .005 mm. Calibration results showed that the decorrelation rate is not affected by beam steering.

Out-of-plane motion estimation was performed on ex-vivo beef steak tissue. 4x80 RF frames at an elevational distance of 0.05 mm between consecutive frames were acquired using the setup shown in Figure 5: four images at each location with $-5°$, $-2.5°$, $0°$, $2.5°$ and $5°$ steering angles.
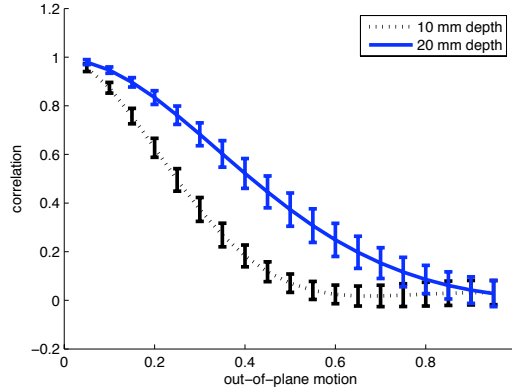
Figure 6. Two calibration curves at depths of 10 mm and 20 mm and their variances. Note that the calibration curve at the deeper location drop slower with the out-of-plane motion.
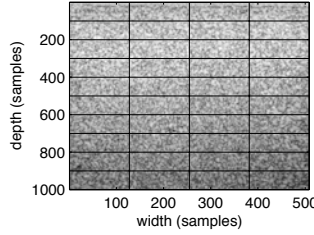
Figure 7. Subdivision of an image of the FDS phantom into patches is shown.

4. OUT-OF-PLANE MOTION ESTIMATION

The correlations are calculated using Pearsons linear correlation coefficient ρ

$$\rho(W, Z) = \frac{\Sigma w_i z_i - N \mu_w \mu_z}{\sqrt{\left(\Sigma w_i^2 - N \mu_w^2\right)\left(\Sigma z_i^2 - N \mu_z^2\right)}} \tag{10}$$

where w_i and z_i, $i = 1 \cdots N$, are the intensity values of each pixel in patches W and Z, N is the total number of pixels and μ_w and μ_y are the means of the intensity values of patches W and Z respectively.

Patches that are closest to being FDS are selected as described in.[15] Figure 8 shows the results of reconstructing out-of-plane motion using the correlation values. (a) and (b) are obtained by combining the two images with $\pm 2.5°$ steering angle at each location, while (c) and (d) are obtained by combining the two images with $\pm 5°$ steering angle at each location. The results show that using the MLE method slightly reduces both the underestimation error and the variance of the out-of-plane measurements. IN addition, it can be seen from (b) and (d) that the needle constraint reduces the variance in the measurements.

5. DISCUSSION AND CONCLUSION

Out-of-plane motion estimation is only studied here for a fixed distance between two frames, 0.4mm. A study of accuracy as the distance varies gives insight for optimum frame selection.[18, 19] In freehand experiments the images are not parallel as they are in our experiments, and therefore the rotations between the images need to be found.[11, 13, 20] We showed before[15] that performing beam steering significantly increases the accuracy of out-of-plane motion estimation. In this work, we showed that MLE can also be used to enhance the out-of-plane motion estimation.
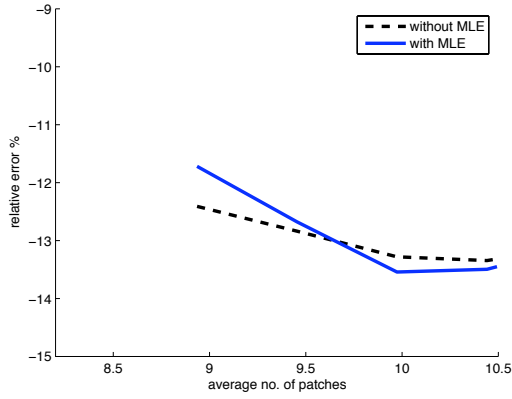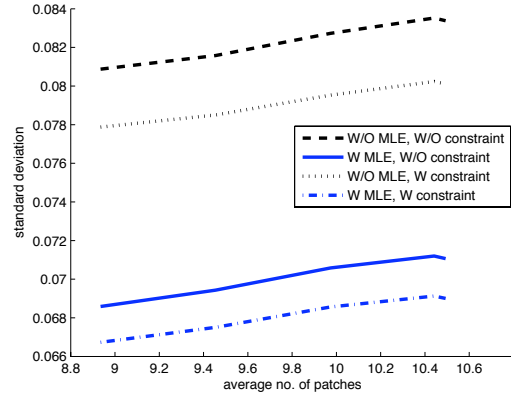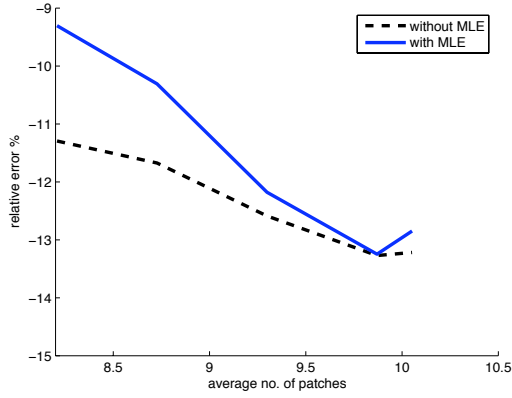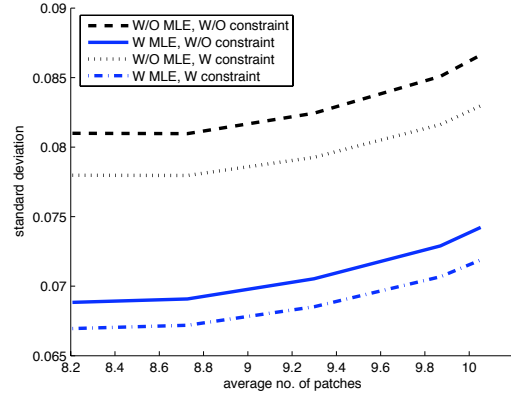
Figure 8. relative error and standard deviation of the sensorless measurements. (a) The relative error. Reconstruction is performed using two steered images at $\pm2.5°$. (b) The standard deviation of the measurements. W/O MLE refers to without MLE, W/O constraint refers to without utilizing the needle continuity constraint, and W MLE refers to with MLE. (c) and (d) are corresponding errors and variances with two steered images at $\pm5°$.

Acknowledgment

REFERENCES

1. J. Chen, B. Fowlkes, P. Carson, and J. Rubin, "Determination of scan-plane motion using speckle decorrelation: theoretical considerations and initial test," *Imag. Sys. and Tech.* **8**, pp. 38–44, 1997.

2. G. Treece, R. Prager, A. Gee, C. Cash, and L. Berman, "Correction of probe pressure artifacts in freehand 3D ultrasound," *Medical Image Analysis* **6**, pp. 199–215, 2002.

3. B. Geiman, L. Bohs, M. Anderson, S. Breit, and G. Trahey, "A novel interpolation strategy for estimating subsample speckle motion," *Pattern Recog. Letters* **45**, pp. 1541–1552, 2000.

4. R. Prager, A. Gee, G. Treece, C. Cash, and L. Berman, "Sensorless freehand 3-d ultrasound using regression of the echo intensity," *Ultrasound Med. Biol.* **29**, pp. 437–446, 2003.

5. H. Rivaz, E. Boctor, P. Foroughi, G. Fichtinger, and G. Hager, "Ultrasound elastography: a dynamic programming approach," *IEEE Trans Med Imaging* **27**, pp. 1373–1377, Oct. 2008.

6. H. Rivaz, I. Fleming, L. Assumpcao, G. Fichtinger, U. Hamper, M. Choti, G. Hager, and E. Boctor, "Ablation monitoring with elastography: 2d in-vivo and 3d ex-vivo studies," *Medical Image Computing & Computer Assisted Interventions, MICCAI, New York, NY* , pp. 458–466, Sept. 2008.

7. H. Rivaz, P. Foroughi, I. Fleming, R. Zellars, E. Boctor, and G. Hager, "Tracked regularized ultrasound elastography for targeting breast radiotherapy," *Medical Image Computing & Computer Assisted Interventions, MICCAI, London, UK* , pp. 507–515, Sept. 2009.

8. R. Wagner, S. Smith, J. Sandrik, and H. Lopez, "Statistics of Speckle in Ultrasound B-Scans," *IEEE Trans. Sonics and Ultrasonics* **17**(3), pp. 251–268, 1983.

9. R. Prager, A. Gee, G. Treece, and L. Berman, "Analysis of speckle in ultrasound images using fractional order statistics and the homodyned k-distribution," *Ultrasonics* **40**, pp. 133–137, 2002.

10. H. Rivaz, E. Boctor, and G. Fichtinger, "Ultrasound speckle detection using low order moments," *IEEE Int. Ultrasonics Symp.* , pp. 2092–2095, Oct. 2006.

11. P. Hassenpflug, R. Prager, G. Treece, and A. Gee, "Speckle classification for sensorless freehand 3-d ultrasound," *Ultrasound Med. Biol.* **31**, pp. 1499–1508, Nov. 2005.

12. V. Dutt and J. Greanleaf, "Speckle analysis using signal to noise ratios based on fractional order moments," *Ultrasonic Imag.* **17**, pp. 251–268, 1995.

13. A. Gee, R. Houdson, P. Hassenpflug, G. Treece, and R. Prager, "Sensorless freehand 3d ultrasound in real tissue: Speckle decorrelation without fully developed speckle," *Medical Image Analysis* **10**, p. 137:149, Apr. 2006.

14. H. Rivaz, E. Boctor, and G. Fichtinger, "A robust meshing and calibration approach for sensorless freehand 3d ultrasound," *Proc. SPIE Medical Imaging* **6583**, pp. 181–188, Feb. 2007.

15. H. Rivaz, R. Zellars, G. Hager, G. Fichtinger, and E. Boctor, "Beam steering approach for speckle characterization and out-of-plane motion estimation in real tissue," *IEEE Int. Ultrasonics Symp.* , pp. 781–784, Oct. 2007.

16. C. Laporte and T. Arbel, "Combinatorial and probabilistic fusion of noisy correlation measurements for untracked freehand 3-d ultrasound," *IEEE Trans Med Imaging* **27**, pp. 984–994, Jul. 2008.

17. C. Laporte, J. Clark, and T. Arbel, "Generalized poisson 3-d scatterer distributions," *IEEE Trans. Ultrason. Ferroelectr. Freq. Control* **56**, pp. 410–414, Feb. 2009.

18. W. Smith and A. Fenster, "Optimum scan spacing for three-dimensional ultrasound by speckle statistics," *Ultrasound Med. Biol.* **26**, pp. 551–562, May 2000.

19. W. Smith and A. Fenster, "Analysis of an image-based transducer tracking system for 3d ultrasound," *Proceedings of SPIE - The International Society for Optical Engineering* **5035**, pp. 154–165, 2003.

20. J. Housden, A. Gee, R. Prager, and G. Treece, "Rotational motion in sensorless freehand 3D ultrasound," *Univ. of Cambridge Tech. Rep.* , Oct. 2007.

Tracked Regularized Ultrasound Elastography for Targeting Breast Radiotherapy

Hassan Rivaz, Pezhman Foroughi, Ioana Fleming, Richard Zellars, Emad Boctor, and Gregory Hager

Johns Hopkins University, Baltimore, MD, USA

Abstract. Tracked ultrasound elastography can be used for guidance in partial breast radiotherapy by visualizing the hard scar tissue around the lumpectomy cavity. For clinical success, the elastography method needs to be robust to the sources of decorrelation between ultrasound images, specifically fluid motions inside the cavity, change of the appearance of speckles caused by compression or physiologic motions, and out-of-plane motion of the probe. In this paper, we present a novel elastography technique that is based on analytic minimization of a regularized cost function. The cost function incorporates similarity of RF data intensity and displacement continuity, making the method robust to small decorrelations present throughout the image. We also exploit techniques from robust statistics to make the method resistant to large decorrelations caused by sources such as fluid motion. The analytic displacement estimation works in real-time. Moreover, the tracked data, used for targeting the radiotherapy, is exploited for discarding frames with excessive out-of-plane motion. Simulation, phantom and patient results are presented.

1 Introduction

Breast irradiation after lumpectomy significantly reduces the risk of cancer recurrence. There is growing evidence suggesting that irradiation of only the involved area of the breast, partial breast irradiation (PBI), is as effective as whole breast irradiation [1]. Benefits of PBI include significantly shortened treatment time and fewer side effects as less tissue is treated. However, these benefits cannot be realized without localization of the lumpectomy cavity. Tracked ultrasound elastography can be used for localizing the lumpectomy cavity in the treatment room, minimizing tissue motion from planning to treatment.

This paper is focused on freehand palpation elastography, which involves estimating the displacement field of the tissue undergoing slow compression. Most elastography techniques estimate the displacement field using local cross correlation analysis of echoes [2,3,4]. These methods are very sensitive and accurate for calculating small displacements. However, elastography is subject to speckle decorrelation caused by various sources such as motion of subresolution scatterers, out-of-plane motion, high compression and complex fluid motions.

The prior of tissue deformation continuity can be used to make elastography more robust to signal decorrelation. Previous work on regularized elastography

is computationally expensive [5,6]. Dynamic programming (DP) can be used to speed the optimization procedure [7], but it only gives integer displacements. Subpixel displacement estimation is possible [7], but it is computationally expensive if a fine subpixel level is desired. In addition, a fixed regularization weight is applied throughout the image. However, while two ultrasound images may correlate well in most parts, they can have small correlation in specific parts. Four examples of low correlation are: (1) correlation decreases with depth mainly due to a decrease in the ultrasonic signal to noise ratio, (2) correlation is low close to arteries due to complex motion and inside vessels due to blood motion, (3) correlation is extremely low in lesions that contain liquid due to the incoherent fluid motion [8,3], and (4) out-of-plane motion of movable structures within the image [8] causes low local correlation. To prevent such regions from introducing errors in the displacement estimation one should use large weights for the regularization term, resulting in over-smoothing.

Freehand palpation elastography provides ease-of-use and requires minimum additional cost. However, out-of-plane motion cannot be avoided in freehand palpation, which reduces the quality of any elastography method. Assisted freehand elastography [9] significantly reduces the out-of-plane motion but it requires addition of a device to the probe. Quality metrics such as persistence in strain images have also been developed to address this problem [10]. To measure the persistence, elastography is performed on two pairs of images and the resulting strain images are correlated. This method requires strain images for calculating the quality metric. Therefore, trying all the combinations in a series of frames to find the best pair for elastography will be computationally expensive.

In this paper, we present a novel elastography method based on analytic minimization (AM) of a cost function that incorporates similarity of echo amplitudes and displacement continuity. We introduce a novel regularization term and demonstrate that it minimizes displacement underestimation caused by smoothness constraint. We also introduce the use of robust statistics implemented via iterated reweighted least squares (IRLS) to treat uncorrelated ultrasound data as outliers. And finally, we use the tracking information to select the best pairs of frames for elastography. Simulation, phantom and patient experiments are presented for validation.

2   Regularized Displacement Estimation

Dynamic Programming (DP). DP is a discrete efficient optimization technique for causal systems. In DP elastography [7], a cost function is defined as

$$C(i, d_i) = \min_{d_{i-1}} \{ C(i-1, d_{i-1}) + \alpha_a R(d_i, d_{i-1}) \} + |I_1(i) - I_2(i + d_i)| , \ i = 2 \cdots m$$

(1)

where d_i is the displacement of sample i, $R(d_i, d_{i-1}) = (d_i - d_{i-1})^2$ is an axial regularization term (axial, lateral and out-of-plane directions are respectively z, x and y in Figure 2 (a)), α_a is a weight for the regularization, I_1 and I_2 are corresponding RF-lines of before and after deformation and m is the length

of RF-lines. The cost function is minimized at $i = m$ and the d_i values that have minimized the cost function are traced back to $i = 1$, giving the d_i for all samples. We have implemented a 2D DP algorithm similar to [7] to generate integer displacements as a starting point for the next step of our algorithm.

Analytic Minimization (AM). We now propose a method that analytically minimizes a regularized cost function and gives the refined displacement field. Only axial displacements will be refined for strain calculation.

Having the integer displacements d_i from DP, it is desired to find Δd_i values such that $d_i + \Delta d_i$ gives the value of the displacement at the sample i for $i = 1 \cdots m$. Such Δd_i values will minimize the following regularized cost function

$$C\left(\Delta d_1, \cdots, \Delta d_m\right) = \Sigma_{i=1}^{m} \left[I_1(i) - I_2(i + d_i + \Delta d_i)\right]^2 +$$
$$\alpha_a(d_i + \Delta d_i - d_{i-1} - \Delta d_{i-1})^2 + \alpha_l(d_i + \Delta d_i - d_i^{p\cdot} - \Delta d_i^{p\cdot})^2 \qquad (2)$$

where superscript $p.$ refers to the previous RF-line (adjacent RF-line in the lateral direction) and α_l is a weight for lateral regularization. Substituting $I_2(i + d_i + \Delta d_i)$ with its first order Taylor expansion approximation around d_i, we have

$$C\left(\Delta d_1, \cdots, \Delta d_m\right) = \Sigma_{i=1}^{m} \left[I_1(i) - I_2(i + d_i) - I_2'(i + d_i)\Delta d_i\right]^2 +$$
$$\alpha_a(d_i + \Delta d_i - d_{i-1} - \Delta d_{i-1})^2 + \alpha_l(d_i + \Delta d_i - d_i^{p\cdot} - \Delta d_i^{p\cdot})^2 \qquad (3)$$

where I_2' is the derivative of the I_2. The optimal Δd_i values occur when the partial derivative of C w.r.t. Δd_i is zero. Setting $\frac{\partial C}{\partial \Delta d_i} = 0$ we have

$$(\mathbf{I_2'}^2 + \alpha_a\mathbf{D} + \alpha_l\hat{\mathbf{I}})\Delta\mathbf{d} = \mathbf{I_2'}\mathbf{e} - (\alpha_a\mathbf{D} + \alpha_l\hat{\mathbf{I}})\mathbf{d} + \alpha_l\mathbf{d}^{t.p.}, \quad \mathbf{D} = \begin{bmatrix} 1 & -1 & 0 & \cdots & 0 \\ -1 & 2 & -1 & \cdots & 0 \\ \vdots & & & \ddots & \\ 0 & \cdots & 0 & -1 & 1 \end{bmatrix}$$
$$(4)$$

where $\mathbf{I_2'} = diag(I_2'(1+d_1) \cdots I_2'(m+d_m))$, $\Delta\mathbf{d} = [\Delta d_1 \cdots \Delta d_m]^T$, $\mathbf{e} = [e_1 \cdots e_m]^T$, $e_i = I_1(i) - I_2(i + d_i)$, $\mathbf{d} = [d_1 \cdots d_m]^T$, $\mathbf{d}^{t.p.} = \mathbf{d}^p + \Delta\mathbf{d}^{p\cdot}$ is the vector of total displacement of the previous line and $\hat{\mathbf{I}}$ is the identity matrix. $\mathbf{I_2'}$, $\mathbf{D}$ and $\hat{\mathbf{I}}$ are matrices of size $m \times m$ and $\Delta\mathbf{d}$, $\mathbf{r}$, $\mathbf{d}$ and $\mathbf{d}^{t.p.}$ are vectors of size m.

Biasing the Regularization. The regularization term $\alpha_a(d_i + \Delta d_i - d_{i-1} - \Delta d_{i-1})^2$ penalizes the difference between $d_i + \Delta d_i$ and $d_{i-1} + \Delta d_{i-1}$, and therefore can result in underestimation of the displacement field. Such underestimation can be prevented by biasing the regularization by ϵ to $\alpha_a(d_i + \Delta d_i - d_{i-1} - \Delta d_{i-1} - \epsilon)^2$, where $\epsilon = (d_m - d_1)/(m-1)$ is the average displacement difference between samples i and $i-1$. An accurate enough estimate of $d_m - d_1$ is known from the previous line. With the bias term, the R.H.S. of Equation 4 becomes $\mathbf{I_2'}\mathbf{e} - (\alpha_a\mathbf{D} + \alpha_l\hat{\mathbf{I}})\mathbf{d} + \alpha_l\mathbf{d}^{t.p.} + \mathbf{b}$ where the bias term is $\mathbf{b} = \alpha_a[-\epsilon \ \ 0 \cdots 0 \ \ \epsilon]^T$ and all other terms are as before. Interestingly, except for the first and the last equation in this system, all other $m - 2$ equations are same as Equation 4.

Equation 4 can be solved for $\Delta\mathbf{d}$ in $4m$ operations since the coefficient matrix $\mathbf{I_2'}^2 + \alpha_a\mathbf{D} + \alpha_l\hat{\mathbf{I}}$ is tridiagonal. Utilizing its symmetry, the number of operations

can be reduced to $2m$. The number of operations required for solving a system with a full coefficient matrix is more than $m^3/3$, significantly more than $2m$.

Making Tracking Resistant to Outliers. Even with pure axial compression, some regions of the image may move out of the imaging plane and increase the decorrelation. In such parts the confidence of the data term is less and therefore the weight of the regularization term should be increased. The parts of the image with low correlation can be regarded as outliers and therefore a robust estimation technique can limit their effect. Before deriving a robust estimator for $\Delta\mathbf{d}$, we rewrite Equation 3 as $C(\Delta\mathbf{d}) = \Sigma_{i=1}^{m}\rho(r_i) + R(\Delta\mathbf{d})$ where $r_i = I_1(i) - I_2(i+d_i) - I_2'(i+d_i)\Delta d_i$, $\rho(r_i) = r_i^2$ and R is the regularization term. The M-estimate of $\Delta\mathbf{d}$ is $\Delta\hat{\mathbf{d}} = \arg\min_{\Delta\mathbf{d}} \{\Sigma_{i=1}^{m}\rho(r_i) + R(\Delta\mathbf{d})\}$ where $\rho(u)$ is a robust loss function [11]. The minimization is solved by setting $\frac{\partial C}{\partial \Delta d_i} = 0$:

$$\rho'(r_i)\frac{\partial r}{\partial \Delta d_i} + \frac{\partial R(\Delta\mathbf{d})}{\partial \Delta d_i} = 0 \tag{5}$$

A common next step [11] is to introduce a weight function w, where $w(r_i).r_i = \rho'(r_i)$. This leads to a process known as "iteratively reweighted least squares" (IRLS), which alternates steps of calculating weights $w(r_i)$ for $r_i = 1 \cdots m$ using the current estimate of $\Delta\mathbf{d}$ and solving Equation 5 to estimate a new $\Delta\mathbf{d}$ with the weights fixed. Among many proposed shapes for $w(\cdot)$, we use [11]

$$w(r_i) = \begin{cases} 1 & |r_i| < T \\ \frac{T}{|r_i|} & |r_i| > T \end{cases} \tag{6}$$

where T is a threshold that can be tuned. A small T will treat many samples as outliers. With the addition of the weight function, Equation 5 becomes

$$(\mathbf{w}\mathbf{I}_2'^2 + \alpha\mathbf{D} + \alpha_2\hat{\mathbf{I}})\Delta\mathbf{d} = \mathbf{w}\mathbf{I}_2'\mathbf{e} - (\alpha_1\mathbf{D} + \alpha_2\hat{\mathbf{I}})\mathbf{d} + \alpha_2\mathbf{d}^{t.p.} + \mathbf{b} \tag{7}$$

where $\mathbf{w} = diag(w(r_1)\cdots w(r_m))$. All of the results presented in this work are obtained with one iteration of the above equation unless otherwise specified. Current implementation of the AM algorithm with the IRLS takes 0.015s to generate a dense displacement field of size 1300×60 on a 3.4GHz P4 CPU(not including the DP run time). The computation time increases linearly with the size of images.

Frame Selection. The ultrasound probe is tracked in navigation/guidance systems to provide spatial information, to generate freehand 3D ultrasound, or to facilitate multi-modality registration. Through a calibration process, the 6DOF motion of the probe in the sensor coordinate system is transformed into image coordinate system [12]. The mean of the absolute motion value of all pixels in 3D, $\langle|v_x|\rangle$, $\langle|v_y|\rangle$ and $\langle|v_z|\rangle$, can be analytically related to the 6DOF sensor readings using straightforward and efficient geometric computations. For frame i and j to be selected from a sequence of frames for elastography,

$$Q_{i,i} = k_x \langle|v_x|\rangle^2 + k_y \langle|v_y|\rangle^2 + k_z \frac{\|\langle|v_z|\rangle - v_{z,opt}\|^3}{\langle|v_z|\rangle + c} \tag{8}$$

should be minimized where k_x, k_y, and k_z are weights for lateral, out-of-plane and axial displacements and $v_{z,opt}$ is the optimum axial motion. Please refer to [12] for a rationale of the shape this function. Note that the selected pairs are not necessarily consecutive frames. The parameters, k_x, k_y, k_z, $v_{z,opt}$ and c are manually tuned to 1, 2, 1, 0.7 and 1 for the AM elastography method.

3   Simulation, Phantom and Patient Results

Simulation Results. RF ultrasound data of two phantoms are simulated using Field II [13]. The first phantom is $50 \times 10 \times 55$mm and the second one is $36 \times 10 \times 25$mm. They are both made of homogeneous and isotropic material: the first one is uniform and the second one contains a circular hole filled with water, simulating a blood vessel in tissue (Figure 2 (a)). A uniform compression in the z direction is applied and the 3D displacement field of the phantom is calculated using ABAQUS finite element package (Providence, RI). The Poisson's ratio is set to $\nu = 0.49$ in both phantoms to mimic real tissue, which causes the phantom to deform in x & y directions as a result of the compression in the z direction.

Respectively 5×10^5 and 1.4×10^5 scatterers with uniform scattering strengths are uniformly distributed in the first and second phantom, ensuring more than 10 scatterers exist in a resolution cell. The scatterers are distributed in the 8mm diameter vein also (Figure 2 (a)). To construct deformed ultrasound images, the displacement of all of the scatterers is calculated by interpolating the displacement of the neighboring nodes in the finite element analysis. The parameters of the probe are set to mimic Siemens 5-10MHz probes. The probe frequency is 7.27MHz, the sampling rate is 40MHz and the fractional bandwidth is 60%.

The first phantom undergoes uniform compressions in the z direction to achieve strain levels of 2% to 14% in 2% intervals. Ground truth integer displacement values are used as the initial estimate for AM to decouple the performance of DP from AM. Accurate subpixel displacement field is calculated with AM and the mean strain values are compared with the ground truth (Figure 1 (a)-(c)). The results are only shown for 2%, 4%, 8% and 14% compression for better visualization. The results with two threshold values for IRLS and without IRLS demonstrate that outlier rejection does not affect the mean strain value, while increasing the regularization weight α_a increases underestimation of the displacement. The rate of increase of the underestimation with increasing α_a is significantly more with the unbiased regularization (dashed line) as expected.

Significantly higher signal to noise ratio (SNR) [2] values can be achieved with outlier rejection (Figure 1 (d)-(f)) without over-smoothing the image with high α_a values. To show the performance of the overall method, the initial integer displacement field is calculated with DP and accurate displacement field is calculated with (Figure 1 (g)-(i)). The SNR values are less than previous case especially at high strain values, where DP results deviates from ground truth.

The second simulation experiment is designed to show the effect of smoothness weight and IRLS threshold on contrast to noise ratio (CNR) [2] when the correlation is lower in parts of the image due to fluid motion. The phantom
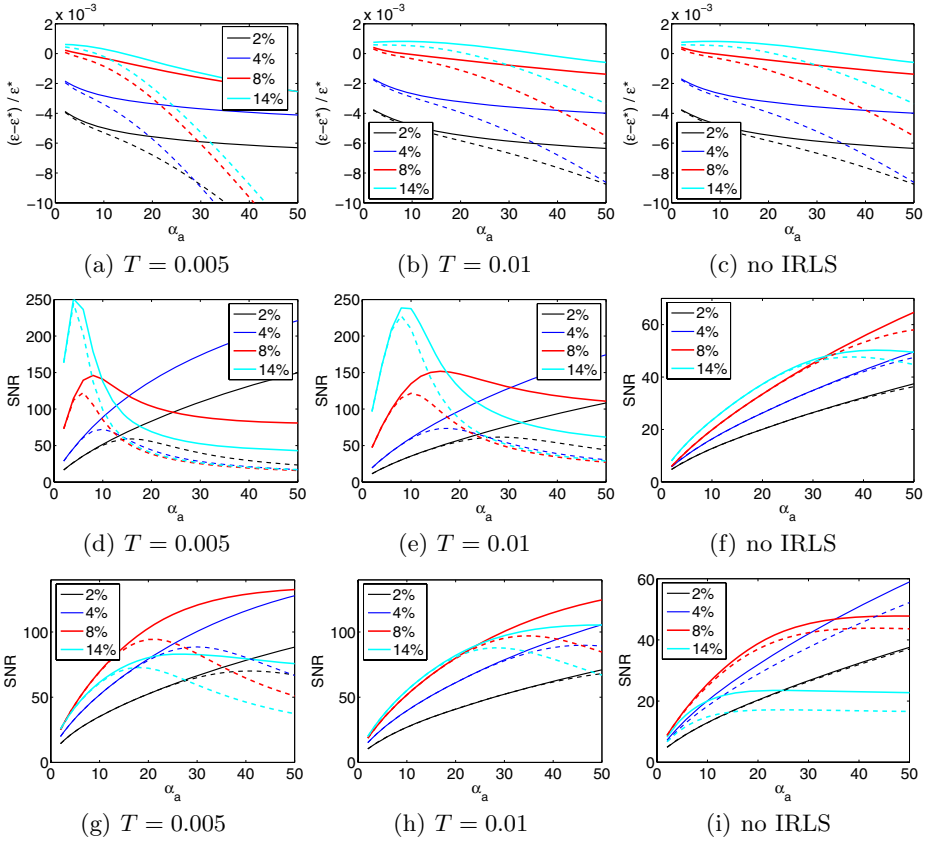
Fig. 1. Mean and SNR of the elastograms of the Field II simulated uniform phantom at four different compression levels (shown in percentage) for three IRLS T values. The solid and dashed lines correspond to biased and unbiased regularizations respectively. (a)-(c) shows the relative underestimation of the strain. ϵ is the mean strain calculated with the elastography method and ϵ^* is the ground truth. (d)-(f) shows the SNR of the AM. (g)-(i) shows the SNR of the AM with initial displacements found by DP.

contains a vein oriented perpendicular to the image plane (Figure 2). The initial integer displacement is generated with DP. The background window for CNR calculation is located close to the target window to show how fast the strain is allowed to vary, a property related to the spatial resolution. The maximum CNR with IRLS is 5.3 generated at $T = 0.005$ and $\alpha_a = 38$, and without IRLS is 4.8 at $\alpha_a = 338$. Such high α_a value makes the share of the data term in the cost function very small and causes over-smoothing.

Phantom Results. We perform freehand palpation experiment on a breast phantom to examine the performance of the frame selection technique. 50 frames of RF ultrasound data are acquired using a Siemens Antares system (Issaquah, WA). Our custom data acquisition program is connected to the Axius Direct Research Interface to send the command for capturing RF data. At the same

(a) simulation phantom

(b) finite element strain

(c) CNR
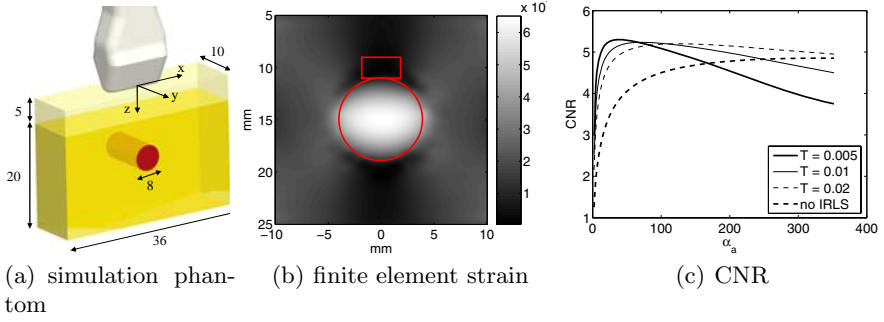
Fig. 2. The target (circular) and background (rectangular) windows for CNR calculation of (c) are shown in (b)
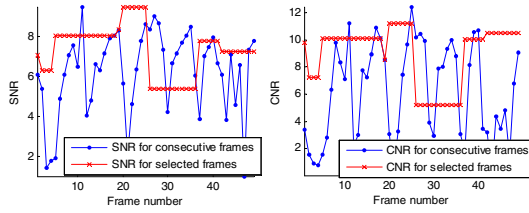
Fig. 3. The SNR and CNR of the phantom experiment with and without frame selection

(a) CT image

(b) B-mode image

(c) strain image
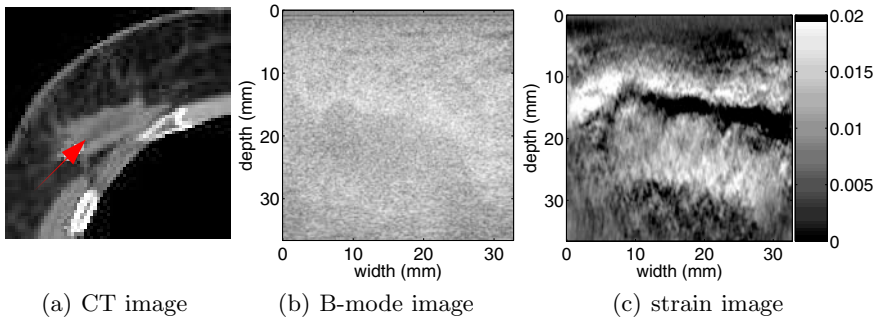
Fig. 4. Patient experiment results. The arrow points to the lumpectomy cavity.

time, the program collects tracking information from a Polaris tracker (Waterloo, Canada). Currently, the RF frames are stored on the ultrasound system and are processed offline. Figure 3 shows the SNR and CNR results. In automatic frame selection, $Q_{i,j}$ (equation 8) for any two frames i, j in a buffer of size 15 frames is calculated. For the two frames which give the minimum Q, the strain image is obtained. The next image is then fed to the buffer, its first image is removed and the frame selection is performed again. The automatic frame selection gives 8 frame pairs for strain calculation (as seen in the figure by 8 SNR and CNR

values). Without frame selection, 49 strain images are calculated. The average CNR and SNR values are improved from 4.91 to 7.19 and from 4.98 to 5.88 with frame selection.

Patient Results. We have acquired freehand palpation ultrasound RF data using the Siemens Antares system from patients approximately four weeks after lumpectomy. The ultrasound probe is tracked with the Polaris tracking system. Optimal frame selection is performed to select images for elastography using the AM method. The strain image (Figure 4) shows that the AM method can detect the thin hard scar tissue even though it is close to the cavity fluids which undergo incoherent motions and cause signal decorrelation. Since the AM method finds the displacement of all the samples on an A-line at the same time, the correlated data at the top and bottom of the cavity guide the method to find the correct displacement inside the cavity where the data is decorrelated.

4   Discussion and Conclusion

We introduced a novel method for calculating a dense displacement map by analytic minimization of a cost function. We used the IRLS method from robust statistics to make the tracking resistant to outliers. Moreover, we exploited the tracking data to optimize frame selection. Through simulation studies using Field II and finite element analysis, we showed that the proposed AM method generates high quality displacement estimates. The elastography method works in real-time. A comparison of the IRLS method with quality guided displacement tracking [14] which also aims for robustness is a subject of future work.

We chose the novel application of the lumpectomy cavity localization as the hard scar tissue is relatively thin and demands a high resolution elastography method. Also, incoherent fluid motions in the cavity causes large decorrelations, requiring a robust method. We have an active Institutional Review Board(IRB) protocol and have promising results from 9 patients which will be published in future work.

References

1. Offersen, B., Overgaard, M., Kroman, N., Overgaard, J.: Accelerated partial breast irradiation as part of breast conserving therapy of early breast carcinoma: a systematic review. Radiotherapy and Oncology 90(1), 1–13 (2009)
2. Ophir, J., Alam, S., Garra, B., Kallel, F., Konofagou, E., Krouskop, T., Varghese, T.: Elastography. Annu. Rev. Biomed. Eng. 213, 203–233 (1999)

3. Hall, T., Zhu, Y., Spalding, C.: In vivo real-time freehand palpation imaging. Ultrasound Med. Biol. 29, 427–435 (2003)
4. Zahiri, R., Salcudean, S.: Motion estimation in ultrasound images using time domain cross correlation with prior estimates. Biomed. Eng. 53(10), 1990–2000 (2006)
5. Pellot-Barakat, C., Frouin, F., Insana, M., Herment, A.: Ultrasound elastography based on multiscale estimations of regularized displacement fields. IEEE Trans. Med. Imag. 23(2), 153–163 (2004)
6. Brusseau, E., Kybic, J., Deprez, J., Basset, O.: 2-d locally regularized tissue strain estimation from radio-frequency ultrasound images: Theoretical developements and results on experimental data. IEEE Trans. Med. Imag. 27(2), 145–160 (2008)
7. Rivaz, H., Boctor, E., Foroughi, P., Fichtinger, G., Hager, G.: Ultrasound elastography: a dynamic programing approach. IEEE Trans. Med. Imag 27, 1373–1377 (2008)
8. Lyshchik, A., Higashi, T., Asato, R., et al.: Thyroid gland tumor diagnosis at US elastography. Radiology 237, 202–211 (2005)
9. Kadour, M., Noble, A.: Assisted-freehand ultrasound elasticity imaging. IEEE Trans. Ultrason. Ferroelectr. Freq. Control. 129, 36–43 (2009)
10. Lindop, J., Treece, G., Gee, A., Prager, R.: An intelligent interface for freehand strain imaging. Ultrasound Med. and Biol. 34(7), 1117–1128 (2008)
11. Stewart, C.: Robust parameter estimation in vision. SIAM 41(3), 513–537 (1999)
12. Foroughi, P., Hager, G., Boctor, E.: Robust elasticity imaging using external tracker. In: IEEE Int. Symp. Biomed. Imag. (in press, 2009)
13. Jensen, A.: Field: A program for simulating ultrasound systems. Medical & Biological Engineering & Computing 34, 351–353 (1996)
14. Chen, L., Treece, G., Lindop, J., Gee, A., Prager, R.: A quality-guided displacement tracking algorithm ultrasonic elasticity imaging. Med. Imag. A. 13, 286–296 (2009)

Tracked Ultrasound Elastography (TrUE)

Pezhman Foroughi[1], Hassan Rivaz[1], Ioana N. Fleming[1], Gregory D. Hager[1], and Emad M. Boctor[1,2]

[1] Dept. of Computer Science, Johns Hopkins University, Baltimore, MD, USA
[2] Dept. of Radiation Oncology, Johns Hopkins University, Baltimore, MD, USA

Abstract. This paper presents a robust framework for freehand ultrasound elastography to cope with uncertainties of freehand palpation using the information from an external tracker. In order to improve the quality of the elasticity images, the proposed method selects a few image pairs such that in each pair the lateral and out-of-plane motions are minimized. It controls the strain rate by choosing the axial motion to be close to a given optimum value. The tracking data also enables fusing multiple strain images that are taken roughly from the same location. This method can be adopted for various trackers and strain estimation algorithms. In this work, we show the results for two tracking systems of electromagnetic (EM) and optical tracker. Using phantom and *ex-vivo* animal experiments, we show that the proposed techniques significantly improve the elasticity images and reduce the dependency to the hand motion of user.

Key words: Ultrasound, Elastography, Elasticity, Tracking, Strain

1 Introduction

Ultrasound elastography is an emerging medical imaging modality which involves imaging the mechanical properties of tissue and has numerous clinical applications. Among many variations of ultrasound elastography [1], our work focuses on real-time static elastography, a well-known technique that applies quasi-static compression of tissue and simultaneously images it with ultrasound. Within many techniques proposed for static elastography, we focus on freehand palpation elasticity imaging which involves deforming the tissue by simply pressing the ultrasound probe against it. Freehand ultrasound elastography has shown great potential in clinical applications especially for diagnosis and screening of breast lesions [2]. The application of elastography is not limited to breast, and other applications such as diagnosis of prostate cancer, monitoring ablation and deep vein thrombosis have also been studied.

Despite the reports on success of elastography, yet it has not become a part of any routine clinical application. The main reason is that elastography is highly qualitative and user-dependent. The best result is achieved when the user compresses and decompresses the tissue uniformly in the axial direction with the proper hand motion. It is difficult to control the compression rate as it is governed by the hand motion and the frame rate of RF data. Also, small lateral

or out-of-plane motions can compromise the quality of images. However, it is difficult to induce pure axial motion with freehand compression. Sophisticated algorithms can only partially address the problem by compensating for in-plane motions and applying smoothness constraints. The images are also hard to interpret, and artifacts –caused by failure of the strain estimation algorithm or poor hand motion– may be mistaken for lesions inside the soft tissue. Developing an elastography technique that is not affected by poor hand motion and other sources of signal decorrelation will pave the way for wide-spread clinical use of elastography.

To improve the reliability, quality metrics such as persistence in strain images have been developed [3, 4]. This quality indicator is calculated for each image and provided to the user as feedback. Persistence is also used to merge multiple elasticity images together [3]. To measure the persistence, strain is computed for two pairs of echo frames, and the resulting images are correlated. Although these techniques offers a major advantage, there remains several limitations. First, the strain has to be estimated before the calculation of the quality metric. With typical ultrasound settings, the frame rate can reach more than 30 Hz. For subsequent frames, an efficient implementation of this image-based metric might cope with this rate. Nonetheless, the task will be extremely difficult to try all the combinations in a series of frames. Moreover, the quality metric will not be able to provide feedback to the user whether he/she should adjust the palpation in certain direction. Also, there would be minimal control over the strain rate.

The ultrasound probe is often tracked in navigation/guidance systems to provide spatial information, to form freehand 3D ultrasound, or to facilitate multi-modality registration. In this work, we exploit the tracking data to enhance the quality of the elasticity images. We use the tracking data to select multiple image pairs that contain the optimum deformation for the elastography algorithm. The optimum value for lateral and out-of-plane motions is zero, and the optimum axial motion is determined by the specific elastography algorithm used, which is Normalized Cross-Correlation (NCC) in this work. Next, we fuse the strain images obtained from the multiple image pairs together based on the location of each strain image to improve image quality. We assume that the ultrasound data is 2D. Nonetheless similar techniques proposed here could be extended to 3D ultrasound.

2   Methodology

Consider a sequence of RF data collected during the palpation of tissue using a tracked transducer. We have previously shown that it is possible to synchronize the RF frames with the tracking information relying only on the same data collected during palpation [5]. From synchronization, the tracking information is interpolated at the incident time of each frame. The input to our algorithm is then a series of RF frames along with their corresponding transformation.

First, we need to define a distance function between two frames of RF data. For this purpose, we use a model of image decorrelation in presence of out-of-

plane and lateral motion. RF signal is often modeled as the collective response of scatterers randomly distributed within the resolution cell of the ultrasound [6, 7]. Each scatterer is assumed to have an amplitude governed by the shape of the resolution cell and a phase which is distributed from 0 to π uniformly at random. Considering a Gaussian shape for the resolution cell Prager *et. al* [8] calculated the correlation as a function of out-of-plane motion to be $exp(-\frac{\delta^2}{2\sigma^2})$. δ and σ denote the displacement and the width of the resolution cell respectively. Although this function is only valid for fully developed speckle, it provides a convenient estimate of correlation. It should be noted that in [8], the displacement is estimated from correlation, whereas here, we intend to define an energy function based on displacement. Extending this formula to both out-of-plane and lateral displacements, we define our energy function, $E(x, z)$, as follows:

$$E(D_x, D_z) = exp(-K_x \cdot D_x^2 - K_z \cdot D_z^2), \tag{1}$$

where D_x and D_z represent the displacement in out-of-plane and lateral directions (D_y is reserved for axial motion). K_x and K_z determine the sensitivity to a certain direction. In order to be able to use this function, we need a component-wise metric representing the distance of two frames given their homogeneous transformations. The first step is to compute the relative transformation between them. Suppose $a = [a_x\, a_y\, a_z]^T$ is the axis-angle representation of the relative rotation, and $t = [t_x\, t_y\, t_z]^T$ is the relative translation. Assuming a small rotation, the relative displacement of a point, $P = [x\, y\, 0]^T$, will be $d = a \times P + t$. We then define the distance vector of two frames, $D = [D_x\, D_y\, D_z]^T$, as the RMS of the components of d for all the points in the region of interest (ROI):

$$D_x = sqrt\{ \ \frac{1}{(y_2 - y_1)} \int_{y_1}^{y_2} (-a_z \cdot y + t_x)^2 dy \ \},$$

$$D_y = sqrt\{ \ \frac{1}{(x_2 - x_1)} \int_{x_1}^{x_2} (a_z \cdot x + t_y)^2 dx \ \},$$

$$D_z = sqrt\{ \ \frac{1}{(y_2 - y_1)(x_2 - x_1)} \int_{x_1}^{x_2} \int_{y_1}^{y_2} (a_x \cdot y - a_y \cdot x + t_z)^2 dy dx \ \}, \tag{2}$$

where $sqrt\{.\}$ returns the root. Here, ROI is assumed to be rectangular and determined by x_1, x_2, y_1, and y_2. The vector D provides a measure of distance for each direction separately. We use this vector in Equation (1) which gives us an estimate of "pseudo-correlation" over the ROI.

The data goes through four stages of processing to create a single high-quality strain image. In the first step, few images are selected from the data series that are approximately collected from one cross-section of tissue with minimal lateral and out-of-plane motion. To this end, the energy function of each frame is computed with respect to all other frames in the sequence. Then, the total energy is found for each frame as the sum of the energies of the M closest frames, where closeness implies higher energy, and M is the maximum number of frames to be selected. Then, the frame with the highest total energy

(the center frame) is identified, and the M closest frames to the center frame including itself are selected. Additionally, the frames that have E of less than 0.5 with respect to the center frame are disqualified. This is applied to ensure lower number of frames are chosen when M frames from one cross-section are not available.

In the next stage, the program evaluates all possible combination of frame pairs for elastography. For M frames, there will be $\binom{M}{2} = M(M-1)/2$ pair combinations which will be compared using a slightly modified version of E. Since the pairs are directly compared, it suffices to minimize the exponent of Equation (1) in order to maximize E. We also add a term for axial motion that penalizes compressions that are higher than an optimum compression value, t_{opt}. Hence, a "cost function", $C1$, is defined as follows:

$$C1(D) = K_x \cdot D_x^2 + K_y \cdot \tilde{D}_y^{\,2} + K_z \cdot D_z^2, \quad \tilde{D}_y = \begin{cases} D_y - t_{opt}, & |D_y - t_{opt}| > 0 \\ 0, & |D_y - t_{opt}| \le 0 \end{cases} \quad (3)$$

t_{opt} implies the optimal strain. Optimal strain can be theoretically defined as described in [9]. It also depends on the robustness of the elasticity estimation algorithm. t_{opt} might be within the range of the resolution of the tracker. Therefore, at this stage we do not assign a penalty for the compressions less than t_{opt}. If the compression is close to zero, the contrast of the reconstructed image degrades. The program filters the pairs with low compression in the next stage using image content. Similar to the first part, a maximum number of frames with lowest cost are selected provided that the cost is lower than a threshold. The threshold is not strict to ensure acceptable pairs are not filtered.

The final pairs are selected by recovering the global lateral motion and compression by matching the two RF frames in each pair. The tracking information is used to initialize the search. For instance, the search range for compression is set to be from zero to the tracker reading in axial direction padded in both sides with the maximum error of the tracker. Given two frame I_1 and I_2, the amount of lateral motion a, and compression, b, is found by solving cross-correlation:

$$\arg \max_{a,b} \left\{ \sum_{x,y \in G} I_1(x, y) \cdot I_2(x + a, by) + I_1(x - a, -by) \cdot I_2(x, y) \right\}. \quad (4)$$

The RF data is normalized with standard variation and assumed to have zero mean. We employ two tricks which extensively increases the speed of search. First, we do not match the entire image to solve for these parameters. Instead, only pixels on a grid, G, are used as described by Equation (4). The two terms of Equation (4) ensures that the search remains reciprocal, which means switching the images only affects the sign of a and b. Second, a is recovered by matching only the top part of the two images while b is fixed to one. The reason is that the displacement due to compression is minimal in that region.

Having the global motions, the cost function is modified to penalize very low compressions:

$$C2(\widehat{D}) = K_x \cdot \widehat{D_x}^2 + K_y \cdot \frac{|\widehat{D_y} - t_{opt}|^3}{\widehat{D_y} + c} + K_z \cdot D_z^2, \tag{5}$$

where $\widehat{D_x}$ and $\widehat{D_y}$ are the global motions from Equation (4) converted to mm. c is a small number that limits the cost of zero compression. Finally, the pairs with the lowest cost are selected until a maximum number of frame pairs is reached or the minimum cost grows higher than the average cost.

The last step involves computing the strain for all the selected frame pairs. We have implemented normalized cross-correlation (NCC) [10] to recover the displacements and least squares estimation to calculate the strain. Before calculating strain, the global lateral motion and compression from the previous step are compensated in one image using cubic interpolation. This is known to reduce the error of strain estimation [11]. The final strain image, S_{final} is the weighted average of all the strains:

$$S_{final} = \frac{\sum_{i=1}^{m} w_i \cdot S_i}{\sum_{i=1}^{m} w_i}, \ \ w_i = \begin{cases} \frac{\rho_i}{1-\rho_i}, & \rho_i > 0.7 \\ 0, & otherwise \end{cases} \tag{6}$$

where ρ_i is the correlation coefficient for the ith pair after applying the displacements, and m is the number of pairs. Fusing the strains in this fashion is acceptable since the algorithm only allows for compressions that are close to a predetermined amount optimal for strain estimation.

3   Experiments and Results

We acquired ultrasound data using a SONOLINE Antares^{TM} ultrasound system (Siemens Medical Solutions USA, Inc.) with a high-frequency ultrasound transducer (VF10-5) at center frequency of 6-8 MHz. We accessed RF through the Axius Direct^{TM} Ultrasound Research Interface provided by Siemens. Our custom data acquisition program was connected to this interface to send the command for capturing RF data. At the same time, the program collected tracking information from either a "Polaris" optical tracker (Northern Digital Inc., Waterloo, Canada) with passive markers or the "medSAFE" EM tracker (Ascension Tech. Corp.).

RF data and tracking information was captured from a breast phantom containing a harder lesion (CIRS elastography phantom, Norfolk, VA) and *ex-vivo* pig liver. Alginate was injected to the liver to mark a part of liver, and then, that area was ablated. The users were asked to palpate the tissue over the hard lesion in the breast phantom and the ablated lesion in the pig liver while data was being collected. Between 100 to 138 RF frames were acquired with the rate of about 30 frames per second.

The first set of data was captured by an experienced user from the breast phantom. Figure 1(a) shows the translation components of hand motion with respect to the first frame. The axial motion is dominant and there is only a

(a) Freehand palpation   (b) Strain image (TrUE)
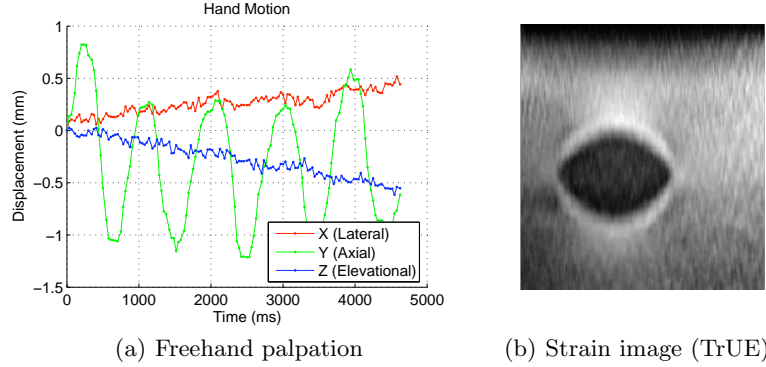
Fig. 1. (a) shows the translation of probe w.r.t. the first image. Proper hand motion is applied as the axial compression is dominant. (b) is the output of our proposed algorithm.
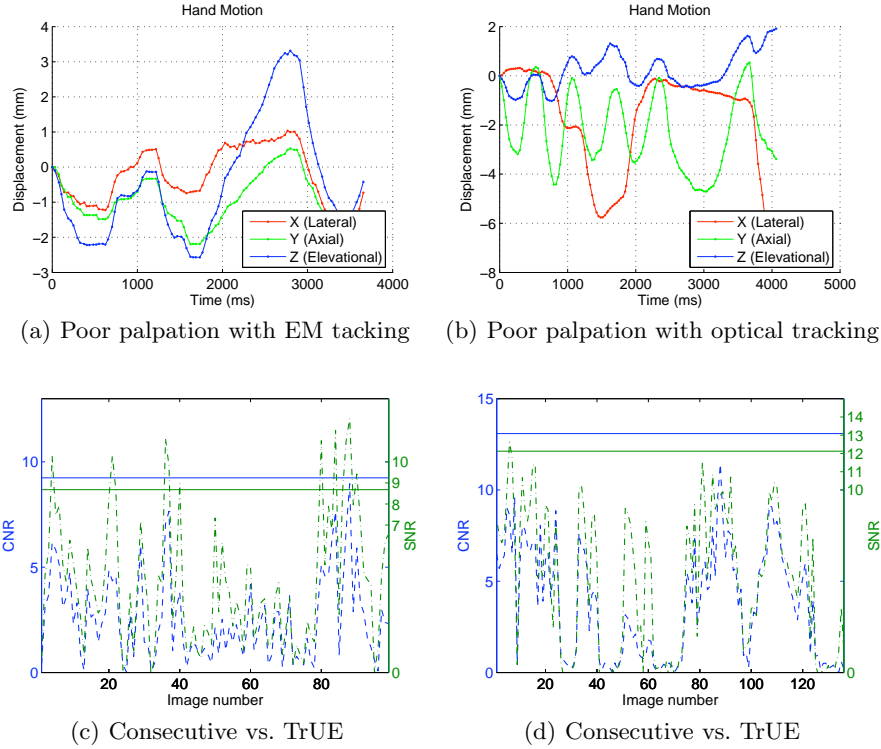
gradual drift in the lateral and elevational directions. Figure 1(b) depicts the high-quality strain image resulting from the TrUE algorithm.

Applying a compression similar to the one shown in Figure 1(a) is a difficult task for novice or even intermediate users. This is especially the case where axial compression does not translate into a simple up and down motion. Ultrasound gel creates a slippery surface that makes the palpation prone to out-of-plane motion. Two case are shown in Figure 2, where one is tracked with the EM tracker and the other one with the optical tracker. In Figure 2(a) the hand motion contains a large amount of out-of-plane motion, whereas, in Figure 2(b), the user has moved the probe laterally. In both cases, the TrUE algorithm generates reliable results. Figures 2 (c) and (d) show the contrast-to-noise ratio (CNR) and signal-to-noise ratio (SNR) of the strain image. The CNR and SNR value are computed from:

$$\mathrm{CNR} = \sqrt{\frac{2(\bar{s}_b - \bar{s}_t)^2}{\sigma_b^2 + \sigma_t^2}}, \quad \mathrm{SNR} = \frac{\bar{s}}{\sigma}, \tag{7}$$

where $\bar{s}$ and σ denote the mean and standard deviation of intensities. The $_t$ or $_b$ subscripts show that the computation is only for the target or the background region, respectively. The SNR and CNR for computing the strain from consecutive frames (the dashed curve) is compared to the SNR and CNR of the strain image from the proposed method (solid line). Using consecutive frames is the standard method of elastography in ultrasound machines. Almost in all cases the TrUE algorithm outperforms the consecutive frames by a large margin.

Although the SNR and CNR provide quantitative measures to compare the strain images, they do not directly reflect the visual quality of strain. In Figure 3, we show results of elastography using our frame selection technique as well as four other strain images calculated from consecutive frames. The Figure shows the effects of improper compression in consecutive frames in the strain image. At the same time our algorithm provides a single reliable strain.

(a) Poor palpation with EM tacking

(b) Poor palpation with optical tracking

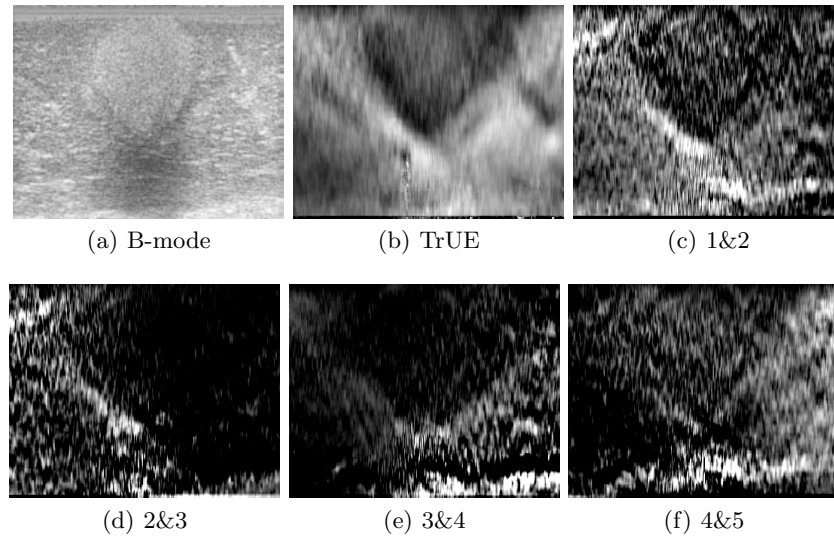(c) Consecutive vs. TrUE

(d) Consecutive vs. TrUE

Fig. 2. Two cases of improper motions are shown where the hand motion suffers from large lateral and elevational components evident in relative translations. The results of case 1 with EM tacker is shown on the left column, and the results of case 2 with optical tracker is shown on the right column.

4   Discussion

We presented a method of ultrasound elastography which is robust to the quality of the hand motion of the user. Using the information from an external tracker, it automatically selects multiple frame pairs with a specific compression and minimal undesired motions. Our approach does not take into account the tissue motion from other sources such as breathing or patient motion. However, these types of motions are not normally problematic since they occur with a slower pace compared to hand motion.

Our experiments shows that even when the transducer has severe lateral or out-of-plane motions, the algorithm still manages to produce good results. The multi-stage frame selection and careful image fusion makes the TrUE method less sensitive to tacker accuracy and robust to strain estimation failures.

We are planning to use the proposed method in a breast cancer study. For this purpose, we will be implementing our MATLAB code in C. The stain estimation which is still the bottleneck of our approach will be executed in GPU allowing for the use of sophisticated algorithms.

(a) B-mode   (b) TrUE   (c) 1&2

(d) 2&3   (e) 3&4   (f) 4&5

Fig. 3. Comparison of the strain from TrUE vs. consecutive frames for *ex-vivo* pig liver.

References

1. Ophir, J., Alam, S., Garra, B., Kallel, F., Konofagou, E., Krouskop, T., Varghese, T.: Elastography: ultrasonic estimation and imaging of the elastic properties of tissues. Annu. Rev. Biomed. Eng. **213** (November 1999) 203–233
2. Garra, B., et. al: Elastography of breast lesions: initial clinical results. Radiology **202** (1997) 79–86
3. Lindop, J.E., Treece, G.M., Gee, A.H., Prager, R.W.: An intelligent interface for freehand strain imaging. Ultrasound Med Biol **34** (2008) 1117–1128
4. Jiang, J., Hall, T.J., Sommer, A.M.: A novel strain formation algorithm for ultrasonic strain imaging. IEEE Ultrasonics Symposium (2006) 1282–1285
5. Foroughi, P., Hager, G., Boctor, E.: Robust elasticity imaging using external tracker. In: IEEE Int. Symp. Biomed. Imag. (2009) 209–212
6. Wagner, R., Smith, S., Sandrik, J., Lopez, H.: Statistics of Speckle in Ultrasound B-Scans. IEEE Trans. Sonics and Ultrasonics **17**(3) (1983) 251–268
7. Shankar, P.: A general statistical model for ultrasonic backscattering from tissues. IEEE Trans Ultrason Ferroelectr Freq Control **47**(3) (May 2000) 727–736
8. Prager, R., et. al: Sensorless freehand 3-d ultrasound using regression of the echo intensity. Ultrasound Med. Biol. **29** (2003) 437–446
9. Varghese, T., Ophir, J.: A theoretical framework for performance characterization of elastography: the strain filter. IEEE Transactions on Ultrasonics, Ferroelectrics and Frequency Control **44** (1997) 164–172
10. Cspedes, I., Huang, Y., Ophir, J., Spratt, S.: Methods for estimation of subsample time delays of digitized echo signals. Ultrasound Imaging **17**(2) (1995) 142–71
11. Varghese, T., Ophir, J.: Performance optimization in elastography: Multicompression with temporal stretching. IEEE Transactions on Ultrasonics, Ferroelectrics and Frequency Control **18** (1996) 193–214(22)

Ultrasound Elastography Using Three Images

Hassan Rivaz, Emad M. Boctor, Michael A. Choti, and Gregory D. Hager

Johns Hopkins University

Abstract. Displacement1 estimation is an essential step for ultrasound elastography and numerous techniques have been proposed to improve its quality using *two* frames of ultrasound RF data. This paper introduces a technique for calculating a displacement field from *three* frames of ultrasound RF data. To this end, we first introduce constraints on variations of the displacement field with time using mechanics of materials. These constraints are then used to generate a regularized cost function that incorporates amplitude similarity of three ultrasound images and displacement continuity. We optimize the cost function in an expectation maximization (EM) framework. Iteratively reweighted least squares (IRLS) is used to minimize the effect of outliers. We show that, compared to using two images, the new algorithm reduces the noise of the displacement estimation. The displacement field is used to generate strain images for quasi-static elastography. Phantom experiments and *in-vivo* patient trials of imaging liver tumors and monitoring thermal ablation therapy of liver cancer are presented for validation.

1 Introduction

Displacement, motion or time delay estimation in ultrasound images is an essential step in numerous medical imaging tasks including the rapidly growing field of imaging the mechanical properties of tissue [1]. In this work, we perform displacement estimation for quasi-static ultrasound elastography [1], which involves deforming the tissue slowly with an external mechanical force, imaging the tissue during the deformation, and performing displacement estimation using the images. More specifically, we focus on real-time freehand palpation elastography [2–7] where the external force is applied by simply pressing the ultrasound probe against the tissue. Ease of use, real-time performance and providing invaluable elasticity images for diagnosis and guidance/monitoring of surgical operations are the key factors that have led to its successful commercialization.

A typical ultrasound frame rate is 20-60 fps. As a result, an entire series of ultrasound images are freely available during the tissue deformation. Multiple ultrasound images have been used before to obtain strain images of highly compressed tissue by accumulating the intermediate strain images, and to obtain persistently high quality strain images by performing weighted averaging of the strain images [8–10]. Accumulating and averaging strain images increases their signal to noise ratio (SNR) and contrast to noise ratio (CNR). However, these techniques are susceptible to drift, a problem with any sequential tracking system
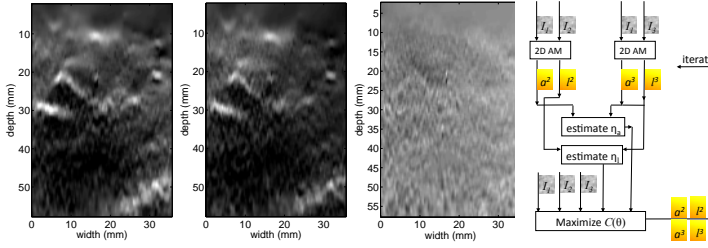
Fig. 1. Left: *in-vivo* images of liver. First and second (S_1 and S_2 from left) are two strain fields calculated from I_1 and I_2, and from I_2 and I_3 respectively. S_1 & S_2 look "similar". Third image is $S_1 - \eta S_2$ for $\eta = 1.1$. The strain range in the first two images is 0 to 0.6%, and in the third image is $\pm 0.3\%$. Right shows the ElastMI algorithm.

[11]. In addition, these techniques do not exploit additional images to *improve displacement estimation*, which has many applications besides strain estimation. Time series of ultrasound data has also been used to characterize tissue [12] and improve elasticity reconstruction [13] and viscoelastic parameters [14, 15].

Figure 1 shows *two consecutive strain images* calculated from *three ultrasound images* using the 2D analytic minimization (AM) method [16]. Our motivation is to utilize the similarity of these two images to calculate a low variance displacement field from three images. The contributions of this work are: (1) introducing constraints on variation of the motion fields based on similarities of strain images through *time*; (2) proposing an EM algorithm to solve for motion fields using three images, and (3) reporting clinical tstudies of ablation guidance/monitoring, with data collection corresponding to before, during and after ablation.

The rest of this paper is summarized as follows. We first introduce the Elastography using Multiple Images (ElastMI) algorithm for tissue displacement estimation, which minimizes a cost function that incorporates data obtained from three images and exploits mechanical constraints. The estimated low variance displacement field can be used in numerous applications in imaging mechanical properties of tissue; we use it for generating strain images by calculating its spatial derivative. We use phantom and *in-vivo* clinical studies to compare ElastMI versus the recently developed elastography technique of 2D AM (code available online at `www.cs.jhu.edu/~rivaz`) [16].

2   ElastMI: Elastography Using Multiple Images

We have a set of $p = 3$ images I_k, $k = 1 \cdots 3$, each of size $m \times n$. Let the 2D displacement field $\mathbf{d}^k = (a^k, l^k)$ denote the displacement between I_k and I_1, where a refers to the axial (i.e. in the direction of the ultrasound beam) and l to the lateral (i.e. perpendicular to the beam and in the imaging plane) directions. By the choice of reference $\mathbf{d}^1 = 0$. Note that we set I_1 as the reference image to simplify the notation. However, in our implementation we always take the middle image (i.e. I_2) as the reference. Our goal is to calculate a high quality $\mathbf{d}^2$ by utilizing all three images in a group-wise approach.

It is well known that many tissue types display linear strain-stress relation in the 0 to 5% range (see [1] for example). In a freehand palpation elastography setup with ultrasound acquisition rate of 20 fps or more, taking three consecutive images as I_1, I_2, I_3 corresponds to strain values of less than 1% and therefore the linearity assumption is valid. Using this property and some simplifying assumptions, it can be shown that the ratio of the strain and displacement fields in different times is a constant value, i.e. *strain images are similar up to a scale* as in Figure 1. We denote the scale factor by $\boldsymbol{\eta} = (\eta_a, \eta_l)$, and allow it to slightly change spatially to account for small nonlinearities in the tissue. As such, η_a and η_l are themselves scale fields in the axial and lateral directions each of size $m \times n$. Using this notation we have $a^3 = \eta_a.*a^2$ and $l^3 = \eta_l.*l^2$ where $.*$ denotes point-wise multiplication.

Let $\boldsymbol{\theta}$ contain all the displacement unknowns $\mathbf{d}^2$ and $\mathbf{d}^3$. The MAP estimate of $\boldsymbol{\theta}$ is obtained by maximizing its posterior probability

$$\Pr(\boldsymbol{\theta} \mid I_1, I_2, I_3) \propto \Pr(I_1, I_2, I_3 \mid \boldsymbol{\theta}) \Pr(\boldsymbol{\theta}) \tag{1}$$

where we have ignored the normalization denominator. The data term is calculated as $\Pr(I_1, I_2, I_3 \mid \boldsymbol{\theta}) = \Sigma_{\boldsymbol{\eta}} \Pr(I_1, I_2, I_3, \boldsymbol{\eta} \mid \boldsymbol{\theta})$. The summation over the latent variable $\boldsymbol{\eta}$ makes the optimization problem intractable. We therefore use Expectation Maximization (EM) to make the problem tractable as following.

1. Initialize: find an estimate for $\boldsymbol{\theta}$ by applying the 2D AM method [16] to two pairs of images (I_1, I_2) and (I_1, I_3) independently.
2. E-step: find an estimate for $\boldsymbol{\eta}$ using $\boldsymbol{\theta}$ (details below).
3. M-step: update $\boldsymbol{\theta}$ with the current estimate of $\boldsymbol{\eta}$ (details below).
4. Iterate between 2 and 3 until convergence.

The algorithm is shown in Figure 1 right. Note that unlike the traditional EM which maximizes $\Pr(I_1, I_2, I_3 \mid \boldsymbol{\theta})$, we maximize the posterior probability of $\boldsymbol{\theta}$ (Equation 1). Steps 2 and 3 are elaborated below.

Calculating η from θ Using Least Squares. At each sample (i, j) in the displacement field $\mathbf{d}^2_{i,j}$, $i = 1 \cdots m$, $j = 1 \cdots n$ take a window of size $m_w \times n_w$ centered at the sample (m_w and n_w are in the axial and lateral directions respectively and both are odd numbers). Stack the axial and lateral components of $\mathbf{d}^2_{i,j}$ that are in the window in two vectors $\mathbf{a}^2_{i,j}$ and $\mathbf{l}^2_{i,j}$, each of length $m_w \times n_w$. Similarly, generate $\mathbf{a}^3_{i,j}$ and $\mathbf{l}^3_{i,j}$ using $\mathbf{d}^3$. Note that since both displacement fields $\mathbf{d}^2_{i,j}$ and $\mathbf{d}^3_{i,j}$ are calculated with respect to samples on I_1, they correspond to the same sample (i, j). We first calculate the axial component $\eta_{(i,j),a}$ ($\boldsymbol{\eta}_{(i,j)} = (\eta_{(i,j),a}, \eta_{(i,j),l})$). Discarding the spatial information in $\mathbf{a}^2_{i,j}$ and $\mathbf{a}^3_{i,j}$, we can average the two vectors into two scalers $\bar{\mathbf{a}}^2_{i,j}$ and $\bar{\mathbf{a}}^3_{i,j}$ and simply calculate $\eta_{(i,j),a} = \bar{\mathbf{a}}^3_{i,j}/\bar{\mathbf{a}}^2_{i,j}$. However, a more elegant way which also takes into account the spatial information is by calculating the least squares solution to the following over-determined problem (superscript T denotes transpose).

$$\mathbf{a}^2_{i,j}\eta_{(i,j),a} = \mathbf{a}^3_{i,j} \quad \text{giving} \quad \eta_{(i,j),a} = \frac{\mathbf{a}^{2T}_{i,j}\mathbf{a}^3_{i,j}}{\mathbf{a}^{2T}_{i,j}\mathbf{a}^2_{i,j}}, \tag{2}$$

which is what we use in our implementation. To calculate the ratio of the lateral displacement fields $\eta_{(i,j),l}$, we take into account possible lateral slip of the probe, which results in a rigid-body-motion. The rigid-body-motion can be simply calculated by averaging the lateral displacement in $\mathbf{d}_{i,j}^2$ and $\mathbf{d}_{i,j}^3$ in the entire image, and calculating the difference between these two average lateral displacements. The lateral scaling factor $\eta_{(i,j),l}$ can be calculated using an equation similar to 2 where the axial displacement $\mathbf{a}_{i,j}$ is replaced with the lateral displacements $\mathbf{l}_{i,j}$. However, we use the following approach which results in a better estimate for $\eta_{(i,j),l}$. The lateral strain ϵ_l is simply $\nu\epsilon_a$ where ν is an unknown Poisson's ratio. Since ν has a small dynamic range in soft tissue and since the difference between the two displacement maps $\mathbf{d}^2$ and $\mathbf{d}^3$ is small, we can assume that ν does not vary from $\mathbf{d}^2$ to $\mathbf{d}^3$. Therefore, $\eta_{(i,j),l} = \eta_{(i,j),a}$. This gives better estimate for $\eta_{(i,j),l}$ since axial displacement estimation is more accurate [16].

Calculating $\boldsymbol{\theta}$ by Maximizing Its Posterior Probability. To analytically solve the MAP estimate of $\boldsymbol{\theta}$, we assume that the data is independent and that the noise model is Gaussian. Although not completely held in real images, these assumptions are also the foundation behind sum of square difference and correlation based elastography methods, which have been extensively shown to produce reliable results. With these assumptions, the robust MAP estimate for $\boldsymbol{\theta}$ can be obtained by minimizing the following cost function

$$C(\boldsymbol{\theta}) = \sum_{i=1}^{m} w_{12,i} \left(I_1(\mathbf{x}_i) - I_2(\mathbf{x}_i + \hat{\mathbf{d}}_i^2) - \delta\mathbf{d}_i^{2T}\nabla I_2(\mathbf{x}_i + \hat{\mathbf{d}}_i^2) \right)^2 +$$
$$\sum_{i=1}^{m} w_{13,i} \left(I_1(\mathbf{x}_i) - I_3(\mathbf{x}_i + \eta_{i,a}\hat{\mathbf{d}}_i^2) - \eta_{i,a}\delta\mathbf{d}_i^{2T}\nabla I_3(\mathbf{x}_i + \eta_{i,a}\hat{\mathbf{d}}_i^2) \right)^2 +$$
$$\sum_{i=1}^{m} (\mathbf{d}_i^2 - \mathbf{d}_{i-1}^2)^T A(\mathbf{d}_i^2 - \mathbf{d}_{i-1}^2) \tag{3}$$

where $\hat{\mathbf{d}}_i^2$ is the estimate obtained using 2D AM, $\delta\mathbf{d}_i^2 = \mathbf{d}_i^2 - \hat{\mathbf{d}}_i^2$ is the update in the displacement that we are looking for, $A = diag(\alpha,\beta)$ is a 2×2 diagonal matrix with tunable regularization weights (α,β) that we adjust manually in this work, and ∇ denotes the gradient operator. Robustness is achieved using IRLS through weights $w_{12,i}$ and $w_{13,i}$ which are calculated as following

$$w_{1k,i} = w(I_1(\mathbf{x}_i) - I_k(\mathbf{x}_i + \hat{\mathbf{d}}_i^k)), \text{for } k = 2,3, \text{ and } w(r_i) = \left\{ \begin{array}{ll} 1 & |r_i| < T \\ \frac{T}{|r_i|} & |r_i| > T \end{array} \right. \tag{4}$$

where T is a tunable parameter which determines the residual level for which sample i can be treated as outlier. A small T will treat many samples as outliers.

Setting the derivative of C w.r.t. the axial ($\delta a_i^2 = \delta\mathbf{d}_{i,a}^2$) and lateral ($\delta l_i^2 = \delta\mathbf{d}_{i,l}^2$) components of $\delta\mathbf{d}_i^2$ for $i = 1\cdots m$ to zero and stacking the $2m$ unknowns in $\delta\mathbf{d}^2 = \left[\delta a_1^2\ \delta l_1^2\ \delta a_2^2\ \delta l_2^2 \cdots \delta a_m^2\ \delta l_m^2 \right]^T$ and the $2m$ initial estimates in $\hat{\mathbf{d}}^2 = \left[\hat{a}_1^2\ \hat{l}_1^2\ \hat{a}_2^2\ \hat{l}_2^2 \cdots \hat{a}_m^2\ \hat{l}_m^2 \right]^T$ we obtain the linear system of size $2m$:

Table 1. The SNR and CNR of the strain images of Figure 2

	Axial, 2D AM	Axial, ElastMI	Lateral, 2D AM	Lateral, ElastMI
SNR	11.11	12.64	6.06	6.63
CNR	8.48	9.63	2.96	3.39

$$(\mathscr{I}' + \mathcal{D})\delta\mathbf{d}^2 = \boldsymbol{r} - \mathcal{D}\hat{\mathbf{d}}^2, \quad \mathcal{D} = \begin{bmatrix} \alpha & 0 & -\alpha & 0 & 0 & 0 & \cdots & 0 \\ 0 & \beta & 0 & -\beta & 0 & 0 & \cdots & 0 \\ -\alpha & 0 & 2\alpha & 0 & -\alpha & 0 & \cdots & 0 \\ 0 & -\beta & 0 & 2\beta & 0 & -\beta & \cdots & 0 \\ 0 & 0 & -\alpha & 0 & 2\alpha & 0 & \cdots & 0 \\ \vdots & & & & & & \ddots & \\ 0 & 0 & 0 & \cdots & -\alpha & 0 & \alpha & 0 \\ 0 & 0 & 0 & \cdots & 0 & -\beta & 0 & \beta \end{bmatrix}, \quad (5)$$

where $\mathscr{I}'$ is a symmetric tridiagonal matrix with 2×2 matrices $\mathfrak{I}'$ in its diagonal:

$$\mathscr{I}' = diag(\mathfrak{I}'^2(1) \cdots \mathfrak{I}'^2(m)),$$

$$\mathfrak{I}'^2(i) = \begin{bmatrix} (w_{12,i} + w_{13,i}\eta_{i,a}{}^2)I'_{1,a}{}^2 & (w_{12,i} + w_{13,i}\eta_{i,a}\eta_{i,l})I'_{1,a}I'_{1,l} \\ (w_{12,i} + w_{13,i}\eta_{i,a}\eta_{i,l})I'_{1,a}I'_{1,l} & (w_{12,i} + w_{13,i}\eta_{i,l}{}^2)I'_{1,l}{}^2 \end{bmatrix} \quad (6)$$

where I'_2 and I'_3 are calculated respectively at $(\mathbf{x}_i + \hat{\mathbf{d}}_i^2)$ and at $(\mathbf{x}_i + \boldsymbol{\eta}_i. * \hat{\mathbf{d}}_i^2)$, superscript $\prime$ indicates derivative and subscript a and l determine whether the derivation is in the axial or lateral direction, and $\boldsymbol{r}$ is a vector of length $2m$ with elements:

$$i \text{ even}: \ r_i = w_{12,i}I'_{1,a}(\mathbf{x}_i)\left[I_1(\mathbf{x}_i) - I_2(\mathbf{x}_i + \hat{\mathbf{d}}_i^2)\right] +$$
$$w_{13,i}\boldsymbol{\eta}_i. * I'_{1,a}(\mathbf{x}_i)\left[I_1(\mathbf{x}_i) - I_3(\mathbf{x}_i + \boldsymbol{\eta}_i. * \hat{\mathbf{d}}_i^2)\right]$$
$$i \text{ odd}: r_i = w_{12,i}I'_{1,l}(\mathbf{x}_i)\left[I_1(\mathbf{x}_i) - I_2(\mathbf{x}_i + \hat{\mathbf{d}}_i^2)\right] +$$
$$w_{13,i}\boldsymbol{\eta}_i. * I'_{1,l}(\mathbf{x}_i)\left[I_1(\mathbf{x}_i) - I_3(\mathbf{x}_i + \boldsymbol{\eta}_i. * \hat{\mathbf{d}}_i^2)\right]. \quad (7)$$

The coefficient matrix in Equation 5 is pentadiagonal and symmetric. As such, it can be solved in $8m$ operations, significantly less than $(2m)^3/3$ required for solving a full system. For all the results presented in this work, the EM algorithm is iterated once.

3   Results of Phantom Experiments and Patient Trials

RF data is acquired from an Antares Siemens system (Issaquah, WA) at the center frequency of 6.67 MHz with a VF10-5 linear array at a sampling rate

(a) 2D AM axial   (b) ElastMI axial   (c) 2D AM lateral   (d) ElastMI lateral
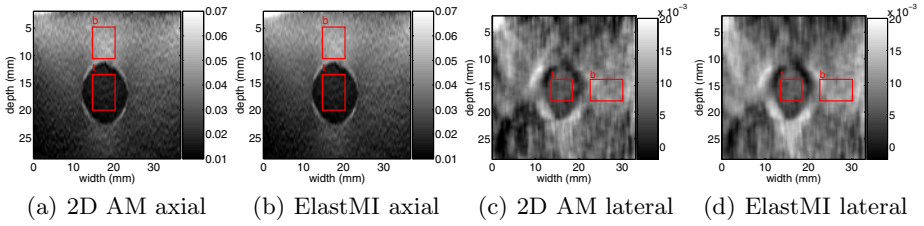
Fig. 2. Strain images of the CIRS phantom with the target and background windows (for calculation of SNR and CNR). No Kalman filter [16] is used to ease the comparison.

Table 2. The CNR of the strain images of first, second and third patient trials (images of second patient are shown in Figure 3). P1, P2 and P3 respectively correspond to patients 1, 2 and 3. $2(\bar{s}_b - \bar{s}_t)^2$ and $\sigma_b^2 + \sigma_t^2$ indicate contrast and noise respectively.

		before ablation		during ablation		after ablation	
		2D AM	ElastMI	2D AM	ElastMI	2D AM	ElastMI
	$10^4 \times 2(\bar{s}_b - \bar{s}_t)^2$	-	-	-	-	2.18	2.22
P1	$10^4 \times (\sigma_b^2 + \sigma_t^2)$	-	-	-	-	0.108	0.083
	$\text{CNR} = \sqrt{\frac{2(\bar{s}_b - \bar{s}_t)^2}{\sigma_b^2 + \sigma_t^2}}$	-	-	-	-	4.49	5.17
	$10^4 \times 2(\bar{s}_b - \bar{s}_t)^2$	0.45	0.89	-	-	2.08	2.15
P2	$10^4 \times (\sigma_b^2 + \sigma_t^2)$	0.0036	0.0045	-	-	0.204	0.142
	$\text{CNR} = \sqrt{\frac{2(\bar{s}_b - \bar{s}_t)^2}{\sigma_b^2 + \sigma_t^2}}$	11.16	14.05	-	-	3.19	3.89
	$10^4 \times 2(\bar{s}_b - \bar{s}_t)^2$	0.235	0.234	0.0745	0.1716	4.85	4.82
P3	$10^4 \times (\sigma_b^2 + \sigma_t^2)$	0.0045	0.0036	0.0091	0.0161	0.204	0.171
	$\text{CNR} = \sqrt{\frac{2(\bar{s}_b - \bar{s}_t)^2}{\sigma_b^2 + \sigma_t^2}}$	7.22	8.01	2.87	3.26	4.87	5.31

of 40 MHz. An elastography phantom (CIRS elastography phantom, Norfolk, VA) is compressed axially in two steps using a linear stage, and three images are acquired. Resulting strain images are shown in Figure 2. The unitless metric signal to noise ratio (SNR $= \frac{\bar{s}_b}{\sigma_b}$) and contrast to noise ratio (CNR $= \sqrt{\frac{2(\bar{s}_b - \bar{s}_t)^2}{\sigma_b^2 + \sigma_t^2}}$) [1] of the ElastMI algorithm are shown in Table 1 (The SNR is only calculated for the background window). Comparing to the 2D AM, the ElastMI algorithm improves the SNR by approximately 14% and the CNR by approximately 11%. The high quality of the lateral strain image, compared to state of the art strain imaging techniques, is visually noticeable.

In the clinical studies, RF data was acquired from ablation therapy of three patients with liver cancer using the Siemens Antares ultrasound machine in the following way: for the first patient only after ablation, for the second patient before and after ablation, and for the third patient before, during and after ablation. The ablation was administered using the RITA Model 1500 XRF generator (Rita Medical Systems, Fremont, CA). Tissue was simply compressed freehand at a frequency of approximately 1 compression per 2 sec with the ultrasound probe without any attachment, and the strain images are generated offline.
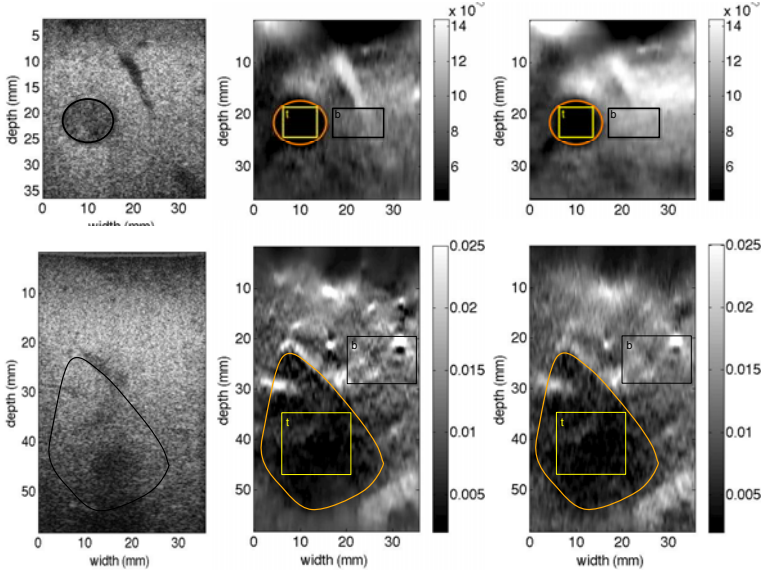
Fig. 3. Axial strain images of the second *in-vivo* patient trial corresponding to before (top row) and after (bottom row) ablation. The first, second and third columns are respectively B-mode, 2D AM strain and ElastMI strain images. The cancer tumor in the top row, and the ablated lesion in the bottom row are delineated. The CNR between the target and background (marked by t & b) windows are given in Table 2.

Results of the second patient trial are shown in Figure 3. Considering the numerous sources of noise in the clinical data, the high contrast of the tumor (top row) and the ablated lesion (bottom row) in the strain images make ElastMI a promising tool for both finding the tumor and monitoring the ablation. It should be noted that elastographic analysis of the ablated lesion is known to be challenging due to high temperatures which significantly degrade the quality of ultrasound data (mainly because of the air bubbles). Table 2 summarizes the CNR, as well as noise and contrast values, in the patient trials obtained using 2D AM and ElastMI methods. In the six cases presented in this table (two before ablation, one during ablation and three after ablation), the average increase in the CNR achieved using ElastMI compared to 2D AM is 17%.

4   Conclusions

In this work, we proposed to utilize three ultrasound images to calculate high quality displacement fields. We neglected the dynamics of tissue motion and assumed a static model for tissue mechanics, which is valid in the quasi-static elastography. Using this model and assuming tissue linearity, which holds in the low strain rates of the freehand elastography, we introduced constraints on the variations of the strain field with time. We then proposed ElastMI, an EM algorithm that exploits these constraints for estimating displacement fields using

three images. The algorithm involves solving sparse linear systems, and therefore runs in real-time. The low variance motion field that we compute by exploiting this new prior can be used in numerous applications in ultrasound imaging; we used it here to generate strain images.

References

1. Greenleaf, J., Fatemi, M., Insana, M.: Selected methods for imaging elastic properties of biological tissues. Annu. Rev. Biomed. Eng. 5, 57–78 (2003)
2. Hall, T., Zhu, Y., Spalding, C.: In vivo real-time freehand palpation imaging. Ultrasound Med. Biol. 29, 427–435 (2003)
3. Zahiri, R., Salcudean, S.: Motion estimation in ultrasound images using time domain cross correlation with prior estimates. IEEE TBME 53, 1990–2000 (2006)
4. Rivaz, H., Boctor, E., Foroughi, P., Fichtinger, G., Hager, G.: Ultrasound elastography: a dynamic programming approach. IEEE Trans. Med. Imag. 27, 1373–1377 (2008)
5. Rivaz, H., Fleming, I., Assumpcao, L., Fichtinger, G., Hamper, U., Choti, M.A., Hager, G.D., Boctor, E.M.: Ablation monitoring with elastography: 2D *in-vivo* and 3D *ex-vivo* studies. In: Metaxas, D., Axel, L., Fichtinger, G., Székely, G. (eds.) MICCAI 2008, Part II. LNCS, vol. 5242, pp. 458–466. Springer, Heidelberg (2008)
6. Rivaz, H., Foroughi, P., Fleming, I., Zellars, R., Boctor, E., Hager, G.: Tracked regularized ultrasound elastography for targeting breast radiotherapy. In: Yang, G.-Z., Hawkes, D., Rueckert, D., Noble, A., Taylor, C. (eds.) MICCAI 2009. LNCS, vol. 5761, pp. 507–515. Springer, Heidelberg (2009)
7. Lindop, J., Treece, G., Gee, A., Prager, R.: 3D elastography using freehand ultrasound. Ultrasound Med. Biol. 32, 529–545 (2006)
8. Jiang, J., Hall, T., Sommer, A.: A novel image formation method for ultrasonic strain imaging. Ultrasound Med. Biol. 53, 1088–1102 (2007)
9. Lindop, J., Treece, G., Gee, A., Prager, R.: An intelligent interface for freehand strain imaging. Ultrasound Med. and Biol. 34, 1117–1128 (2008)
10. Chen, L., Housden, R., Treece, G., Gee, A., Prager, R.: A data weighting scheme for quasistatic ultrasound elasticity imaging. Univ. of Cambridge TR651 (2010)
11. Brown, M., Burschka, D., Hager, G.: Advances in computational stereo. IEEE Trans. Pattern Anal. Mach. Intell. 25, 993–1008 (2003)
12. Moradi, M., Mousavi, P., Abolmaesui, P.: Tissue typing using ultrasound rf time series: Experiments with animal tissue samples. Med. Phys. 37, 1401–1413 (2010)
13. Li, L., Cui, Y., Kadour, M., Noble, A.: Elasticity reconstruction from displacement and confidence measures of a multi-compressed ultrasound rf sequence. IEEE Trans. Ultrason. Ferroelectr. Freq. Control 55, 319–326 (2008)
14. Catheline, S., et al.: Measurement of viscoelastic properties of homogeneous soft solid using transient elastography. J. Acoust. Soc. Amer. 116, 3734–3741 (2004)
15. Eskandari, H., Salcudean, S., Rohling, R.: Viscoelastic parameter estimation based on spectral analysis. IEEE T. Ultrason. Ferro. Freq. Control 55, 1611–1625 (2008)
16. Rivaz, H., Boctor, E.M., Choti, M.A., Hager, G.D.: Real-time regularized ultrasound elastography. IEEE Trans. Med. Imaging 30, 928–945 (2011)